INTERNATIONAL ATOMIC ENERGY AGENCY
UNITED NATIONS EDUCATIONAL, SCIENTIFIC AND CULTURAL ORGANIZATION

INTERNATIONAL CENTRE FOR THEORETICAL PHYSICS
34100 TRIESTE (ITALY) - P.O.B. 586 - MIRAMARE - STRADA COSTIERA 11 - TELEPHONE: 2240-1
CABLE: CENTRATOM - TELEX 460392 - I

SMR/459 - 23

SPRING COLLEGE IN CONDENSED MATTER
ON
'PHYSICS OF LOW-DIMENSIONAL SEMICONDUCTOR STRUCTURES'
(23 April - 15 June 1990)

BACKGROUND MATERIAL FOR THE LECTURE COURSE ON

"HOT CARRIERS"

Paolo LUGLI
II Universita' degli Studi di Roma
Dipartimento di Ingegneria Meccanica
Via Orazio Raimondo
00173 Roma

Solid-State Electronics Vol. 32, No. 12, pp. 1881–1885, 1989
Printed in Great Britain

0038-1101/89 $3.00 + 0.00
Pergamon Press plc

HOT PHONONS IN QUANTUM WELLS SYSTEMS

P. Lugli

Dipartimento di Ingegneria Meccanica, II Universita' di Roma
Via O. Raimondo, 00173 Roma, Italy

P.Bordone, S. Gualdi, P. Poli

Dipartimento di Fisica, Universita' di Modena
Via Campi 213/A, I-41100 Modena, Italy

S. M. Goodnick

Dept. of Electrical and Computing Engineering,
Oregon State University, Corvallis, Oregon, 97331 USA

ABSTRACT

We present an investigation of non-equilibrium LO-phonon effects in quantum well systems. Phonon confinement is taken into account by considering esplicitly slab modes in the formulation of Fuchs and Kliever. With respect to the "standard" case, where a tridimensional dispersion is used for the LO phonons, the electron-phonon interaction is riduced as result of phonon confinement. We use the Monte Carlo (MC) scheme, which allows the simultaneous study of the coupled electron and phonon dynamics, without requiring any sort of assumption on the respective distribution function. It should be pointed out that the quantization of the phonon wavevector in the direction perpendicular to the interface completely solves the normalization problems of the hot-phonon calculation in 2D-systems. For the case of photoexcitation in AlGaAs-GaAs quantum wells we observe a reduction in the cooling rate due to the reabsorption of hot phonon.

KEYWORDS

Hot phonons, slab modes, quantum wells, Monte Carlo simulation.

INTRODUCTION

Non equilibrium phonons have recently received a lot of attention. This is largely due to the availability of time resolved optical experiments performed on a picosecond and subpicosecond time scale which have given useful information on the microscopic processes active in such a time scale and indicated that phonon heating is a relevant process in the relaxation of photoexcited carriers (Shah and others, 1985;Ryan and others, 1988; Lobentanzer and others,1987). It has been shown for example that the density dependence of the cooling of hot plasma in quantum well (QW) systems is largely attributable to the presence of perturbed LO phonon distributions. At the same time, Raman spectroscopy has indicated directly the presence of such non equlibrium distributions following laser excitation, first in bulk GaAs (Von der Linde and others, 1980; Kash and others, 1985) and recently in GaAs/AlGaAs QW's (Tsen and others, 1989). From the theoretical point of view there has also been a lot of activity focusing both on the study of the vibrational properties of low dimensional sytems as well as on the carrier-phonon interaction and its effects on carrier dynamics in highly nonequilibrium situations. The latter class of investigations have been based mainly on semiclassical Boltzmann equation, solved either through the moment method (Marchetti and Poetz, 1989; Joshi and Ferry,1989) or by Monte Carlo (MC) technique (Lugli and Goodnick, 1987; Goodnick and Lugli, 1988). Microscopic models have been set up that describe quite accurately some of the most important features of carrier cooling. Nevertheless, many aspects need to be clarify, preventing in many cases a direct fit of the experimental data. We will concentrate now on the phonon properties of superlattices and QW.

PHONONS IN TWO DIMENSIONAL SYSTEMS

The study of the vibrational properties of QW's and superlattices is a relatively new subject (two excellent reviews on the subject can be found in Jusserand and Cardona, 1989, and Menendez, 1898). Most of the theoretical and experimental work has centered on the physics of phonons in such system, without focusing on its implications on carrier transport. On the other side, the transport community has so far neglected all the features connected to phonon confinements (except for some isolated attempts, such as Riddoch and Ridley, 1985; Sawaki, 1986; Babiker and others, 1987), relying on the well established bulk phonon picture. While such approximation is justifiable for large QW's (well width of 10 nm or more), a more creative and rigorous approach is needed for narrower wells. We will treat here only optical phonons, which are the relevant feature when ultrafast phenomena are considered. It is well established that optical modes are fairly well localized in each layer of superlattices and QW's, with a small degree of penetration into adjacent layers depending on the properties of the interface.

Macroscopic models have been used to study the lattice dynamics of Q.W.'s and superlattices. On the basis of a dielectric continuum model, Fuchs and Kleever (1965) have analized the vibrational properties of the ionic slabs. By treating the LO modes as consisting only of electrostatic fields, the solution of Laplace equation leads to two sets of modes, guide modes whose associated displacement is represented by sine and cosine functions, and surface modes, with displacement given by sinh and cosh functions. The standard electrostatic B.C.'s imposed on the field lead to a zero value for the potential at the boundaries, with the transverse displacement in antiphase with respect to the potential. Such formalism has been used by Riddoch and Ridley (1986) to determine the scattering rates and by Jain and Das Sarma (1988) to calculate the energy loss rate due to polar optical scattering in Q.W. and superlattices. Recently it has been pointed out (Cardona, 1988) that mechanical B.C.'s must also taken into consideration, by imposing phonon confinement via a zero displacement at the boundaries. Accordingly, since the mechanical displacement is proportional to the electrical polarization, the potential is bound to have a maximum at the interface. Furthermore, because of the zero displacement condition, no surface modes are allowed by the mechanical B.C.'s. Such conclusion are somewhat analogous to the results of Babiker (1986) (based on a dispensive continuum model) and of microscopic models (Molinari and others, 1986; Huang and Zhu, 1989).
The incompatibility of the two boundaries conditions, and the consequent opposite simmetry of the dispacements and potentials have originated some controversy (Ridley, 1989). It has recently been shown (Huang and Zhu, 1989; Menendez, 1989) that no controversy actually exists and that proper account of the surface modes lead to a good agreement between Fuchs and Kleever model and microscopic calculation. The key point is that the interface modes of the dielectric contiuum model (which for k = 0 become bulk-like vibration) corresponde to the modeless first confined modes of the microscopic model. Once the "interface modes" are included into the picture, the simmetry of the successive confined modes coincides in the two models. We will base our treatment on Fuch and Kliever approach.

M.C. SIMULATION

We describe here briefly the Monte Carlo simulation used for the present study. A detailed discussion of the model can be found Goodnick (1989). This model simulates the carrier dynamics of photogenerated electrons and holes using the computer random number generator to generate the stochastic collision times and final states of these carriers as they interact among themselves and with the lattice through optical phonon scattering. We simultaneously simulate an ensemble of several thousand particles in order to study the transient behavior of the electronic system during and after photoexcitation. The basic model for the quantum well system contains scattering mechanisms due to slab modes for electrons and holes, TO phonons for holes as well as carrier-carrier (c-c) scattering, calculated numerically using the envelope function states of the quantum well system. The c-c scattering rate is calculated using a screened Coulomb potential with the use of a static screening constant which is updated during the simulation to account for the time dependent density and temperature of the electron system during photoexcitation. To account for hot phonon effects, we employ the algorithm previously employed for the bulk modes (Lugli and Goodnick, 1987) in which the population of phonons is calculated by a detailed balance of phonon emission and absorption events with the electrons system. The excess phonon population is also assumed to decay phenomenologically due to anharmonic interactions. The dynamic population of excess phonons is used to recalculate the electron-phonon scattering rate at each time step of the simulation, strongly coupling the carrier and phonon systems. It should be pointed out that considering slab modes solves all the problems connected to the normalization of the phonon distribution function of our previous model.

The total scattering rate for electrons in the first subband of a 150 A well due to guided modes (dashed line) and to surface modes (dotted line) at 10 K is compared with the bulk three-dimensional scattering rate in Fig.1. We can notice that the contribution of the surface modes is negligible under those circumstances. These scattering rates have been used for the M. C. simulation of the relaxation of a photoexcited plasma in a n-doped quantum well. The parameters have been chosen so as to reproduce the experimental condition of Ryan and others (1988). The background electron doping density is 7×10^{11} cm $^{-2}$, while the excited carrier densityis 5×10^{11} cm $^{-2}$. Electrons are injected with an excess energy of 200 meV, at a lattice temperatureof 10 K. Figure 2 and 3 show respectively the average electron and hole energy (expressed in K degree) as a function of time The three curves correspond to different values of confined phonon lifetime τ, respectively 0 ps (i.e. equilibrium phonons, continuous curve), 7 ps (dashed curve) and 25 ps (dotted curve). The different behavior is attributed to

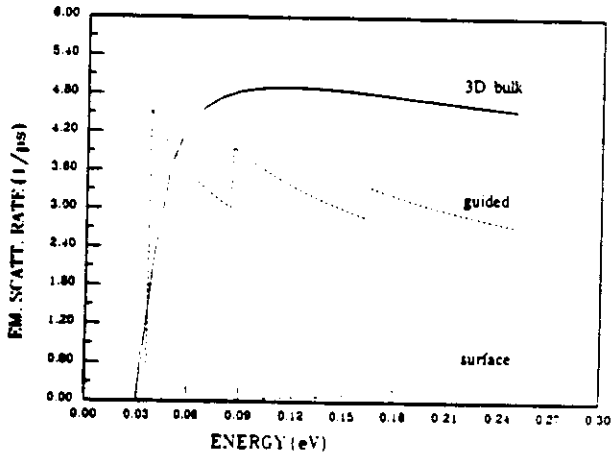

Fig. 1. Scattering rate for optical phonon emission in a 150 A QW at T = 10 K. Dashed and dotted lines show respectively the contribution of guided and surface modes, compared with the 3D bulk rate (continuous line).

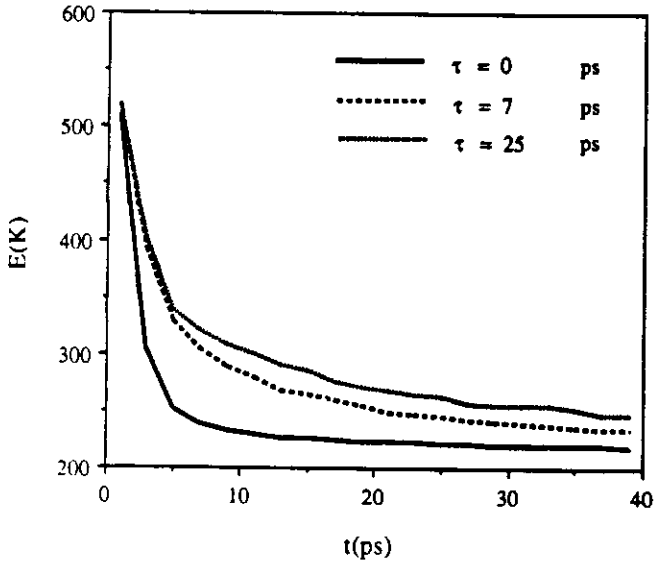

Fig. 2. Electron average energy as function of time after excitation (with a 1 ps laser pulse) for three different values of LO phonon lifetime.

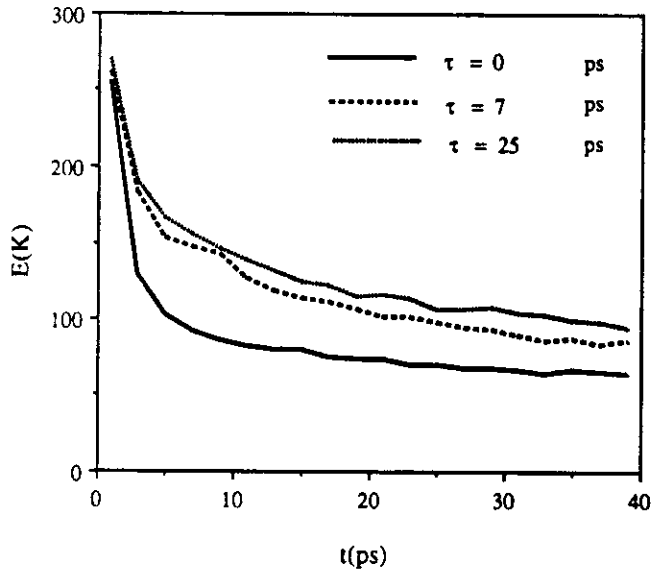

Fig. 3. Hole average energy as function of time after excitation (with a 1 ps laser pulse) for three different values of LO phonon lifetime.

non-equilibrium phonons, in the same way as previously found (Lugli and Goodnick, 1987). When phonons are kept in thermal equilibrium (t =0) carriers exhibit a faster decay; the rate at which the cooling process slows down depends on the phonon lifetime, since the reabsorption process is directly proportional to N_q.

Holes exhibit the same type of behavior, with the reduced cooling associated mainly with the presence of nonequilibrium LO phonons. TO phonons are very slightly perturbed, mainly because of the larger q-space region that the emitted phonons fill up. The phonon distribution at 1 ps time delay for the three lowest guided modes is shown in Fig. 4. Here a phonon lifetime of 7 ps is taken The main contribution comes from the m=1 mode, which, because of its parity, reflects mainly the contribution of intrasubband transition. Very little scattering via surface modes is detected, as indicated by the negligible scattering rate with surface modes in Fig. 1. Neverthless, since these phonons are emitted over a very small region of q space, a certain degree of heating has been found. The non equilibrium distribution of the first guide mode is plotted at three different delay times in Fig. 5. The highest perturbation is obtained immediately after the excitation, very pronunced at small q's, in correspondence to emission by the photoexcited electrons. Holes contribute less to the heating of slab modes because of the heavier mass (which implies a larger q of the emitted phonons), the reduced excess energy and the strong coupling to TO phonons.

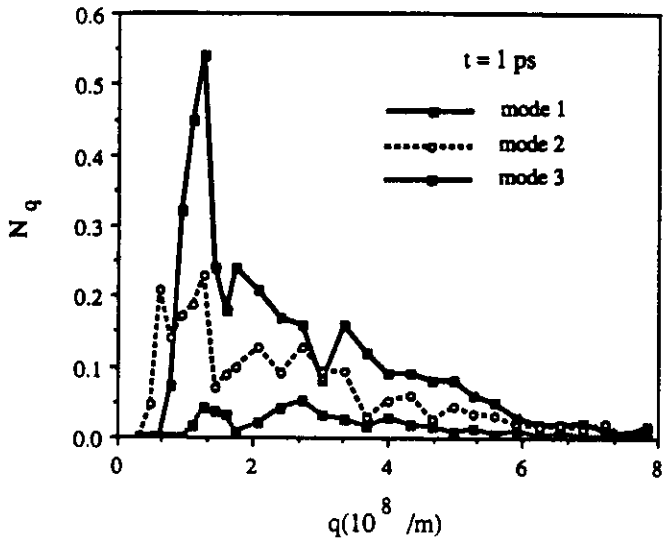

Fig. 4. Non equilibrium phonon distribution fot three guided modes (m = 1,2,3) at 1 ps time delay.

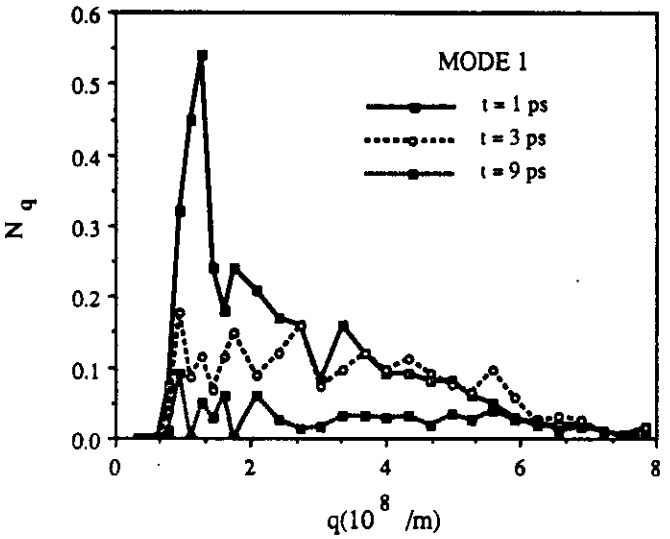

Fig. 5. Non equilibrium phonon distribution for the first guided mode, at three different times after photoexcitation.

The phonon perturbation is somewhat smaller than the one reported in own previous study. This is a consequence of the strong intercarrier scattering, that opens a channel for energy dissipation from the photoexcited plasma ($n = p = 3x10^{11}$ cm $^{-2}$) to the background density of cold electrons ($n = 7x10^{11}$ cm $^{-2}$). Figure 6 shows the net rate of energy transfer from the electrons into the lattice via scattering with slab modes compared to the rate of energy exchange (in absolute value) via electron-electron and electron-hole scattering. At short times (t<5 ps), the photoexcited electrons loose energy to the lattice (the emission rate being higher than the absorption rate), and to the other carriers (background electrons and photoexcited holes). At later times, the energy loss rate is considerably reduced, leading to the slow decay of the electron average energy shown in Fig. 2.

CONCLUSIONS

We have discussed the properties of phonons in two dimensional system, pointing out the relation between existing macroscopic continuum models and microscopic formulations. A Monte Carlo simulation has been performed to study the effect of non equilibrium confined phonons on the relaxation of photoexcited carriers in GaAs/AlGaAs quantum wells. We have shown that the presence of phonon perturbations slows down the cooling of both electrons and holes.

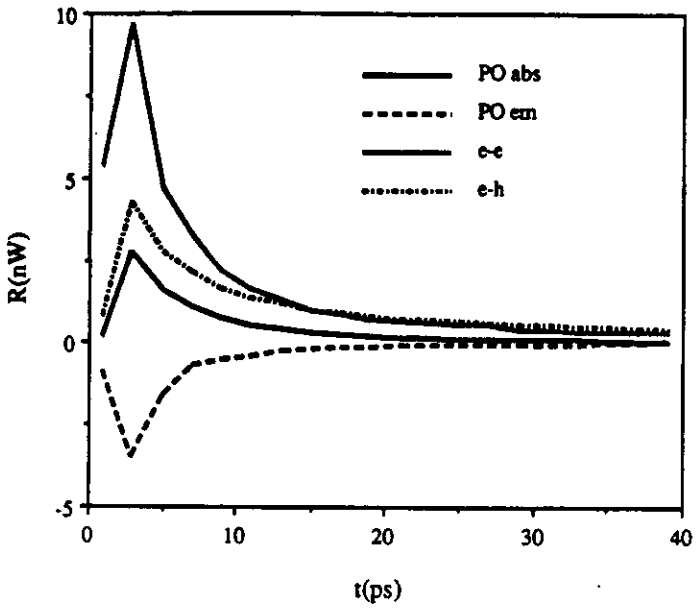

Fig. 6. Electron energy transfer rate (for PO absorption and emission), and exchange rate (for electron-electron and electron-hole scattering) as a function of time after photoexcitation.

ACKNOWLEDGMENTS

This work was partially supported by Office of Naval Research, the National Center for Supercomputing Applications and the Computer Center of the Modena University.

REFERENCES

Babiker, M. (1986). *J. Phys.*, C19, 683.
Babiker, M., M. P. Chamberlain, and B. K. Ridley (1987). *Semicond. Sci. Technol.*, 2, 582.
Cai, W., C. Marchetti, and M. Lax (1988). *Phys. Rev.*, B 34, 8573.
Cardona, M. (1988). *Superlatt. and Microstruct.*, 5, 27.
Fuchs, R., and K. L. Kliever, (1965). *Phys. Rev.*, 140A, 2076.
Goodnick, S. M., (1989). "Proc. of NATO ARW on Spectroscopy of Semiconductor Microstructures", Eds. G. Fasol, A. Fasolino and P. Lugli, Plenum Press, in press.
Goodnick, S. M. and P. Lugli (1988). *Phys. Rev.*, B 37, 2578.
Huang, K. and B. Zhu (1988). *Phys. Rev.*, B 38, 13377
Jain, K., J., and S. Das Sarma (1988). *Phys. Rev. Lett.*, 62, 2305.
Joshi, R. P., and D. K. Ferry (1988). *Phys. Rev.*, B 39, 1180.
Jusserand, B. and M. Cardona. in "Light Scatering in Solids V". ed. by M. Cardona and G. Guntherodt, Springer, Berlin, 1989.
Kash, J. A., J. C. Tsang, and J. M. Hvam (1985). *Phys. Rev. Lett.*, 54, 2151.
Lobentanzer, H., H. J. Polland, W. W. Ruhle, W. Stolz, and K. Ploog (1987). *Appl. Phys. Lett.*, 51, 673.
Lugli, P., and S. M. Goodnick (1987). *Phys. Rev. Lett.*, 59, 716.
Marchetti, C., and W. Poetz (1988). *J. Vac. Sci. Technol.*, 6, 1341.
Menendez, J. (1989). to be published in *J. of Luminescence*.
Molinari, E., A. Fasolino, and K. Kunc (1986).*Superlatt. Microstruct.*, 2, 397.
Ryan, J. F., M. Tatham, D. J. Westland, C. T. Foxon, M. D. Scott, and W. I. Wang (1988). *Proc. SPIE* 942.
Riddoch, F. A. and B. K. Ridley (1986). *Physica B+C*, 134B, 342.
Ridley, B. K. (1989). *Phys. Rev.*, B 39, 5282.
Sawaki, N. J. (1986). *J. Phys.*, C 19, 4965.
Shah, J., A. Pinczuk, A.C. Gossard and W. Wiegmann (1985). *Phys. Rev. Letter.*, 54, 2045.
Tsen, K. T., R. P. Joshi and D. K. Ferry, H. Morkoc (1988). *Phys. Rev.*, B 39, 1446.
Von der Linde, D., J. Kuhl, and H. Klingenberg (1980). *Phys. Rev. Lett.*, 44, 1505

Solid-State Electronics Vol. 32, No. 12, pp. 1737-1741, 1989
Printed in Great Britain.

0038-1101/89 $3.00 + 0.00

MONTE CARLO SIMULATION OF FEMTOSECOND SPECTROSCOPY IN SEMICONDUCTOR HETEROSTRUCTURES

Stephen M. Goodnick

Department of Electrical and Computer Engineering
Oregon State University, Corvallis, Oregon 97331

Paolo Lugli

Dipartimento di Ingegneria Meccanica
II Universita' di Roma, Via O. Raimondo, 00173 Roma, Italy

Wayne H. Knox and Daniel S. Chemla

AT&T Bell Laboratories, Holmdel NJ 07733

ABSTRACT

We use an ensemble Monte Carlo simulation for photoexcited electrons and holes in a quantum well structure to model the effects of carrier-carrier scattering on the observed time resolved differential transmission spectrum from undoped, n- and p-type structures. The simulated absorption spectrum agrees with the qualitative trends observed experimentally showing reduced thermalization times as the density in the system increases. However, differences are found between the model and experiments in very dense systems with carrier concentrations exceeding $5x10^{11}/cm^2$ which we attribute to strong renormalization effects in the optical spectrum and the breakdown of the single particle picture.

INTRODUCTION

Ultrafast optical studies of semiconductor quantum wells have supplied a great deal of information concerning the nonequilibrium dynamics of electrons and holes (Rosker, 1986; Ryan, 1986; Knox, 1986; Oberli, 1987). Recently, differential absorption experiments have been performed under conditions which isolate the effects of intercarrier scattering(Knox and coworkers, 1986; 1988; 1989). By using a suitable pump pulse energy such that the excess energy of photoexcited electrons and holes is less than the optical phonon energy, the injected carriers are inhibited from emitting phonons and relaxing their excess energy on the time scale of the experimental studies(usually on the order of a picosecond or less). Thus it is argued that the changes in the differential transmission spectrum observed experimentally arise from carrier-carrier scattering which causes the initial nonthermal distribution to relax to a Maxwell-Boltzmann type of distribution on a time scale of 100fs or less (Knox and coworkers, 1986; 1988; 1989). Various undoped, n-type and p-type modulation doped samples were studied with varying excitation intensities in order to vary the number of photogenerated electrons and holes. However, in all cases, the absorption spectrum indicated the presence of a nonthermal distribution of carriers centered around the spectral hole burning at the peak of the pulse, which subsequently decays for delay times after the pulse to form a Maxwellian type background. For undoped samples (Knox and coworkers, 1986; 1988), the thermalization time at low excitation densities was found to be longest, on the order of 100fs. As the excitation density was increased, the thermalization time decreased to 30fs for an injected density of $5x10^{11}/cm^2$. Modulation doped samples were later considered in order to isolate the effects of electrons and holes separately (Knox and coworkers, 1989). For n-type samples with an aerial density of $3x10^{11}/cm^2$, carrier thermalization appears so rapidly, that it occurs on a time scale below the system resolution of 10fs. Modulation doped p-type samples showed unusual Fermi edge shift and broadening which greatly complicates the interpretation of the measured spectrum. In spite of this difficulty, an estimate of 60fs was made of the thermalization time based on comparison to a simple relaxation time approximation model.

In previous work, we have simulated the electron and hole dynamics for such differential absorption measurements using an ensemble Monte Carlo numerical method (Goodnick and Lugli, 1988a; 1988b; 1988c). For electrons only, the results show qualitative agreement with the trends observed experimentally, i.e. 100fs relaxation times for low density samples and shorter times for high density and doped samples (Goodnick and Lugli, 1988a). More recently, this model was expanded to include both electrons and heavy holes in the simulation (Goodnick and Lugli, 1988c). This was applied to the study of the lowest density, undoped experiments discussed above, with a good agreement between the calculated differential transmission spectrum and the experimental result. An important result of this work was the identification of the electrons as the main contribution to the observed relaxation.

The basic model contains intercarrier scattering based on a two-particle screened Coulomb interaction discussed in detail elsewhere (Goodnick and Lugli, 1988b). The generalization of this formalism to include electron-hole scattering is accomplished by replacing the single band masses with the appropriate reduced masses and scaling the relative wavevectors accordingly (Goodnick and Lugli, 1988c). An important quantity in this model for carrier-carrier interaction is the choice of the proper dielectric screening function. Here we take the long wavelength limit of the multi-band Lindhard dielectric function for quasi-two-dimensional particles and assume that the interaction is statically screened. The resulting screening

constant is proportional to the sum of the occupancies of the bottom of each subband, a quantity which we calculate at every time step of the simulation. The approach here is essentially single particle, and hence neglects important contributions due to plasmon effects. However, a nonequilibrium theory for the plasmon loss rate is beyond the scope of the present work.

In the present paper, we extend our previous work on intercarrier relaxation to include the n and p-type structures recently reported by Knox and coworkers (1989). Here we present results for the calculated differential transmission spectrum based on the electron and hole distributions obtained from simulation of the carrier dynamics after photoexcitation. For n-type and p-type samples, the simple relation giving the differential transmission as the sum of the electron and hole distribution functions must be modified by the initial occupancies to give

$$\Delta T(h\nu,t)/To = 1 - (1-f_e(k,t) - f_h(k,t)) / (1-f_{eo} - f_{ho}) \quad (1)$$

where the distribution functions, $f_{eo,ho}$ refer to the initial values before photoexcitation. Thus the differential transmission spectrum is not necessarily a direct measure of the electron and hole distribution functions. The well widths are chosen to agree with the experimental values: 9.6 nm for undoped samples, 11 nm for p-type and 12 nm for n-type. The excitation photon energy is chosen such that electrons are injected 20meV above the bottom of the ground subband. A gaussian spectral shape is assumed with a 10meV half width a 100fs pulse duration.

UNDOPED QUANTUM WELLS

The calculated differential transmission based on (1) is shown first for undoped wells with three different values of the injected carrier concentration. The first excitation density in Fig. 1a for $2x10^{10}/cm^2$ corresponds to our previous results (Goodnick and Lugli, 1988c) for low excitation intensities. The athermal peak in the absorption coefficient there was shown to arise from a similar athermal peak in the electron distribution function. This peak centered around the pump energy of 1.488eV persists for 100 fs after the peak of the pulse at t= 0fs. This value is in agreement with the experimentally measured value under the same conditions. In contrast, for an injected density of $2x10^{11}/cm^2$ shown in Fig. 1b , the athermal peak is barely discernable at 50 fs after the peak of the pulse. Thus the apparent relaxation time due to carrier-carrier scattering has decreased substantially by increasing the injected carrier density by an order of magnitude in agreement with the experimental trend with injected carrier density. However, when the carrier density is further increased to $5x10^{11}/cm^2$, the apparent relaxation time does not continue to decrease. Rather, it actually increases slightly. To understand this effect, we must first consider the primary source of intercarrier relaxation which is inelastic scattering. It is quite easy to show from the collision integral of the Boltzmann equation that for a spherically symmetric distribution function such as one encounters during photoexcitation, that the rate of change of the distribution function due to intercarrier collisions vanishes for purely elastic scattering. Inelastic scattering is necessary for the system to evolve in phase space in accordance with Boltzmann's H-theorem and thus reach the maximum entropy quasi-equilibrium final state. Thus, a measure of the effectiveness of inelastic intercarrier in relaxing the nonequilibrium photoexcited distribution is the rate of energy exchanged per particle. We tabulate this quantity for both electron-electron (e-e) and electron-hole (e-h) events during the simulation and average over each time step. For sufficiently long times after the pulse, the energy exchange rate approaches a constant which is dependent on the final density and temperature of the carriers in the system. This value is tabulated in Table I for the various samples considered here:

TABLE I
ENERGY EXCHANGE RATE(nW)

Density($x10^{11}/cm^2$) (background)	Density($x10^{11}/cm^2$) (injected)	e-e	e-h	type
0.0	0.2	28	18	i
0.0	2.0	53	49	i
0.0	5.0	40	43	i
3.0	3.0	41	21	n
2.0	3.0	33	51	p

For the undoped samples, we see from Table I that the energy exchange rate of both electrons and holes follows the qualitative relaxation time behavior fairly well. The energy exchange rate is reduced going from $3x10^{11}/cm^2$ to $5x10^{11}/cm^2$. The reason for this effect arises from the trade-off between increased intercarrier scattering at increased carrier density and the opposite effect of increased screening(Goodnick and Lugli, 1988a). For this reason, it is apparent that the calculated relaxation rate is dependent on the exact screening model used. Using a full dynamical screening model rather than the static model used here could give quite different trends with density.

DOPED QUANTUM WELLS

For doped quantum wells, the injected carrier dynamics are modified due to the presence of a background equilibrium concentration of carriers which interact with the photoexcited carriers. Figures 2a and b show the calculated differential transmission spectrum for the n-type and p-type samples studied experimentally by Knox and coworkers(1989). In Fig. 2a, the calculated spectrum shows a clear athermal peak at the maximum of the pump pulse. However, after 50fs, the spectrum appears as a distorted athermal peak resembling a cold Fermi gas injected into the system. In any case, the apparent

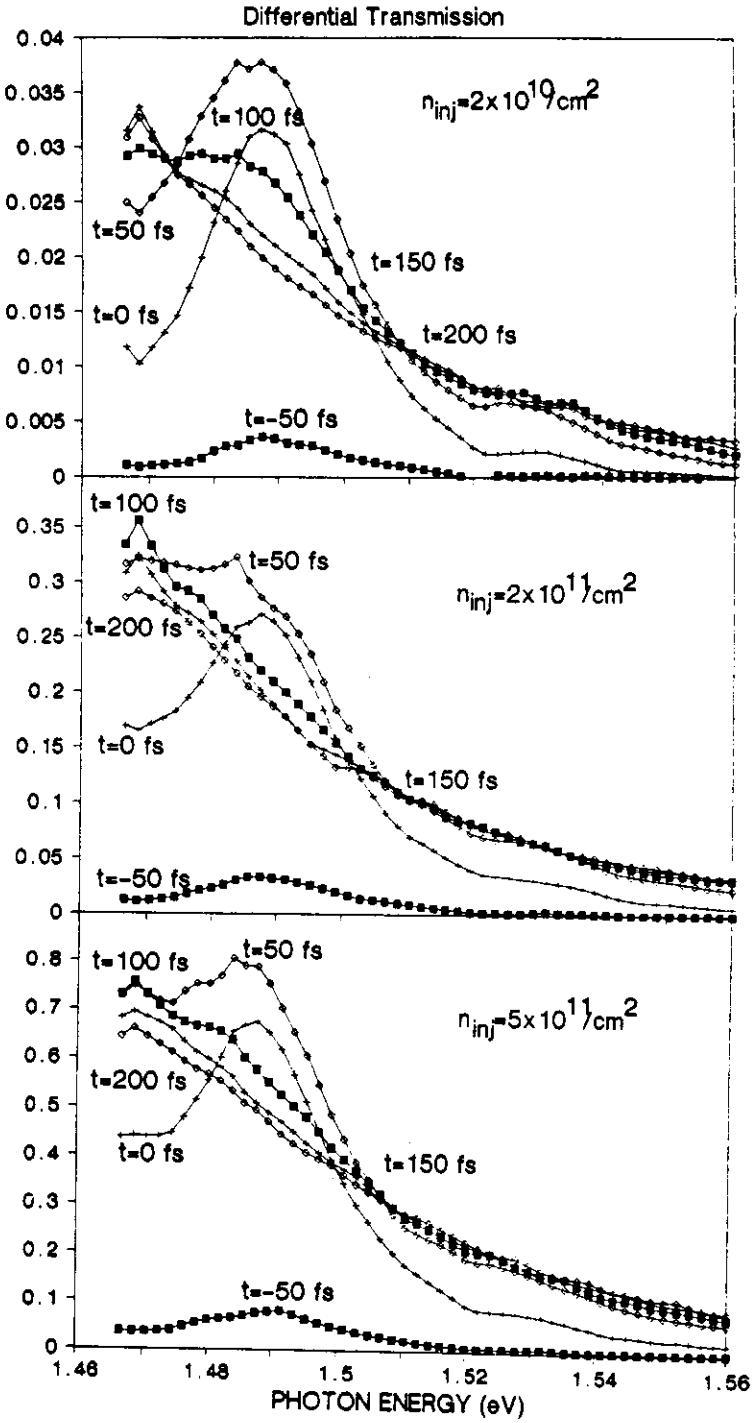

Fig. 1. Differential absorption spectrum calculated using (1) for undoped quantum wells with 20meV excess electron energy for a) $2x10^{10}/cm^2$ injected electron hole pairs, b) $2x10^{11}/cm^2$ injected electron hole pairs, and c) $5x10^{11}/cm^2$ injected carriers.

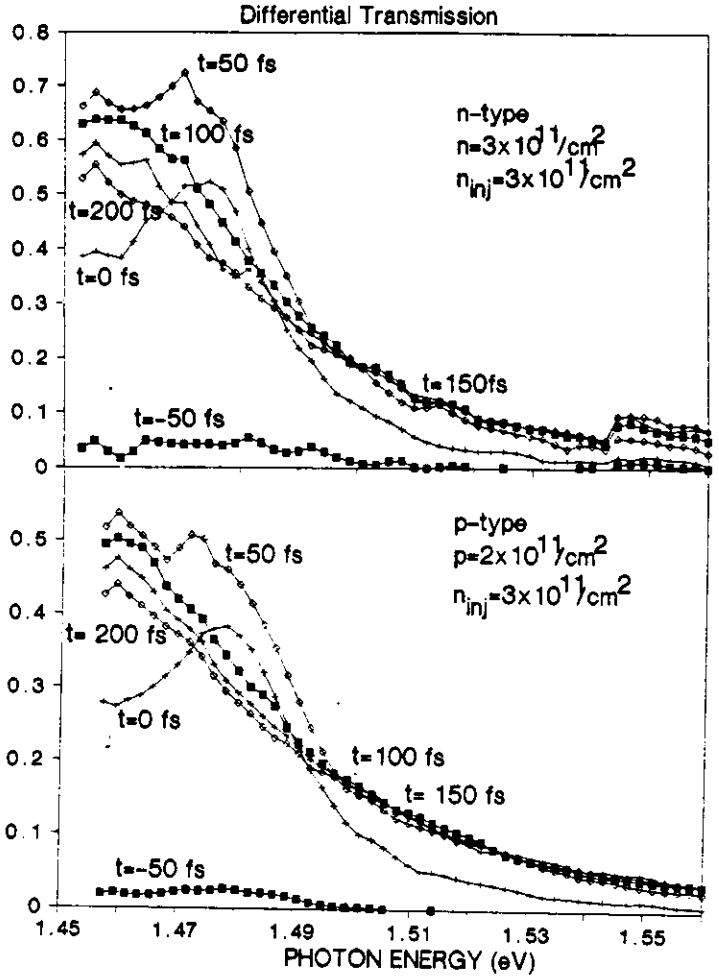

Fig. 2. Differential absorption spectrum calculated using (1) for a) n-type quantum wells, $3x10^{11}/cm^2$ background concentration, $3x10^{11}/cm^2$ injected electron hole pairs, and b) p-type quantum wells, $2x10^{11}/cm^2$ background concentration, $3x10^{11}/cm^2$ injected electron hole pairs.

'thermalization' is quite rapid in accordance with the'qualitative behavior measured experimentally. In Fig. 2b, the differential transmission for various times is shown for a p-type sample. Here the apparent relaxation occurs over a time period at least as short as that observed in Fig. 2a for the n-type sample. The e-h scattering is quite effective in exchanging energy in the p-type sample as indicated in Table I which accounts for the rapid thermalization shown in Fig. 2b. This behavior is somewhat in disagreement with the observation of Knox (1989) who found longer times in p-type than in n-type samples. However, as discussed there, the optical absorption spectrum in the modulation doped samples is subject to rather strong renormalization and many body effects which greatly complicates the interpretation of the data. Also, the model presented here is essentially single particle in nature, and thus one expects that this picture will be inaccurate for dense Fermi systems such as one encounters in heavily doped material.

ACKNOWLEDGEMENTS

One us(SMG) would like to acknowledge the support of the Office of Naval Research and the National Center for Supercomputer Applications.

REFERENCES

Goodnick, S.M., and P. Lugli, (1988a). *Solid State Electron.*, 31, 463.
Goodnick, S.M., and P. Lugli, (1988b). *Phys. Rev.*, B37, 2578.
Goodnick, S.M., and P. Lugli, (1988c). *Phys. Rev.*, B38, 10135.
Knox, W.H., C. Hirlimann, D.A.B. Miller, J. Shah, D.S. Chemla, and C.V. Shank, (1986). *Phys. Rev. Lett.*, 56, 1191.
Knox, W.H., D.S. Chemla, and G. Livescu, (1988). *Solid State Electron.*, 31, 425.
Knox, W.H., D.S. Chemla, G. Livescu, J.E. Cunningham and J.E. Henry, (1989). Accepted for publication, *Phys. Rev. Lett.*.
Oberli, D.Y., D.R. Wake, M.V. Klein, J. Klem, T. Henderson, and H. Morkoc, (1987). *Phys Rev. Lett.*, 59, 696.
Rosker, M., F. Wise, and C.L. Tang, (1986). *Appl. Phys. Lett.*, 49, 1714.
Ryan, J.F., R.A. Taylor, A.J. Turberfield, and J.M. Worlock, (1985). *Surf. Sci.*, 170, 511.

PHYSICAL REVIEW B VOLUME 38, NUMBER 14 15 NOVEMBER 1988-I

RAPID COMMUNICATIONS

Influence of electron-hole scattering on subpicosecond carrier relaxation in $Al_xGa_{1-x}As/GaAs$ quantum wells

Stephen M. Goodnick
Center for Advanced Materials Research, Oregon State University, Corvallis, Oregon 97331

Paolo Lugli
Dipartimento di Ingegneria Meccanica, II Università di Roma, Via Orazio Raimondo, 00173 Roma, Italy

(Received 20 June 1988)

We have simulated subpicosecond-time-scale pump-and-probe absorption experiments in $Al_xGa_{1-x}As/GaAs$ quantum wells using an ensemble Monte Carlo calculation of the photoexcited electron-hole system. For excess carrier energies less than the optical-phonon energy, our results show that the apparent 200-fs relaxation observed in differential transmission experiments is directly attributable to relaxation of electrons through electron-electron scattering with inelastic electron-hole scattering playing a smaller role. Photoexcited holes are found to thermalize on a 50-fs time scale which is much shorter than the relaxation time of the electrons. However, a nonthermal hole distribution develops *after* the pulse due to optical-phonon absorption at 300 K which should give rise to absorption features at higher photon energies.

Time-resolved optical studies of photoexcitation in semiconductors have provided a unique probe of nonequilibrium carrier relaxation processes in semiconductors on a picosecond and subpicosecond time scale.[1-5] In the experiments of Knox and co-workers[4,5] pump-and-probe absorption spectroscopy was used to study the relaxation kinetics of optically excited carriers in undoped[4] and modulation-doped[5] quantum wells. For nonexcitonic band-to-band absorption, the absorption coefficient depends on the number of occupied initial states and the number of unoccupied final states. For low-level excitation, the differential transmission, $\Delta T/T_0$, is equal to the sum of electron and hole distributions

$$\Delta T(h\nu,t)/T_0 = f_e(\mathbf{k},t) + f_h(\mathbf{k},t) , \quad (1)$$

where $f_e(\mathbf{k},t)$ and $f_h(\mathbf{k},t)$ are the time-dependent electron and hole distribution functions for a wave vector $\mathbf{k}$ corresponding to a photon energy of $h\nu$. In the experiments of Knox and co-workers, the pump energy was chosen such that the electron excess energy, $\Delta E_c = \hbar^2 k^2/2m_e$, was less than the optical-phonon energy. A peak in the differential transmission was observed centered at the pump-probe energy which was attributed to absorption saturation due to a nonequilibrium distribution of photogenerated electrons and holes. Two hundred femtoseconds after the peak of the pump pulse, the differential transmission spectrum was observed to relax to a Maxwellian line shape. The observed relaxation in the differential transmission spectra was therefore argued to result from electron-electron scattering as optical-phonon emission was prohibited. To the extent in which this experiment simulates the time evolution of an isolated system (i.e., no energy transfer to the lattice and constant particle number after the pulse), the observed relaxation after the pulse is a direct consequence of Boltzmann's H theorem[6] which predicts that an interacting system of particles in an arbitrary initial distribution will evolve along a path of increasing entropy in phase space toward the equilibrium state characterized by a Maxwell-Boltzmann distribution (or Fermi-Dirac at high density).

Monte Carlo simulations of the results of Knox and co-workers[4,5] have been performed for the electron system alone which showed that this relaxation could be explained by electron-electron scattering.[7-9] However, in all such optical experiments, comparable numbers of electrons and holes are present which complicates the analysis since relaxation of the hole distribution contributes to the differential transmission in (1), and inelastic electron-hole scattering is present which may dominate the carrier-carrier scattering.

In order to understand the role that holes play in the apparent carrier relaxation in ultrafast laser experiments, we have included the dynamics of holes into a Monte Carlo simulation of quantum-well systems described in detail elsewhere.[10] We have neglected the complications of band mixing in the hole states[11] and simply considered a square-well potential for heavy-hole states within the effective-mass approximation. Hole generation within the light-hole subbands is neglected due to the lower density of states, and the heavy-hole-to-light-hole transitions are assumed negligible on the time scale of these experiments. Unscreened polar-optical-phonon (POP) scattering and transverse-optical (TO) scattering are included for the holes along with impurity and carrier-carrier scattering (CCS). For TO phonon scattering within the quantized hole system, we use the optical deformation potential scattering rate as calculated by Ridley[12] for quasi-two-dimensional systems. We treat intercarrier scattering through a screened Coulomb interaction as before[8-10] with the effective mass replaced with a reduced mass

$$m_r = 2m_i m_j/(m_i + m_j) , \quad (2)$$

where m_i and m_j are the effective masses of band i and band j which reduces to the intraband mass for $i = j$. We

consider only long-wavelength diagonal screening derived from the matrix random-phase approximation (RPA) as before:[8]

$$\epsilon_D(q) = 1 + \sum_{i,n} q_{in} \frac{f_{in}(0)}{q}, \tag{3}$$

where n is the band index (electrons, heavy holes, etc.) and i is the subband index within each band. The constant q_{in} is given by

$$q_{in} = m^*_{in}/\pi\hbar^2(2\pi e^2/\epsilon_{sc}), \tag{4}$$

with ϵ_{sc} the semiconductor dielectric constant. The occupancy, $f_{in}(0)$, of the bottom of the band is calculated at every time step (5 fs) during the simulation and used to update the CCS rate which changes dynamically during photoexcitation.

In the present communication, we simulate the earlier experiments of Knox *et al.*[4] corresponding to an undoped, 95-Å-wide quantum well with an injected carrier density of 2×10^{10} cm^{-2}. A background density of 2×10^9/cm^2 is assumed for the unintentional doping in the molecular-beam-epitaxial (MBE) layer which is also taken as the ionized-impurity-scattering density. At these low values of the free-carrier and ionized-impurity concentrations, square-well solutions to the Schrödinger equation are virtually identical to those calculated using self-consistent wave functions. We assume a 100-fs laser-pulse duration with a spectral width of 20 meV. As described elsewhere,[10] particles are added to the Monte Carlo simulation in accordance to the temporal and energy dependencies of the pump probe in order to simulate laser excitation. Typically, we use 20000–40000 particles and a 5-fs time step in order to assure the statistical accuracy of the results. We neglect the photon momentum in the optical transition so that electrons and holes are added simultaneously with the same wave vector. Therefore, a certain correlation exists in the initial distribution between electrons and holes which rapidly decays through elastic and inelastic collisions.

Figure 1 shows the simulated results at 300 K for electrons and holes in which the excess energy of the electrons above the conduction band edge is 20 meV corresponding to the experimental conditions of Ref. 4. We plot the average energy of electrons and holes as a function of time during and after the pulse where the peak of the pulse occurs at $t=200$ ps. Both electrons and holes are injected with excess energies below the lattice temperature, with the heavy holes injected at a much lower temperature than electrons due to the large difference in the density of states. A substantial heating of the hole distribution occurs during the first 200 fs after the pulse peak due to TO and POP phonon absorption. A weaker heating of the holes due to inelastic electron-hole scattering is also present. Simulated results with the same model at low temperature show that at least 1 ps is required for the electrons and holes to equilibrate with one another through CCS, which is much longer than the 200-fs heating shown in Fig. 1. Experimentally, lower temperatures are required to completely isolate the effects of intercarrier scattering from that of lattice vibrations.

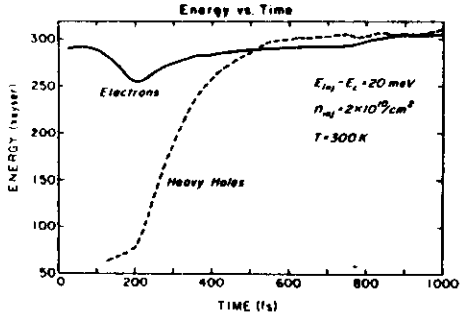

FIG. 1. Energy vs time for electrons and holes at 300 K. The pulse duration is 100 fs and peaks at $t=200$ fs.

In Fig. 2 we plot the instantaneous electron-energy distribution at various times before and after the pulse. An athermal, Gaussian-shaped pulse is observed at time zero which subsequently evolves to a Maxwellian-shaped pulse after 200 fs. The evolution of the electron distribution in Fig. 2 is qualitatively similar to that observed experimentally over the same time scale in the differential transmission spectra. As suggested by Fig. 1, considerable phonon emission and absorption occur at 300 K which complicates the interpretation of the relaxation. Carrier relaxation is driven by inelastic scattering which allows the system to "sample" various regions of phase space. Optical-phonon scattering alone cannot account for the observed relaxation to an equilibrium distribution as the carriers would then simply scatter back and forth between the same constant energy shells separated by $\hbar\omega_0$. By tabulating the energy exchanged per scattering event as a function of time, we are able to determine which scattering mechanism is responsible for relaxation. Energy exchange due to electron-electron scattering was found to be two to three times that of electron-hole and POP phonon scattering on the time scale of Fig. 2 which suggests the former mechanism as the primary driving force for relaxation. Our previous results for electrons alone at low temperature show the same qualitative relaxation over the same time scale which further supports this conclusion.[8,9]

In Fig. 3,we show a similar plot to Fig. 2 for the heavy-hole energy distribution function. The relaxation of the hole distribution occurs within 50 fs which is much sooner than that of the electrons. This difference is due to the larger intercarrier scattering rate corresponding to the larger effective hole mass and due to the fact that holes are injected much closer to the band edge. Perhaps more interesting in Fig. 3 is the appearance of an athermal phonon replica (at 40 meV) in the hole distribution due to TO and POP absorption which peaks after the maximum of the laser pulse. Such a feature has not been observed in previous experimental studies. However, the photon energy which couples this excess hole energy to the conduction band is in excess of 1.7 eV (based on a parabolic band model) which is outside the optically coupled region of

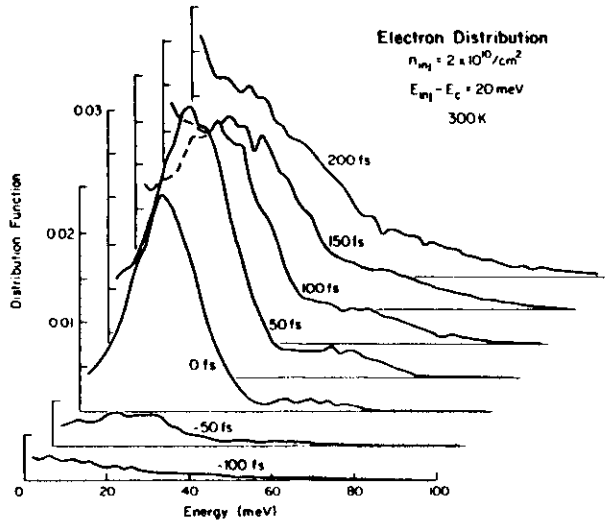

FIG. 2. Electron distribution function as a function of energy at various times before and after a pump pulse at time $t=0$.

those experiments. Time-resolved observation of this feature in absorption experiments could provide a direct measure of the hole–optical-phonon coupling and possible nonequilibrium phonon effects at lower temperatures. As shown in Fig. 3, the athermal phonon replica is observed to smear out with time due to hole-hole scattering and eventually form a Maxwellian tail after 200 fs.

Finally, in Fig. 4 we plot the differential transmission spectra as a function of photon energy at various times using Eq. (2) and the results of Figs. 2 and 3. The excess energies of f_e and f_h coupled by a photon of energy $h\nu$ are chosen to satisfy the momentum conservation rules for band-to-band optical transitions. A quantitative comparison between Fig. 4 and experimental spectra[4,5] is difficult at this time due to the overlap of the excitonic absorption spectrum at low energies which changes dynamically dur-

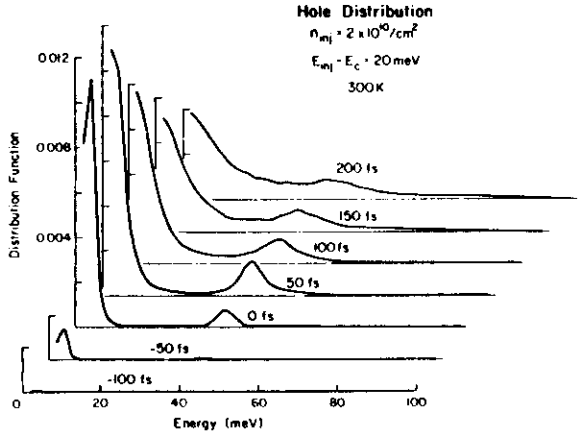

FIG. 3. Hole distribution function as a function of energy at various times during a pump pulse at $t=0$.

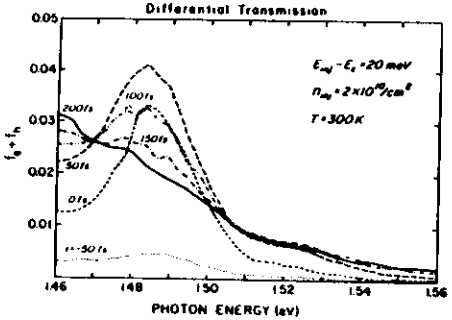

FIG. 4. Differential transmission based on the distribution functions of Figs. 2 and 3 at the same times.

ing photoexcitation.[13] The evolution of the calculated differential transmission spectrum in Fig. 4 is seen to follow that of the electron distribution of Fig. 2 and not that of the holes in Fig. 3 which relaxes much faster. This result supports the original conjecture of Knox *et al.*[4] that their results measured the relaxation of the electron distribution function, at least for the present set of experimental conditions.

In conclusion, our Monte Carlo results for a photoexcited electron-hole plasma in semiconductor quantum wells show that the time-dependent relaxation observed in experimental differential transmission spectra is primarily due to relaxation of the electron distribution. The mechanism for this relaxation is principally through inelastic electron-electron scattering with a lesser contribution due to electron-hole scattering. At 300 K an athermal phonon replica in the hole distribution appears due to POP and TO phonon absorption which should result in absorption spectrum features at large phonon energies. The time evolution of this feature depends strongly on the hole-phonon absorption time as well as hole-hole scattering which broadens this short-time distribution into a thermal tail after several hundred femtoseconds.

The authors would like to thank D. S. Chemla and W. H. Knox for helpful discussions related to this work. The research was supported under the U.S. Office of Naval Research Contract No. N00014-87-K-0686.

[1]J. F. Ryan, R. A. Taylor, A. J. Turberfield, and J. M. Worlock, Surf. Sci. 170, 511 (1986).
[2]D. Y. Oberli, D. R. Wake, M. V. Klein, J. Klem, T. Henderson, and H. Morkoc, Phys. Rev. Lett. 59, 696 (1987).
[3]M. Rosker, F. Wise, and C. L. Tang, Appl. Phys. Lett. 49, 1714 (1986).
[4]W. H. Knox, C. Hirlimann, D. A. B. Miller, J. Shah, D. S. Chemla, and C. V. Shank, Phys. Rev. Lett. 56, 1191 (1986).
[5]W. H. Knox, D. S. Chemla, and G. Livescu, Solid State Electron. 31, 425 (1988).
[6]See, for example, R. C. Tolman, *The Principles of Statistical Mechanics* (Oxford Univ. Press, London, 1938), pp. 134–177.
[7]D. W. Bailey, M. Artaki, C. Stanton, and K. Hess, J. Appl. Phys. 62, 4635 (1987).
[8]S. M. Goodnick and P. Lugli, Appl. Phys. Lett. 51, 585 (1987).
[9]S. M. Goodnick and P. Lugli, Solid State Electron. 31, 463 (1988).
[10]S. M. Goodnick and P. Lugli, Phys. Rev. B 37, 2578 (1988).
[11]M. Altarelli, in *Heterojunctions and Semiconductor Superlattices*, edited by G. Allan, G. Bastard, N. Boccara, M. Lannoo, and M. Voos (Springer-Verlag, Berlin, 1986), pp. 12–37.
[12]B. K. Ridley, J. Phys. C 15, 5899 (1982).
[13]S. Schmitt-Rink, D. S. Chemla, and D. A. B. Miller, Phys. Rev. B 32, 6601 (1985).

-14-

Nonequilibrium Longitudinal-Optical Phonon Effects in GaAs-AlGaAs Quantum Wells

P. Lugli
Dipartimento di Fisica, Università di Modena, 41100 Modena, Italy
and
S. M. Goodnick
Department of Electrical and Computer Engineering, Oregon State University, Corvallis, Oregon 97331
(Received 3 November 1986)

We use an ensemble Monte Carlo technique to study the electron and phonon dynamics in a single quantum well of GaAs-AlGaAs under optical excitation. The cooling of the photoexcited quasi two-dimensional electron distribution is studied in the presence of a nonequilibrium longitudinal-optical phonon population and electron-electron interaction. It is found that the presence of hot phonons due to emission from the photoexcited carriers in the quantum well reduces the electron relaxation rate in qualitative agreement with available experimental results in such systems.

PACS numbers: 73.40.Lq, 63.20.Kr, 72.20.Ht

Recent results from time-resolved studies of the hot-carrier relaxation in GaAs-AlGaAs quantum wells have shown that the relaxation times for photoexcited electrons are much longer than are expected from simple consideration of the bulk electron–longitudinal-optical (LO) phonon interaction.[1–3] Several possibilities have been suggested for this slow cooling rate: (i) enhanced screening of the electron–LO-phonon interaction due to the two-dimensional gas, (ii) reduction in the electron-phonon interaction due to confinement of the lattice modes in the quantum well, and (iii) the presence of a nonequilibrium population of LO phonons. Recent calculations of the effect of dynamical screening of the two-dimensional electron gas on the LO-phonon interaction[4] indicate a 50% reduction in the total scattering due to this effect. This is not enough in itself to account for the difference in relaxation rates observed experimentally. The existence of "slab" modes of the optical vibrations in confined systems has been studied by Riddoch and Ridley.[5] There it was shown that for wells larger than 150 Å, the difference in scattering rates between slab modes and bulk modes is fairly small. The presence of nonequilibrium hot phonons in bulk systems under high optical excitation has been shown from time-resolved Raman studies.[6] Their effect on the hot-carrier relaxation in bulk GaAs has been calculated analytically by Pötz and Kocevar[7] and found to explain retarded cooling effects observed experimentally in the bulk.[8] For quantum wells, Shah *et al.*[3] have argued that the effect of nonequilibrium phonons is the dominant effect contributing to slow carrier relaxation.

In the present study, we show the importance of nonequilibrium phonon effects in the cooling rates of photoexcited electrons in a quantum well through an ensemble Monte Carlo simulation discussed in detail elsewhere.[9] We consider a single quantum well of GaAs-$Al_{0.23}Ga_{0.77}As$ in our calculation, with the subband energies given by the solution of the one-dimensional square-well potential for a barrier height of 0.28 eV. The two-dimensional electrons are assumed to interact with unscreened bulk LO phonons. The reported effects of screening of the LO phonon interaction and the subsequent effect on cooling vary considerably in the literature both for the bulk and quantum wells and will not be considered here. The scattering rates for both intrasubband and intersubband transitions are calculated fully numerically, similar to other calculations of this mechanism for confined systems.[10,11] Intervalley transfer to the satellite L valleys ($E_{\Gamma L} = 0.283$ eV) is included in the calculation where the L valleys are assumed quantized with the same barrier as the central valley. We have introduced two-dimensional electron-electron scattering into the Monte Carlo simulation through a generalization to multisubband systems of the self-scattering technique of Brunetti *et al.*[12] used for bulk Ge. Both intrasubband and intersubband scattering are considered, in which the various electrons are allowed to interact via a static screened Coulomb interaction determined by the long-wavelength limit of the two-dimensional Lindhard dielectric function at low temperature. In this approximation, the intersubband scattering rate is found to be negligible (intersubband in the sense that one of the participant electrons changes subbands after scattering), while the intrasubband rate (which includes scattering between electrons of different subbands) is at least an order of magnitude greater than the LO-phonon rate so that energy is exchanged between subbands allowing them to thermalize within a short time. Degeneracy in the quasi two-dimensional system is included through a generalization of the self-scattering technique proposed by Bosi and Jacoboni.[13,14] Electron-hole scattering has been neglected in this study. This effect may be important in the reported experiments, particularly at high excitation densities on undoped samples. For now we will concentrate

-15-

on n-type samples with relatively low injection densities.

The nonequilibrium phonon distribution is given directly by a detailed balance of emission and absorption events during the simulation. On the time scales involved in the simulation, the group velocity of LO phonons is sufficiently small to neglect diffusion away from the well region. Because of confinement in the quantum well, there is not conservation of the component of the phonon wave vector q_z normal to the well. For an infinite well it has been shown[10] that the probability of scattering with a particular q_z is very peaked around momenta associated with the energy between the initial and final subband. Thus, for intrasubband scattering, phonons are emitted and absorbed with normal wave vectors close to zero, while intersubband events occur for $q_z \neq 0$. We assume that the overlap in momentum space of the various probabilities is small so that we may consider independent two-dimensional nonequilibrium phonon populations occurring for each q_z associated with each possible intersubband and intrasubband scattering event. For each value of q_z, the phonon population as a function of q (the magnitude of the parallel wave vector) is calculated and continually updated. The nonelectronic contributions (phonon-phonon and phonon-boundary scattering) are introduced via a phenomenological lifetime. No direct measurement of the LO-phonon lifetime in quantum-well systems is available at this time and thus a value of 7 ps is used here corresponding to the measured value for bulk GaAs at 77 K from Raman studies.[6] As the phonon population evolves in time, a self-scattering rejection technique is used to account for the modification of the scattering rate induced by the phonon perturbation.

The cooling of photoexcited electrons in n-type GaAs-AlGaAs quantum wells at low temperature (5 K) has been simulated. At each time step of the simulation (10 fs) carriers are added monoenergetically 0.25 eV above the lowest subband minima according to the generation rate of the laser pulse. The evolution in time of the generation rate is taken as an inverse hyperbolic cosine function of width 0.6 ps which peaks at 1 ps into the simulation. A cold background electron density of $2.5\times10^{11}/\mathrm{cm}^2$ is considered, similar to experimental studies on n-type samples.[3] Well widths of 50, 150, and 250 Å were considered with up to six subbands included (depending on the well width and height). Parameters for GaAs (including intervalley coupling constants) are essentially the same as used by Littlejohn, Hauser, and Glisson.[15]

Figure 1 shows the initial electron relaxation for an injected density of $5\times10^{11}/\mathrm{cm}^2$ and a 150-Å well width (four subbands allowed). The electron energy distribution function, $N(E)$, is plotted at different times during and after the laser excitation. The solid curve in the top figure represents the initial cold background electrons. At the maximum of the laser pulse ($t=1$ ps in this plot), a significant transfer of energy from the photoexcited electrons to the background electrons has already occurred. Furthermore, energy loss to the lattice through LO phonons has also occurred as shown by the secondary peak one phonon energy below the injection level. Shortly after the end of the pulse ($t=1.6$ ps), the strong intercarrier scattering creates a broad distribution where the subband minima (indicated by arrows) clearly appear. Within each subband, the distribution function starts to exhibit a Fermi-type appearance which is fully established at longer times as shown in the bottom curve. As a result of the spreading of the pulse arising from intercarrier scattering and hot phonons, a considerable number of electrons are excited above the minima of the satellite L valleys leading to intervalley transfer. This number depends strongly on the background density of cold carriers which absorb the energy of the high-energy injected electrons preventing transfer. For the densities considered here, typically 5%–15% of the injected electrons transfer within the first 4 ps of the simulation where they cool and retransfer back to the central valley within 10 ps. As the L-valley energy is close to that of the AlGaAs barrier, it is expected that a real-space transfer of carriers should occur as well. Although not modeled here, it is expected that the effect will be qualitatively the same as for intervalley transfer.

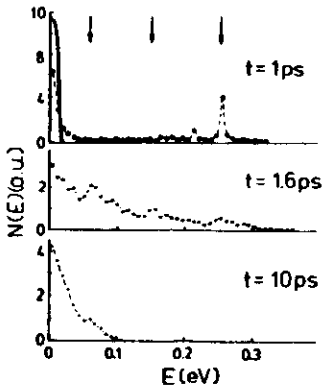

FIG. 1. Electron distribution function for various times before (solid curve), during (1 ps), and after (1.6, 10 ps) laser excitation. The arrows indicate the energy of higher subbands relative to the ground state.

The electron relaxation towards equilibrium is accompanied by a buildup of the LO-phonon distribution due to the large energy loss via LO-phonon emission in the initial phase of the relaxation. Figure 2 shows the phonon distribution as a function of the phonon wave-vector component parallel to the well for $q_z=0$ at times during and after the laser pulse. For polar optical scattering, energy and momentum conservation set a lower limit on the parallel wave vector of the participating phonons which decreases with increasing electron energy [see, for

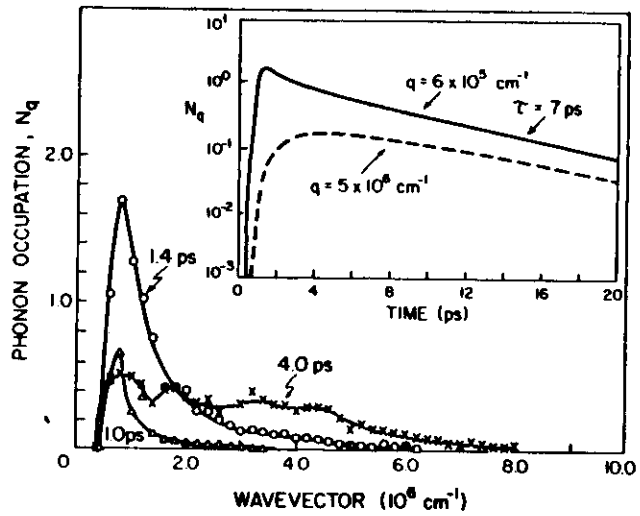

FIG. 2. Density of occupied phonon modes as a function of total parallel momentum for times during and after laser excitation for $q_z=0$ corresponding to intrasubband scattering. Inset: The decay vs time for $q=6\times10^5$ cm^{-1} (solid line) and $q=5\times10^6$ cm^{-1} (dashed curve).

example, Eq. (19) in Ref. 10]. For electrons injected at 0.25 eV, the minimum phonon wave vector for emission is 4.7×10^5 cm^{-1} which corresponds to the long-wavelength cutoff in the distribution of Fig. 2. The peak in the phonon distribution at $q=1\times10^6$ cm^{-1} corresponds to phonons emitted by the energetic photoinjected electrons during their initial relaxation. However, as the electrons thermalize through e-e scattering and phonon emission, phonons are emitted by electrons with energies close to the phonon emission threshold (35 meV). The minimum emitted phonon wave vector for electrons at this energy is 2.4×10^6 cm^{-1} and thus an increase in the nonequilibrium phonon population at longer times will occur at shorter wavelengths. This is evidenced in Fig. 2 for $t=4$ ps where a buildup of the phonon distribution around $q=4\times10^6$ cm^{-1} is observed. The minimum wave vector for phonon reabsorption also increases as the distribution cools which suggests that the population at small q as measured by Raman studies[6] is primarily governed by phonon relaxation and not by reabsorption. The inset in Fig. 2 shows the phonon population as a function of time for long-wavelength phonons ($q=6\times10^5$ cm^{-1}) and for phonons at $q=5\times10^6$ cm^{-1}. After a rapid initial decrease from the peak value, the long-wavelength population decreases with the 7-ps time constant assumed in the simulation as shown in the inset for $t>5$ ps. For the large-wave-vector population, the buildup in the distribution is delayed by several picoseconds in comparison, and the decay is slower because of continued emission, approaching the 7-ps rate at much longer times. For $q_z\neq0$ (corresponding to phonons generated through intersubband events), qualitatively similar behavior in the phonon population is found.

The induced LO-phonon perturbation feeds back into the electron system and is responsible for a reduction in the cooling rates, as shown in Fig. 3. There, the evolution of the average energy per electron (kinetic plus potential relative to the lowest subband) is presented as a function of time during and after the laser pulse. Note that the average energy may vary considerably from the electron temperature measured experimentally when the system is degenerate. If the phonons are forced to maintain an equilibrium distribution, the hot electrons are found to reach the equilibrium average energy shown by the dashed line in Fig. 3 (half of the Fermi energy at 5 K for a total concentration of $5\times10^{11}/\mathrm{cm}^2$) in about 3 ps. A much slower relaxation is found when nonequilibrium phonons are accounted for, as shown by the two curves in Fig. 3, corresponding to two different injected densities of (2.5 and 5)$\times10^{11}/\mathrm{cm}^2$. The reduction of the electron cooling rates is due to reabsorption of nonequilibrium phonons which build up at the earliest stages of the relaxation, as seen in Fig. 2. The effect is stronger when a considerable number of electrons have relaxed to the low-energy region below the emission threshold, resulting in the long-time tail in the average energy seen in Fig. 3. In this regime, the rates of LO-phonon emission and absorption are almost the same so that the energy loss rate is severely reduced. The decay rate in the average energy is thus dependent primarily on the phonon lifetime

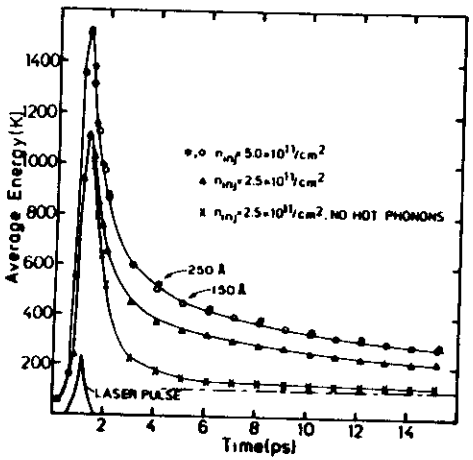

FIG. 3. Average total energy (kinetic plus potential) vs time for two different injection densities. The dashed curve represents the equilibrium energy at 5 K for a total carrier concentration of $5.0\times10^{11}/cm^2$. For $n_{inj}=5.0\times10^{11}/cm^2$, results are shown for well widths of 150 Å (circles) and 250 Å (asterisks).

and by variation of this parameter, proportional changes in the cooling are found in the results. A difference in the cooling between the two injection levels arises because more energy is pumped into the system at the higher injection density and thus a higher peak temperature is reached. The decay rate for the two curves in Fig. 3 is qualitatively the same since the energy loss is primarily governed by the phonon decay once the emission and absorption rates become comparable. However, at longer times when phonon reabsorption effects are strong, electron-hole scattering will reduce the energy by losses through transverse optical modes coupling to the holes,[7] increasing the cooling rate shown, especially at higher injection densities where the electron and hole concentrations are similar. This effect has not been studied in quantum-well systems and will be the subject of future work. As shown in Fig. 3, there is little difference between the cooling rate for a 150-Å (circles) well width and a 250-Å (asterisks) well (six subbands included) for the given injection level. The same result was found when a 50-Å well was considered. Experimentally, Ryan *et al.*[1] found differences between 150- and 250-Å wells in time-resolved experiments for times longer than 20 ps, which is longer than the time scale of Fig. 3. For longer times, other effects not considered here such as electron-hole interaction and recombination play an important role which could account for such differences.

We thank R. Brunetti, C. Jacoboni, and P. Kocevar for many useful discussions regarding this work. The authors acknowledge the support of IBM Corporation and the Alexander von Humboldt Foundation in making this work possible.

[1]J. F. Ryan, R. A. Taylor, A. J. Turberfield, and J. M. Worlock, Surf. Sci. 170, 511 (1986).
[2]Z. Y. Xu and C. L. Tang, Appl. Phys. Lett. 44, 692 (1984).
[3]J. Shah, A. Pinczuk, A. C. Gossard, and W. Wiegmann, Phys. Rev. Lett. 54, 2045 (1985).
[4]S. Das Sarma, W. L. Lai, and X. C. Xie, in *Proceedings of the Eighteenth International Conference on the Physics of Semiconductors, Stockholm, Sweden, 1986*, edited by O. Engström (World Scientific, Singapore, 1987), p. 651.
[5]F. Riddoch and B. Ridley, Physica (Amsterdam) 134B, 342 (1985).
[6]N. von der Linde, J. Kuhl, and H. Klingenburg, Phys. Rev. Lett. 44, 1505 (1980).
[7]W. Pötz and P. Kocevar, Phys. Rev. B 28, 7040 (1983).
[8]R. F. Leheny, J. Shah, R. F. Fork, C. V. Shank, and A. Migus, Solid State Commun. 31, 809 (1979).
[9]S. M. Goodnick and P. Lugli, to be published.
[10]F. A. Riddoch and B. K. Ridley, J. Phys. C 16, 6971 (1983).
[11]K. Yokoyama and K. Hess, Phys. Rev. B 31, 6872 (1985).
[12]R. Brunetti, C. Jacoboni, A. Matulionis, and V. Dienys, Physica (Amsterdam) 134B, 369 (1985).
[13]S. Bosi and C. Jacoboni, J. Phys. C 9, 315 (1976).
[14]P. Lugli and D. K. Ferry, IEEE Trans. Electron Devices 32, 2431 (1985).
[15]M. A. Littlejohn, J. R. Hauser, and T. H. Glisson, J. Appl. Phys. 48, 4587 (1977).

-18-

Effect of electron-electron scattering on nonequilibrium transport in quantum-well systems

S. M. Goodnick
Department of Electrical and Computer Engineering, Oregon State University, Corvallis, Oregon 97331
P. Lugli
Dipartimento di Fisica, Università di Modena, 41100 Modena, Italy
(Received 22 June 1987)

We model nonequilibrium transport in a GaAs-$Al_xGa_{1-x}As$ quantum-well structure using an ensemble Monte Carlo simulation of the full multisubband system in which we include electron-electron (*e-e*) scattering explicitly into the calculation. The *e-e* scattering cross section is calculated using the Born approximation and introduced into the transient Monte Carlo simulation via a self-scattering technique. This interaction is found to be especially effective in transferring energy between different subbands, thus thermalizing the carriers within a picosecond. The model described herein is applied to the study of laser-excited carriers in a quantum-well system and to the response of such a system to high parallel electric fields. In the case of laser excitation, *e-e* interaction may dominate the initial evolution, reducing the cascade of carriers via optical-phonon emission.

I. INTRODUCTION

Recent time-resolved bleaching studies of the initial relaxation of photoinjected carriers in bulk GaAs (Ref. 1) and GaAs-$Al_xGa_{1-x}As$ (Ref. 2) quantum wells (QW) have shown the apparent evolution of the electron distribution as a function of time on the subpicosecond time scale. On this time scale, the electron (and hole) distribution functions evolve from a highly nonequilibrium Gaussian pulse centered around the excitation energy in the band to a heated Maxwellian (thermalized) distribution on the order of a few tenths of a picosecond. This time scale is short enough that polar-optical-phonon (POP) scattering has not relaxed a significant portion of the energy, and thus the distribution is thermalized through intercarrier interaction. Time-resolved photoluminescence measurements have also been reported which show that the distribution function on the picosecond time scale is thermalized and Fermi-like.[3-5] However, under certain conditions, cw luminescence experiments show a cascadelike distribution arising from successive phonon emission of electrons as they cool.[6] In these experiments carrier-carrier scattering is less dominant and a nonthermal distribution is maintained.

In the present work we model the picosecond time-scale dynamical behavior of electrons confined in a quantum well using an ensemble Monte Carlo simulation which includes *e-e* scattering, degeneracy, and the inclusion of nonequilibrium phonons. We previously used this model to simulate the dynamics of photoexcited carriers in a QW system, the results of which showed that carrier cooling in such systems is controlled by hot-phonon buildup.[7,8] Here we present details of the model used in the previous work and apply it to the study of the subpicosecond response in quantum-well systems to both optical and electrical excitation. In the present paper we will concentrate on the model for *e-e* scattering in a QW system and reserve discussion of hot phonons for future work. In the next section (II), details of the Monte Carlo transport simulation for a model QW system are given. The following section (III) will show the results of this simulation for the steady-state distribution function of electrons subject to an applied electric field. Results will then be presented for the carrier evolution under laser excitation in the presence of *e-e* scattering assuming temperature-independent screening. This evolution, which depends substantially on the electron density, is found to evolve as a cascade of phonon emission only for very low injected densities (10^{10} cm^{-2}). For higher densities, *e-e* scattering broadens the injected carrier energy sufficiently fast to wash out peaks in the distribution arising from phonon emission. Due to the high rate of intersubband energy exchange, a common energy is achieved between the different subbands shortly after the end of the laser pulse.

II. MODEL

In the present section we describe the model used in calculating the nonequilibrium response of a quantum-well system using an ensemble Monte Carlo simulation. Results of Monte Carlo simulation on transport in quasi-two-dimensional systems have been reported previously by other authors.[9-11] In our model for the quantum-well system, all scattering rates are calculated from their two-dimensional forms including both intra- and intersubband scattering processes. We have included the effects of polar-optical-phonon scattering (bulk modes), intervalley scattering with the satellite L valleys, also assumed quantized, impurity scattering (from a

-19-

sheet of impurities[12], and finally electron-electron scattering. Degeneracy of the final state is also accounted for in our simulation so that low-temperature transport may be modeled. Typically, in the ensemble Monte Carlo we model the motion of 2000–5000 electrons whose free flight times and scattering events are generated stochastically from the various probabilities for scattering and the random-number generator on the computer. From this we tabulate the instantaneous distribution function of the electrons (and phonons when nonequilibrium effects are included) from which various macroscopic quantities may be calculated. In the following, we detail the model employed in the description of the quantum-well system and of the various scattering mechanisms. We also discuss the algorithm used to incorporate multisubband *e-e* scattering and degeneracy effects into the Monte Carlo simulation.

A. Quantum-well system

As a model quasi-two-dimensional system, we consider a finite square-well potential defined by the conduction-band offset between undoped GaAs and $Al_{0.23}Ga_{0.77}As$ which we take as 0.28 eV. The subband energies and eigenfunctions in the central valley are calculated from the solution of the one-dimensional effective-mass equation for this potential. The envelope functions then satisfy the separable form[13]

$$\Psi(R)=\xi_i(z)e^{ik\cdot r}/A \ , \tag{2.1}$$

where R is the position vector, r and k are the position and wave vectors in the plane parallel to the well, z is the normal direction, and A is the normalization area. The scattering rates discussed below are calculated fully numerically, and thus we are not limited to a simple square well employed here for simplicity. Results using a full self-consistent calculation including exchange and correlation effects have been discussed elsewhere.[11] We consider the L valley as quantized although the barrier height in the upper valleys is not well known and is expected to be less than that of the central valley. Here we assume the same barrier in the L valley as the central valley (0.28 eV) and assume solutions in the form of (2.1).

B. Polar optical scattering

Longitudinal polar-optical-phonon scattering is a dominant energy-loss mechanism in GaAs, at least at high carrier temperatures. In the quantum well we assume that the two-dimensional (2D) electrons interact with bulk phonon modes via the Fröhlich interaction.[14,15] Quantization of the phonon modes (or slab modes) has been considered to some extent by Riddoch and Ridley,[16] who found significant deviations in the scattering rates for well widths less than about 100 Å. The effect of screening of the longitudinal-optical (LO) interaction is not clear, especially in 2D. Static screening leads to gross overestimation of this interaction, and thus a full dynamical calculation is required.[17,18] If one assumes only bulk screening of longitudinal modes, then the matrix element for scattering is given by[14]

$$|\langle \mathbf{k}\pm\mathbf{q},j|H|\mathbf{k},i\rangle|^2=\frac{2\pi\hbar^2eE_0(q^2+q_z^2)}{Vm^*(q^2+q_z^2+q_s^2)^2}\times(n_{\omega_0}+\tfrac{1}{2}\mp\tfrac{1}{2})|G_{ij}(q_z)|^2 \ , \tag{2.2}$$

where q and q_z are the parallel and normal components of the phonon wave vector, q_s is the 3D inverse screening length, m^* is the effective mass, i and j denote the initial and final subband indices, and the effective field eE_0 is given by

$$eE_0=\frac{m^*e^2\hbar\omega_0}{\hbar^2}\left|\frac{1}{\kappa_\infty}-\frac{1}{\kappa_0}\right| \ , \tag{2.3}$$

with κ_0 and κ_∞ the low- and high-energy dielectric constants, and $\hbar\omega_0$ is the phonon energy. The overlap integral $|G_{ij}(q_z)|^2$ is given by

$$|G_{ij}(q_z)|^2=\int_{-\infty}^{\infty}dz\int_{-\infty}^{\infty}dz'\rho_{ij}(z)\rho_{ij}^*(z')e^{iq_z(z-z')} \ , \tag{2.4a}$$

$$\rho_{ij}(z)=\xi_i^*(z)\xi_j(z) \ , \tag{2.4b}$$

between initial and final subbands. This function, which is related to the momentum uncertainty due to the spatial confinement of the electrons, is peaked for q_z corresponding to the parabolic momentum associated with the initial- and final-state subband energies. By converting the sum over q_z to an integral, the q_z dependence may be integrated analytically to yield a smooth function which is better suited for numerical evaluation of the scattering rate. Thus we define the function

$$I(q,z,z')=\int_{-\infty}^{\infty}dq_z\frac{(q^2+q_z^2)}{(q^2+q_z^2+q_s^2)^2}e^{iq_z(z-z')} \ , \tag{2.5}$$

which may be evaluated by contour integration to yield

$$I(q,z,z')=\frac{\exp[-(q^2+q_s^2)^{1/2}|z-z'|]}{(q^2+q_s^2)^{1/2}}\times\left[1-\frac{|z-z'|q_s^2}{2(q^2+q_s^2)^{1/2}}-\frac{q_s^2}{2(q^2+q_s^2)}\right] \ , \tag{2.6}$$

which in the unscreened case ($q_0=0$) gives the same result as Price.[19] The total scattering rate may thus be written

$$\Gamma_{ij}(k)=\frac{eE_0}{2\hbar}\left[n_{\omega_0}\int_0^{2\pi}\frac{H_{ij}(q_+)}{(q_+^2+q_z^2)^{1/2}}+(n_{\omega_0}+1)\int_0^{2\pi}d\theta\frac{H_{ij}(q_-)}{(q_-^2+q_z^2)^{1/2}}\right] \ , \tag{2.7}$$

where the function H_{ij} is defined from the integration over the envelope functions

$$\frac{H_{ij}(q)}{(q^2+q_z^2)^{1/2}}=\int_{-\infty}^{\infty}dz\int_{-\infty}^{\infty}dz'\rho_{ij}(z)\rho_{ij}^*(z')I(q,z,z') \tag{2.8}$$

with $I(q,z,z')$ given in (2.6). The + and − signs on q in (2.7) refer to absorption and emission, respectively, for the scattered wave vector given by

$$q=|\mathbf{k}-\mathbf{k}'|=\left|2k^2\pm\frac{2\omega_{ij}^*m^*}{\hbar}-2k\left|k^2\pm\frac{2\omega_{ij}^*m^*}{\hbar}\right|^{1/2}\cos\theta\right|^{1/2} \ , \tag{2.9a}$$

$$\hbar\omega_{ij}^*=\hbar\omega_0\pm(E_i-E_j) \ , \tag{2.9b}$$

where $\hbar\omega_{ij}^*$ serves as an effective phonon energy which depends on the initial and final subband energies E_i and E_j. The scattering rate (2.7) is shown for a 150-Å well in Fig. 1 where $i=1$ and we sum over j (total scattering rate from the bottom subband). For comparison we plot the 3D rate as well. We take $q_z=0$ for this calculation. As seen in Fig. 1, the 2D rate is a piecewise approximation of the 3D rate due to the discontinuities in the 2D density of states at the various subband energies.

If nonequilibrium phonons are considered, the phonon occupation factors are no longer independent of q and q_z and thus cannot be taken as constant. In the Monte Carlo simulation we can account for this dependence through the use of self-scattering. Here, n_{ω_0} is replaced by its maximum value during the simulation (which must be set *a priori*), and after every scattering event a rejection technique is used to compare the maximum scattering rate to its actual value determined by the instantaneous value of the phonon distribution.

C. Intervalley scattering

Intervalley scattering for two-dimensional systems has been treated previously in connection with Si inversion layers.[20] In the GaAs-$Al_xGa_{1-x}As$ system, it is not clear to what degree quantization plays a role in the upper L and X valleys of the GaAs as the band offset is expected to be smaller there. For simplicity, we consider only quantized upper L valley states in the GaAs with the same barrier as the central valley. For zeroth-order interaction, the matrix element for scattering is given by

$$|H_{\mathbf{kk}'}^{ij}|_{iv}^2=\frac{\hbar E_{iv}^2(n_{\omega_{iv}}+\frac{1}{2}\mp\frac{1}{2})I_{iv}}{2\rho A\omega_{iv}} \ , \tag{2.10}$$

where E_{iv} is the intervalley deformation potential, ρ is the mass density, and ω_{iv} is the intervalley phonon frequency. I_{iv} is an overlap integral given by

$$I_{iv}=\int_{-\infty}^{\infty}dz\,|\zeta_i^v(z)|^2\,|\zeta_j^{v'}(z)|^2 \ , \tag{2.11}$$

where v and v_f refer to the initial and final valley envelope functions. The total scattering rate is thus given by

$$\Gamma_{ij}(k)=\sum_{v_f}m_f^*\frac{E_{iv}^2(n_{\omega_{iv}}+\frac{1}{2}\mp\frac{1}{2})I_{iv}}{2\rho\omega_{iv}\hbar^2} \tag{2.12}$$

with m_f^* being the effective mass in the final-state valley and the sum is over all the final-state valleys. We consider a GaAs(100) layer and thus the subbands of the four satellite L valleys are degenerate.

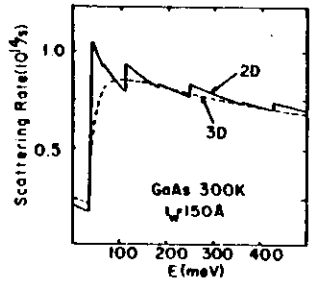

FIG. 1. Total scattering rate due to POP scattering for a 150-Å well for electrons in the first subband (solid line). The dashed line is the 3D scattering rate.

D. Electron-electron scattering

The *e-e* scattering rate in bulk materials has been previously calculated using the Born approximation.[21–24] This method has been criticized as overestimating the scattering rate by as much as 5 times in sodium[22] compared to computation based on the more-accurate phase-shift method, although the degree of this error in semiconductors is not known. As a first approach to this problem in a quantum-well system, we will adopt the Born approximation in our calculation.

We start by considering the scattering rate between an electron in the well with wave vector $\mathbf{k}$ in subband i and a second electron with wave vector $\mathbf{k}_0$ in subband j. The final states of these two electrons are $\mathbf{k}'$ and m for the first electron and $\mathbf{k}_0'$ and n for the second electron. The unscreened matrix element between these two initial and final states may be written

$$H_{\substack{\mathbf{k},\mathbf{k}';\mathbf{k}_0,\mathbf{k}_0'\\ i,m,j,n}}^{ee}=\frac{e^2}{\kappa}\int_{-\infty}^{\infty}dz\int_{-\infty}^{\infty}dz'\int d\mathbf{r}\int d\mathbf{r}'\frac{e^{-i(\mathbf{k}-\mathbf{k}'+\mathbf{k}_0-\mathbf{k}_0')\cdot(\mathbf{r}-\mathbf{r}')}}{[|\mathbf{r}-\mathbf{r}'|+(z-z')^2]^{1/2}}\xi_i(z)\xi_j(z')\xi_m^*(z)\xi_n^*(z') \ . \tag{2.13}$$

Introducing the two-dimensional Fourier transform of the Coulomb potential in (2.13), the matrix element becomes

$$H_{\substack{\mathbf{k},\mathbf{k}';\mathbf{k}_0,\mathbf{k}_0'\\ i,m,j,n}}^{ee}=\frac{2\pi e^2\delta(\mathbf{k}'+\mathbf{k}_0'-\mathbf{k}-\mathbf{k}_0)}{A\kappa q}F_{ijmn}(q) \tag{2.14}$$

with $q=|\mathbf{k}-\mathbf{k}'|$ and the form factor given by

$$F_{ijmn}(q)=\int_{-\infty}^{\infty}dz\int_{-\infty}^{\infty}dz'\zeta_i(z)\zeta_j(z') \times\zeta_m^*(z)\zeta_n^*(z')e^{-q|z-z'|}\,. \tag{2.15}$$

This form factor appears in the 2D random-phase-approximation (RPA) dielectric function[13] and is somewhat similar to that appearing in phonon scattering[15] as well. As will be discussed later, this form factor is important in determining the relative magnitude of the e-e scattering and favors intrasubband over intersubband transitions. Screening in the multisubband 2D system is quantitatively difficult, requiring an inversion of the dielectric matrix in the RPA.[25] For single-subband static screening, the RPA dielectric function in the long-wavelength limit is characterized by a single wave-vector-independent constant (the inverse screening length) which is independent of carrier density at low temperature[26] and proportional to density under nondegenerate conditions.[27] The square of the matrix element is thus given by

$$|H^{sc}|^2=\frac{4\pi^2e^4\delta(\mathbf{k}'+\mathbf{k}_0'-\mathbf{k}-\mathbf{k}_0)}{A^2\kappa^2(q+q_0)^2}\,|F_{ijmn}(q)|^2 \tag{2.16}$$

with q_0 the inverse screening length in two dimensions. For simplicity, we assume q_0 is given by the low-temperature limit in the present results. When temperature-dependent and multisubband effects are included in q_0, the e-e scattering rate is enhanced due to a decrease in the screening constant. Results in which we consider temperature-dependent and multisubband screening are reported elsewhere.[20] In the Born approximation, the total scattering rate out of the first electron in an initial state $\mathbf{k}$, i to a final state in subband m is then calculated from the sum over the final states

$$\Gamma_{im}(k)=\frac{2\pi e^4}{\hbar\kappa A}\sum_{\mathbf{k}_0,j,n}{}'f_j(\mathbf{k}_0)\int d\mathbf{k}_0'\frac{|F_{ijmn}(q)|^2}{(q+q_0)^2} \times\delta(E_i-E_f)\,, \tag{2.17}$$

where use has been made of the δ function in (2.16) to eliminate the sum over $\mathbf{k}'=\mathbf{k}+\mathbf{k}_0-\mathbf{k}_0'$. The δ function in (2.17) represents conservation of energy between the initial and final state and $f_j(\mathbf{k}_0)$ is the carrier distribution function. The prime on the summation indicates that the sum is only over electrons with antiparallel spin. Thus we neglect scattering with carriers at parallel spin which is lower in magnitude than the scattering due to antiparallel electrons due to exchange considerations.[24]

As in the three-dimensional case,[23] it is useful to introduce the relative wave vectors

$$\mathbf{g}=\mathbf{k}_0-\mathbf{k},\quad \mathbf{g}'=\mathbf{k}_0'-\mathbf{k}' \tag{2.18}$$

so that (2.17) may be rewritten

$$\Gamma_{im}(k)=\frac{2\pi e^4}{\hbar\kappa^2A}\sum_{\mathbf{k}_0,j,n}{}'f_j(\mathbf{k}_0)\int d\mathbf{g}'\frac{|F_{ijmn}(|\mathbf{g}-\mathbf{g}'|/2)|^2}{(|\mathbf{g}-\mathbf{g}'|/2+q_0)^2} \times\delta(E_i-E_f)\,, \tag{2.19}$$

and the argument of the δ function between initial- and final-state energies is

$$\delta(E_i-E_f)=\delta\left[\frac{\hbar^2g^2}{4m^*}-\frac{\hbar^2g'^2}{4m^*}+E_z\right] \tag{2.20}$$

with $E_i=E_i+E_j-E_m-E_n$. This δ function may be used then to reduce the integral over g' to

$$\Gamma_{im}(k)=\frac{4\pi e^4m^*}{\hbar^3A\kappa^2}\sum_{\mathbf{k}_0,j,n}{}'f_j(\mathbf{k}_0)\int_0^{2\pi}d\theta\frac{|F_{ijmn}(q)|^2}{(q+q_{s0})^2}\,, \tag{2.21}$$

where q is related to θ, the angle between $\mathbf{g}$ and $\mathbf{g}'$, by

$$q=|\mathbf{g}-\mathbf{g}'|/2 =[2g^2+g_0^2-2g(g^2+g_0^2)^{1/2}\cos\theta]^{1/2}/2\,, \tag{2.22}$$

and g_0^2 is $4m^*E_i/\hbar^2$. In the case of intrasubband scattering, $g_0=0$ and q is simply

$$q=g\sin\theta/2\,. \tag{2.23}$$

The total scattering rate (2.21) depends on the square of the form factor (2.15) which plotted in Fig. 2 for the

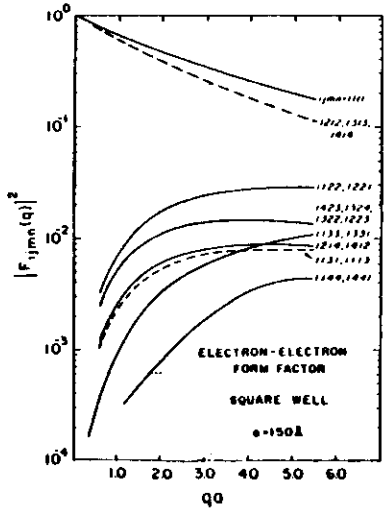

FIG. 2. Electron-electron form factor as a function of wave vector for a 150-Å square well. The indices $ijmn$ label initial and final subband states.

dominant terms involving the first electron in the lowest subband. The dominant term occurs for pure intrasubband scattering ($ijmn=1111$) in which the initial and final subband for both electrons is the lowest subband. Of similar value is the form factor for intrasubband scattering in which the initial subbands of the two electrons are different, although they stay within their respective subbands after scattering ($i=m$ and $j=n$). This inelastic scattering between subbands allows energy to be transferred from hot subbands to cold subbands so that a uniform energy is quickly reached between different subbands. Since $g_0=0$ for intrasubband transitions, the scattering rates are peaked for $q=0$ and small-angle scattering is favored.

The intersubband scattering form factor is much lower in magnitude and vanishes for $q=0$ due to the orthagonality of the eigenfunctions in (2.15). Strong interference effects occur in (2.15) so that certain combinations of initial and final subband states result in negligibly small form factors. For the 150-Å well shown in Fig. 2, the dominant intersubband form factors are shown. The transitions 1221, 1331, and 1441 are exchange transitions in which the first and second electrons exchange subbands. Such transitions are similar in effect to intrasubband scattering as the net particle flux from one subband to another is zero. The other transitions do, however, allow a net intersubband particle diffusion. However, as shown in Fig. 2, the form factor is almost 2 orders of magnitude less than the intrasubband value, and thus the mass transfer rate between subbands may be considerably reduced leading to transient bottleneck effects in the subband populations when the 2D system is driven far from equilibrium. The reduction in intersubband scattering is further enhanced due to the nonzero value of g_0 in the denominator, which decreases the scattering rate. However, a similar form factor to (2.15) multiplies the screening constant as well,[13] so that reduced screening could enhance the intersubband rate. More work is needed on the full multisubband screening in order to determine which effect dominates.

E. Monte Carlo simulation

We have included the various scattering mechanisms discussed above into the framework of an ensemble k-space Monte Carlo simulation. Monte Carlo techniques as applied to semiconductor transport have been reviewed by Jacoboni and Reggiani.[29] For the quasi-two-dimensional QW systems, we include both intra- and intersubband scattering in the simulation, both within the same valley and between different valleys. Only two-dimensional transport has been considered in the plane parallel to the well, and thus vertical transport effects over the well (such as real-space transfer) are not included in the simulation. For the results presented here, we neglect any screening of the phonon modes and thus $q_s=0$ in (2.7). Typically, we follow an ensemble of 5000 electrons from which we calculate the electron distribution function, the mean velocity, and mean energy in each subband.

The exclusion principle modifies the scattering rates discussed previously, and this effect must be included in the nonequilibrium behavior at low temperatures and high carrier densities. The inclusion of this effect in a Monte Carlo simulation has been reported by Bosi and co-workers[30] In the multisubband QW system, we account for degeneracy by tabulating the electron distribution function within each subband during the simulation using a self-scattering rejection technique to accept or reject scattering events based on the final-state occupancy.[31] Using this technique (and including e-e scattering discussed below), the equilibrium distribution function in the Monte Carlo simulation attains the proper Fermi-Dirac function of the multisubband system.

The inclusion of hot phonons in the simulation is accomplished through a detailed balance of LO-phonon emission and absorption from which the phonon distribution function is determined. From this distribution function, the electron-phonon scattering rate is subsequently updated through (2.7).[1,8] A variable self-scattering is used to account for the change of this rate during the simulation.

We include e-e scattering into the QW simulation using a modification of the self-scattering technique proposed by Brunetti *et al.*[32] for the bulk. Here we take the full multisubband scattering rate given by (2.21) and maximize the quantity inside of the integral, i.e., choose a maximizing function that is integrable, calculate the total scattering rate based on the new function, and account for the actual value of the function when the final state is chosen through a rejection method. For the intrasubband scattering rate in (2.21), we note that the integrand is sharply peaked at $q=0$ corresponding to $\theta=0$ and 2π. Since the form factor is always unity or less, the maximum value of the integrand is always less than $1/q_0^2$. Thus, the maximum scattering rate is given by

$$\Gamma_{\max,ii}=\frac{4\pi^2e^4m^*N_s}{\hbar^3\kappa^2q_0^2}\,, \tag{2.24}$$

where N_s is the total sheet density of the QW and the total rate has been multiplied by $\frac{1}{2}$ due to neglect of parallel spin scattering. This scattering rate is used to generate the free flight time during the simulation. Similarly, for intersubband scattering, the maximum scattering rate from an initial subband i to a final subband m may be written

$$\Gamma_{\max,im}=\Gamma_{\max,ii}F_{\max}^2N_{\text{sub}}\,, \tag{2.25}$$

where N_{sub} is the total number of subbands, and $F_{\max}$ is the maximum value of the form factor, (2.15), for intersubband scattering (which is much less than unity as seen in Fig. 2). When e-e scattering is chosen, another electron is chosen at random from the ensemble, and the scattering angle is chosen at random according to the flat distribution associated with the maximizing function. Using another random number between zero and the maximum value of the integrand ($1/q_0^2$), the actual value of the integrand is compared to that of the random number, and the scattering is rejected if the integrand is less than this number. In this case, the electron and its counterpart are then allowed to continue on their origi-

nal flights unchanged. If the random number is less than the integrand value, then the scattering is accepted, the momentum and energy changed accordingly, and a new flight generated. In this technique, considerable computation time is lost via self-scattering events. Depending on the exact electron dynamics, the number of self-scattering events may be 10–100 times the number of real events. However, considerable savings in time is achieved because the scattering rate does not have to be continually recalculated as the electron distribution function changes. Also, the algorithm is quite simple to implement in the context of the usual Monte Carlo program. Degeneracy effects are also included by checking the occupancy of the final states of both electrons and using a rejection technique as discussed earlier.

In general, the total number of particles is not constant (e.g., during optical injection). Also, the screening constant depends strongly on the electron distribution which changes as well, and thus the e-e scattering rate changes during the simulation. Therefore, at the beginning of the simulation, the maximum e-e scattering rate which will occur during the simulation must be known. During the simulation, the e-e rate will vary within this maximum rate. The tabulation of all the scattering rates used to generate the termination of the electron free flights is shown schematically in Fig. 3. When the free flight of the electron is ended, a random number between 0 and Γ is chosen, selecting one of the mechanisms shown in Fig. 3. As shown, self-scattering is divided between e-e scattering and the other scattering mechanisms. If e-e scattering is chosen to terminate a flight, we first check to see if this is a real event or self-scattering. Then as discussed above, a second possibility for self-scattering arises from the choice of final state and degeneracy. The accuracy of this method is improved as the number of simulated particles is increased and if time steps that are shorter than the collision time are used (the time over which the distribution can change appreciably). We use a time step of 10 fs in the present work which satisfies this requirement. Satisfactory results were obtained with 5000 electrons, and the results were not found to vary with the inclusion of more particles (only the statistical uncertainty is improved). We include e-e scattering only for the central valley electrons and neglect this interaction in the L valley.

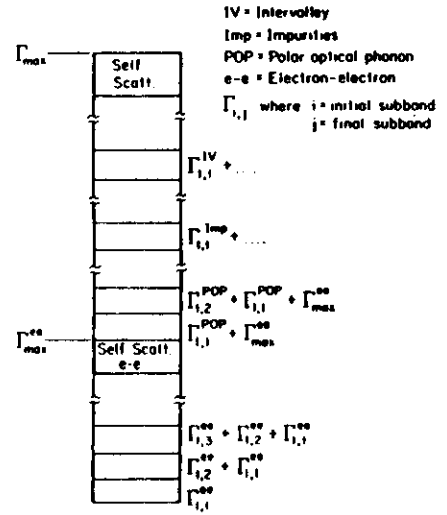

FIG. 3. Histogram of the various scattering rates in the Monte Carlo simulation.

III. RESULTS AND DISCUSSION

A. Hot-carrier behavior in a uniform electric field

Electron-electron scattering exchanges energy between carriers thus redistributing the energy gained by an electric field and driving the electron distribution function towards a Maxwellian-type distribution. In polar semiconductors, the threshold in energy for optical-phonon emission results in a sharp increase in the scattering rate which tends to deplete the population of electrons above the threshold energy. Thus, in the presence of strong polar-optical-phonon scattering, the electron distribution function cuts off at the emission threshold, while e-e scattering has the effect of repopulating the high-energy tail. Figure 4 shows the steady-state electron distribution function in the lowest subband with and without e-e scattering in a uniform field of 0.5 kV/cm at 20 K. A carrier density of 4×10^{11} cm^{-2} was assumed which is a typical value for GaAs-Al$_x$Ga$_{1-x}$As quantum wells. Hot phonons were not considered in the results in which electric fields were present. Without e-e scattering, the distribution function is well represented by a two-temperature model in which electrons above the threshold are depleted to lower energies via phonon emission. The kink in the distribution function is removed with e-e scattering present due to inelastic scattering above the phonon threshold. Such a result has been observed in bulk Monte Carlo simulation of e-e interaction as well.[23]

In Fig. 5 we show the electron occupation versus energy for a 258-Å well with four subbands in the well. The energies of the subband levels are shown by the arrows in Fig. 5. The normalized electron density (which is the distribution times the density of states) is shown for three different applied electric fields corresponding to the fields used by Shah *et al.*[33] in studying the carrier heating in similar width quantum wells using photoluminescence (PL). At the first excited subband energy, a kink in the density is observed in Fig. 5 due to the presence of carriers in the second subband, similar to the results of PL studies. We see very little structure in the occupation at the next subband however. In fact, we see a depletion of the higher subbands due to the fact that electron may transfer from a higher subband to a lower one by phonon emission for any energy (unless the subband spacing is less than the phonon energy). However, to make an intersubband scattering to a higher subband via

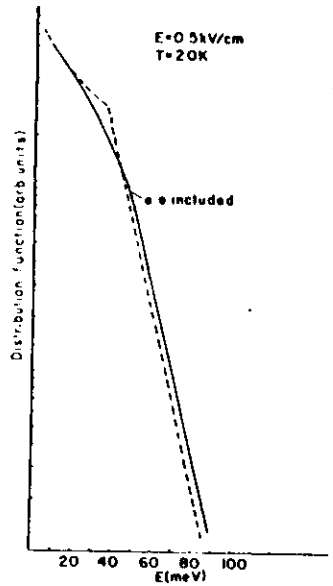

FIG. 4. Steady-state electron distribution function for an applied field of 0.5 kV/cm in a single subband system.

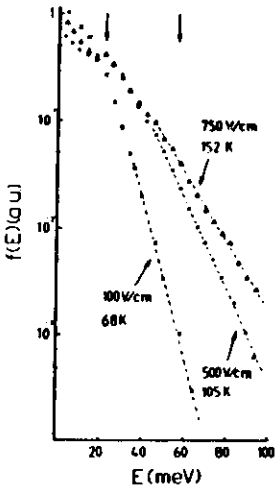

FIG. 5. Steady-state distribution function for a 258-Å well for various applied electric fields. The arrows denote the energies of the first and second excited subbands.

phonon emission requires that the electron be one phonon energy above the subband energy itself. Since at low temperature absorption is negligible, there is a tendency towards depleting the bottoms of the higher subbands. This is still found to be true with e-e scattering present in the constant screening approximation as the intersubband e-e scattering rate is less than that of POP scattering.

The carrier "temperatures" are found from the high-energy slope as shown in Fig. 5. We find values of 68, 105, and 152 K for electric fields of 100, 500, and 750 V/cm, respectively. Note that these temperatures do not correspond to the average carrier energies due to the effect of degeneracy, the latter values being larger. The electron temperatures measured in PL studies are 100, 145, and 165 K for the same fields[33] which are consistently higher than those calculated here. The reason for this difference is not understood at this time, although screening of the LO interaction or hot phonons could play a role.

In Fig. 6 we show the transient electron drift velocity as a function of time for an electric field of 5 kV/cm applied at time $t=0$ to an electron gas originally at 77 K in equilibrium. The results are shown both with and without e-e scattering and the difference is very marginal due to the fact that the total wave vector of both electrons is conserved for e-e scattering, and therefore no change in the momentum in the direction of the field is expected. As shown by the dashed line of Fig. 6, electrons are accelerated quasiballistically during the first 0.2 ps even though numerous e-e collisions have occurred during this time interval.

B. Photoexcitation into the quantum well

Numerous investigations have been made of the relaxation of hot carriers injected into multiple quantum wells.[34] The initial relaxation dynamics are strongly

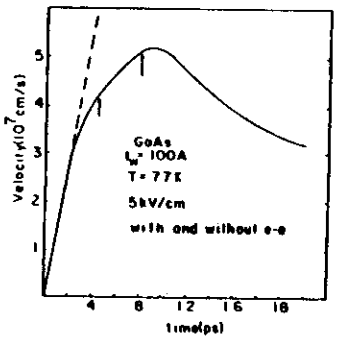

FIG. 6. Velocity vs time after an applied electric field of 5 kV/cm to a 100-Å well (two subbands). The arrows denote the onset of intersubband transfer (first arrow) and intervalley transfer. The dashed curve is the velocity free acceleration of the carriers without collisions.

influenced by e-e interaction. If e-e scattering is weak, the injected electrons relax in a cascade of subsequent polar-optical-phonon emission. The nonequilibrium distribution would appear as a series of peaks starting at the injection energy and separated by $\hbar\omega_0$ to the bottom of the band. If e-e scattering is strong, then the electrons are scattered several times before optical-phonon emission and thus memory of the initial injection energy is eliminated. In this case, electrons cool by phonon emission from a thermalized distribution rather than a cascade.

To study the initial dynamics, we simulate the injection of carriers monoenergetically into the conduction band of the quantum well. To model the time dependence of the carrier injection through femtosecond laser excitation, we add carriers monoenergetically into the Monte Carlo simulation according to the following equation:[35]

$$G(t)=I_0\cosh^{-2}(2.634t/t_p)\,, \tag{3.1}$$

where I_0 is the incident intensity which we choose to match the total number of injected carriers, and t_p is the half-width of the pulse. Extra particles are added to the simulation during each time step according to (3.1). To account for spectral broadening of the pulse, the carriers are introduced according to a Gaussian distribution 20 meV wide around the injection energy. Hot phonons are also included here due to their dominant effect in the energy relaxation.[7]

In Fig. 7(a) we show the result for a 500-fs pulse and a relatively small injection density of 5×10^{10} cm^{-2} at different times starting at the end of the laser pulse (the peak of the pulse occurs at 0.7 ps). Here we assume a well width of 150 Å and a small background density of 1×10^{9} cm^{-2} at 5 K. Carriers are injected 150 meV above the bottom of the band. We plot the total occupancy as a function of energy for all the subbands, which is the distribution function times the density of states. As shown, a cascade in the distribution is quite evident and persists up to 1.6 ps due to the relative inefficiency of the e-e scattering at this low free-carrier density. The kink in the curve at about 40 meV is the second subband energy.

In Fig. 7(b) we show the relative rates of e-e and electron-phonon scattering, calculated from the number of scattering events divided by the total number of particles over each time step. Phonon emission is the dominant scattering mechanism until the distribution has cooled sufficiently (1.6 ps) that e-e scattering is more important. Phonon absorption becomes increasingly important due to buildup of nonequilibrium phonons. As shown in Fig. 7(b), the rates of emission and absorption approach one another, resulting in a reduction of the net energy-loss rate.

At an injection density of 5×10^{11} cm^{-2} shown in Fig. 8(a), e-e scattering is more effective than the phonon emission, and the features of the cascade are washed out almost resulting in a thermalized (Maxwellian) type of distribution immediately after the pulse is over. The rate of e-e scattering is now greater due to the increased density of the injected carriers as shown in Fig. 8(b). Here e-e scattering exceeds the phonon emission rate after only 0.5 ps. Phonon absorption due to nonequilibrium phonons becomes important at shorter times due to the higher injected carrier density which generates a greater number of hot phonons.

In the simplified model for screening used here, the screening constant does not depend directly on density which is characteristic of low-temperature screening in a purely two-dimensional system. Thus, the scattering

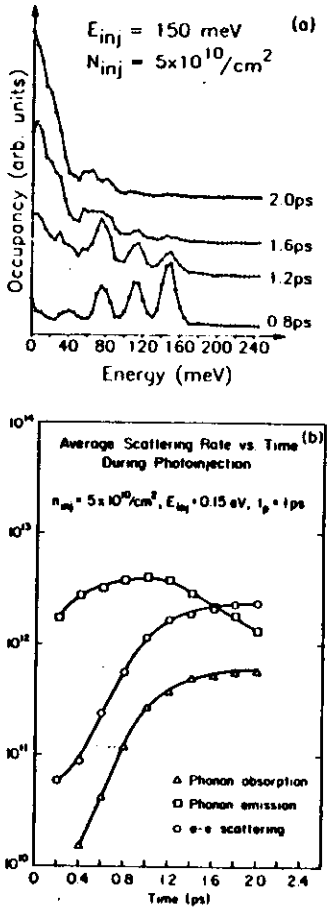

FIG. 7. (a) Electron occupancy as a function of energy for various times after laser excitation and an injection density of 5×10^{10} cm^{-2} at an energy 0.15-eV above the conduction-band edge. (b) Average total scattering rate per electron as a function of time for POP emission (□), absorption (△), and electron-electron (○) scattering.

rate (2.21) is directly proportional to the electron density resulting in the transition from cascadelike to thermalized behavior in the 1×10^{11} cm^{-2} range of carrier densities. If a more complete model for the screening is used, this simple picture will no longer hold as the screening constant depends on density, particularly at high temperatures. At high temperatures, q_0 is directly proportional to density for a 2D system,[27] and therefore e-e scattering may be important at lower densities as well.

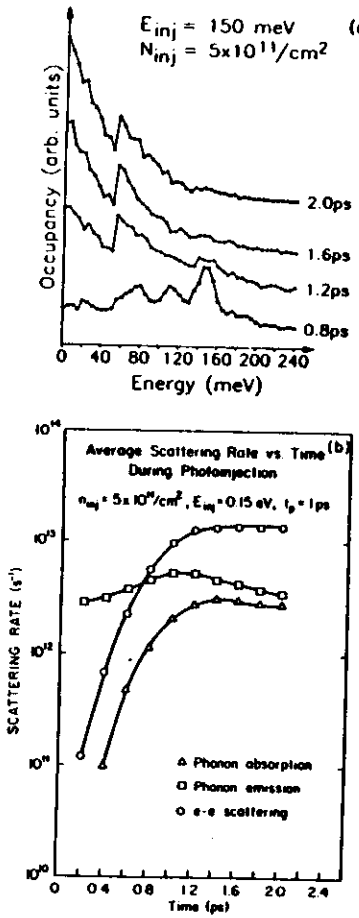

FIG. 8. Electron occupancy as a function of energy for various times after laser excitation and an injection density of 5×10^{11} cm^{-2} at an energy of 0.15 eV above the conduction-band edge. (b) Average total scattering rate per electron as a function of time for POP emission (□), absorption (△), and electron-electron (○) scattering.

However, the effect of reducing q_0 is to increase small-angle scattering which is ineffective in exchanging energy between particles,[24] and thus the density dependence may be qualitatively the same as we have presented here. The effect of temperature-dependent screening on carrier relaxation in 2D systems is discussed elsewhere.[28]

Due to the intersubband energy exchange arising from e-e scattering, redistribution of the carrier kinetic energy occurs and the subband energies tend to equilibrate. This effect is evidenced in Fig. 9 where we plot the carrier temperature (the average kinetic energy) in the lowest and first excited subband as a function of time during laser excitation. In this simulation, we start with a background density of 2.5×10 cm^{-2} carriers at 5 K in the lowest subband and then inject carriers at an energy of 0.25 eV above the lowest subband energy as discussed above. We inject a total of 5×10^{11} cm^{-2} carriers into the band using a 0.6-ps pulse which is centered at $t=1$ ps in Fig. 9. The injected carriers interact with the cold electrons through e-e scattering, transferring energy to them and losing energy in the process. As seen in Fig. 9, the electrons in both subbands rapidly reach the same average energy primarily through e-e scattering. As shown by the dotted curve of Fig. 9, when e-e scattering is absent, the electron temperatures remain quite different after the pulse is over. In Fig. 10, we plot the fractional occupancy of the lowest subband as a function of time with and without e-e scattering which shows little difference due to the relative weakness of intersubband e-e scattering in the present formalism.

The fraction of carriers which transfer to the L valley does depend on e-e scattering, especially at injection energies close to the L-valley energy. This is also shown in Fig. 10 on the left-hand side. More carriers reside in the upper valley at times after the pulse due to spreading of the injected distribution to higher energies before relax-

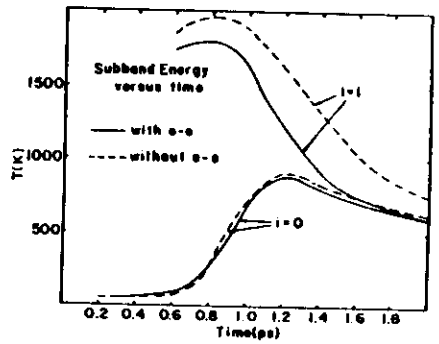

FIG. 9. Average kinetic energy with (solid line) and without (dashed line) e-e interaction in the ground ($i=0$) and first-excited ($i=1$) subbands during a 0.6-ps laser pulse which peaks at 1 ps. A background density of 2.5×10^{11} cm^{-2} is assumed with 5×10^{11} cm^{-2} carriers injected at an energy of 0.25 eV.

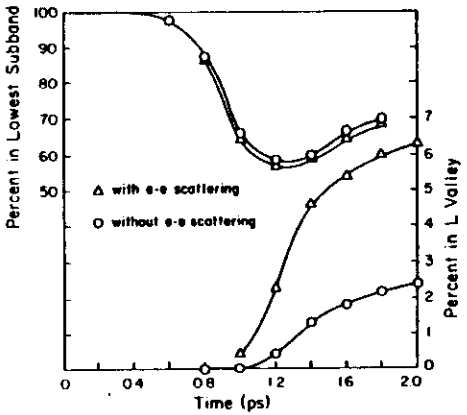

FIG. 10. Occupancy of the ground subband (top curves) with (Δ) and without (O) *e-e* scattering as a function of time for the same parameters as Fig. 9. Also shown is the occupancy of the *L* valley (bottom curves) with (Δ) and without (O) *e-e* scattering.

ing, allowing more carriers to transfer than in the case where this mechanism is absent. This fact accounts for the overall lower energy in Fig. 9 of electrons cooling subject to *e-e* scattering. The energy is eventually fed back into the electron system at longer times due to retransfer back from the *L* valley.

IV. CONCLUSIONS AND FUTURE WORK

We have presented a model for *e-e* scattering in a QW system using an ensemble Monte Carlo simulation. This model is capable of describing the carrier dynamics at low temperature through the inclusion of degeneracy and *e-e* scattering, which allows the equilibrium distribution at low temperature to achieve a Fermi-Dirac distribution in the simulation. With an applied electric field, *e-e* scattering is found to be effective in the 2D QW system in removing the kink in the distribution associated with phonon emission. Comparison of the calculated steady-state distribution function for various applied electric fields with photoluminescence results[33] show agreement in the gross features, but give consistently smaller electron temperatures as derived from the high-energy tail of the distribution.

We show that the shape of the distribution function is controlled by *e-e* scattering during and after laser excitation. For low carrier densities, *e-e* scattering is weak and electrons relax their energy via a cascade of successive optical-phonon emissions. For higher carrier densities, *e-e* scattering is more effective in setting up a heated Maxwellian distribution which absorbs the energy of the injected electrons before they can emit an optical phonon, thus suppressing the cascade. Our results show that thermalization of the carrier energy between subbands occurs quite rapidly through *e-e* scattering shortly after the end of the laser pulse. The exact scattering rate due to *e-e* scattering depends strongly on screening which is formally difficult in the multisubband system. We have used a low-temperature screening constant for the present work which overestimates the screening, and thus *e-e* scattering may be important at low electron densities as well. In future investigations, we will include heating effects on the 2D screening which our preliminary results show enhances the rate of *e-e* scattering during laser excitation.

ACKNOWLEDGMENTS

The authors would like to express their gratitude to R. Brunetti, C. Jacoboni, P. Kocevar, and J. Shah for many useful discussions related to this work. We would also like to acknowledge financial support from the Alexander von Humboldt Foundation in this research.

[1]J. L. Oudar, D. Hulin, A. Migus, and A. Antonetti, Phys. Rev. Lett. 55, 2074 (1985).
[2]W. H. Knox, C. Hirlimann, D. A. B. Miller, J. Shah, D. S. Chemla, and C. V. Shank, Phys. Rev. Lett. 56, 1191 (1986).
[3]J. F. Ryan, R. A. Taylor, A. J. Turberfield, A. Maciel, J. M. Worlock, A. C. Gossard, and W. Wiegmann, Phys. Rev. Lett. 53, 1841 (1984).
[4]J. Shah, A. Pinczuk, A. C. Gossard, and W. Wiegmann, Phys. Rev. Lett. 54, 2045 (1985).
[5]C. H. Yang, J. M. Carlson-Swindle, S. A. Lyon, and J. M. Worlock, Phys. Rev. Lett. 55, 2359 (1985).
[6]D. N. Mirlin, I. Ya Karlik, L. P. Nikitin, I. I. Reshina, and V. F. Sapega, Solid State Commun. 37, 757 (1980).
[7]S. M. Goodnick and P. Lugli, in *Proceedings of the 18th International Conference on the Physics of Semiconductors*, edited by O. Engstrom (World-Scientific, Singapore, 1987), pp. 1334–1338.
[8]S. M. Goodnick and P. Lugli, in *High-Speed Electronics*, edited by B. Kallack and H. Beneking (Springer-Verlag, Berlin, 1986).
[9]M. Tomizawa, K. Yokoyama, and A. Yoshii, IEEE Electron Dev. Lett. EDL-5, 464 (1984).
[10]K. Yokoyama and K. Hess, Phys. Rev. B 33, 5595 (1986).
[11]M. Al-Mudares and B. K. Ridley, Physica 134B, 526 (1985).
[12]P. Lugli, S. M. Goodnick, and F. Koch, Superlatt. Microstruct. 2, 335 (1986).
[13]T. Ando, A. B. Fowler, and F. Stern, Rev. Mod. Phys. 54, 437 (1982).
[14]P. J. Price, Ann. Phys. (N.Y.) 133, 217 (1981).
[15]F. A. Riddoch and B. K. Ridley, J. Phys. C 16, 6971 (1983).
[16]F. A. Riddoch and B. K. Ridley, Physica 134B, 342 (1985).
[17]C. H. Yang and S. A. Lyon, Physica 134B, 309 (1985).
[18]S. Das Sarma, W. Y. Lai, and A. Kobayashi, in *Proceedings of the 18th International Conference on the Physics of Semiconductors*, Ref. 7, pp. 651–654.
[19]P. J. Price, Phys. Rev. B 30, 2234 (1984).
[20]D. K. Ferry, Surf. Sci. 57, 218 (1976).
[21]E. Abrahams, Phys. Rev. 95, 839 (1954).
[22]J. M. Ziman, *Electrons and Phonons* (Oxford University Press, London, 1960), pp. 170–172.
[23]N. Takenaka, M. Inoue, and Y. Inuishi, J. Phys. Soc. Jpn. 47, 861 (1979).
[24]C. J. Hearn, in *The Physics of Nonlinear Transport in Semiconductors*, edited by D. K. Ferry, J. R. Barker, and C. Jacoboni (Plenum, New York, 1980), pp. 153–166.
[25]E. D. Siggia and P. C. Kwok, Phys. Rev. B 2, 1024 (1970).
[26]F. Stern, Phys. Rev. Lett. 18, 5009 (1978).
[27]A. L. Fetter, Phys. Rev. B 10, 3739 (1974).
[28]S. M. Goodnick and P. Lugli, Appl. Phys. Lett. 51, 584 (1987).
[29]C. Jacoboni and L. Reggiani, Rev. Mod. Phys. 65, 645 (1983).
[30]S. Bosi and C. Jacoboni, J. Phys. C 9, 315 (1976).
[31]P. Lugli and D. K. Ferry, IEEE Trans. Electron Dev. ED-32, 2431 (1985).
[32]R. Brunetti, C. Jacoboni, A. Matulionis, and V. Dienys, Physica 134B, 369 (1985).
[33]J. Shah, A. Pinczuk, H. L. Störmer, A. C. Gossard, and W. Wiegmann, Appl. Phys. Lett. 44, 322 (1984).
[34]S. A. Lyon, J. Lumin. 35, 121 (1986).
[35]P. Kocevar (private communication).

MONTE CARLO SIMULATION OF INTERSUBBAND RELAXATION IN SEMICONDUCTOR QUANTUM WELLS

S.M. Goodnick
Center for Advanced Materials Research, Oregon State University
Corvallis, Oregon 97331

P. Lugli
Dipartimento di Ingegneria Mecanica, II Universitá di Roma
Via O. Raimondo, 00173 Roma, Italy

(Received 12 August 1988)

We have used an ensemble Monte Carlo simulation of semiconductor quantum wells to simulate recent time resolved optical experiments of intersubband relaxation. In the present work we model a single quantum well electron system with the inclusion of intra- and intersubband carrier-carrier scattering and nonequilibrium polar optical phonons. Simulated results with and without these basic mechanisms show that the experimentally measured long time constant pile-up of carriers in upper subbands in wide quantum wells appears to be associated with the thermal tail of the total carrier distribution function which remains hot for long times after the pump pulse due to hot phonon effects.

Time resolved optical studies of bulk GaAs and GaAs/AlGaAs quantum wells have provided a wealth of information on the dynamics of hot carrier relaxation in semiconductors. Such experiments have been used to illuminate effects such as nonequilibrium phonons[1,2] and electron-electron relaxation in quantum well systems.[3] Recently, time resolved techniques have been employed to study the relaxation of carriers through intersubband scattering.[4,5] In such experiments, a short time duration pump pulse is used to generate carriers in upper subbands of a quantum well system, and a subsequent optical probe is used to study the relative population of carriers in the upper subbands as a function of time. Oberli et al.[4] used intersubband Raman scattering to look at the relaxation time for 116Å and 215Å wells using a pump pulse which generates carriers in the first and second subbands simultaneously at energies just above the second subband edge. In the narrow well, the observed depopulation of the second subband was extremely rapid, less than the time resolution of the experiment. Such a rapid depopulation is expected since the intersubband scattering rate due to polar optical phonons (POP) is relatively quick, on the order of a picosecond.[6] For the wider well, the separation between the first and second subbands was reported to be 27meV which is less than the optical phonon energy (35meV). Thus, carriers at the bottom of the second subband are forbidden from making transitions via the POP mechanism, leading to the possibility of a 'bottleneck' in the depopulation of the upper level.[4] Long time constants for the carrier population in the second subband were indeed observed, on the order of several hundred picoseconds. Seilmeier et al.[5] used time resolved infrared absorption to study intersubband relaxation in 50Å wells where the intersubband separation is large. In contrast to the results of Oberli et al., they observed a relatively slow relaxation rate in their studies with time constants of 11-14ps, much longer than the expected rate due to intersubband POP scattering rate.

In order to more fully interpret these experiments, we have performed Monte Carlo simulations of the above experiments. Here we model only the electron system and defer study of electron-hole interactions to future work.[10] The model we use is discussed in detail elsewhere[7-9] where the main mechanisms of concern in the present paper are the inclusion of inter- and intrasubband e-e scattering, and bulk-like POP scattering including hot phonon effects. A simple square well potential is assumed for subband wavefunctions and energies.

For e-e scattering, a static screened interaction is employed using the long wavelength limit of the RPA dielectric matrix which changes continually during the simulation through changes in the carrier distribution function.[8] For intersubband e-e scattering, we use the same dielectric matrix as for intra-band scattering which overestimates screening. Thus the rate of intersubband e-e scattering is expected to be even greater than modeled here.

For nonequilibrium phonons in the Monte Carlo simulation,[7] the population of phonons with momentum parallel to the well is calculated from a detailed balance of emission and absorption events during the simulation as well as decay due to a phenomenological time constant taken as 7ps from Raman experiments.[1] The phonon wavevector normal to the well is constrained to wavevectors less

0749-6036/89/040561+03 $02.00/0

than the inverse width of the quantum well system which corresponds to the width of the phonon 'wave packet' in momentum space.[11]

To simulate optical excitation, we add particles to the simulation centered around the excess electron energy in the conduction band according to the temporal distribution of the experimental laser pulse.[9] Degeneracy of the final states is also included through a rejection technique.[9]

In the present paper, we report on simulations of carrier relaxation corresponding to the experiments of Oberli et al.[4] Here we assume a total carrier density of $4\times10^{11}/cm^2$ after injection at a lattice temperature of 5K. A pulse duration of 1ps is assumed in all the simulated results with the pulse peaking 1ps into the simulation. The injection energies are chosen so that carriers are excited below the optical phonon energy in the upper subband in accordance with the experimental studies.[12] Well widths of 120Å and 230Å were used in our calculations in order to match the experimental intersubband separations.

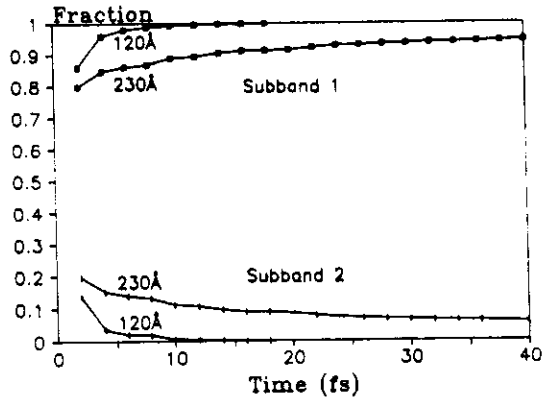

Figure 1. Fraction of the total carrier population residing in subbands 1 and 2 for two different well widths.

Figure 1 shows the comparison of the relative subband populations for both the 120Å and the 230Å well. The result here is similar to that found by Oberli et al., at least for the time scale that can reasonably be modeled using the Monte Carlo method. The population in the upper subband of the 120Å well decays quite rapidly and is completely empty after about 10fs. The 230Å well on the other hand maintains a sizable population in the upper subband even after 40ps.

The question is whether a bottleneck occurs in the intersubband transfer due to the suppression of POP scattering. To study this, we look at the total distribution of the electrons in the 230Å well at various times after photoexcitation into the second subband as shown in Fig. 2. The kink in the distribution function at 27meV corresponds to the position of the second subband for this particular well. If there is a true bottleneck occurring, then the occupancy of the second

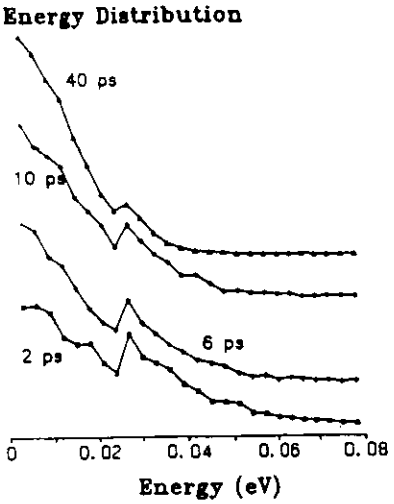

Figure 2. Total energy distribution function for carrier relaxation in a 230Å well at various times after the peak of the pump pulse at t=1ps.

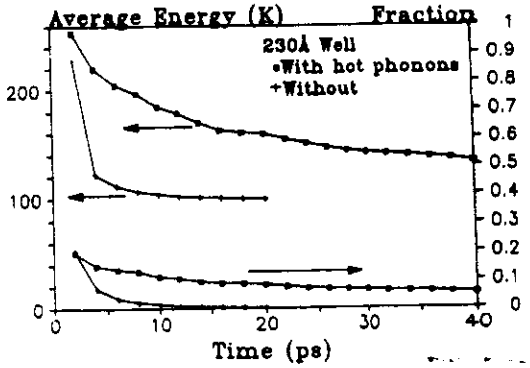

Figure 3. Average energy and fraction of carrier residing in the second subband for the 230Å well with and without the effect of hot phonons.

subband should be greater than that of the first subband. However, as seen from Fig. 2, the relative occupancy of the first and second subbands are virtually the same at all times. The occupancy of the second subband appears to be due to the thermal tail of the distribution function from the first subband.

To understand the origin of this long tail we selectively 'turn off' the effect of nonequilibrium phonons by forcing them to remain in equilibrium, and compare to the previous result. The comparison is shown in Fig. 3. We first note that the average energy of the carriers decreases rapidly and quickly reaches its equilibrium value of half the Fermi energy at 5K. As is well known, the effect of nonequilibrium phonons is to slow down the dissipation of energy by keeping the excess electron energy within the coupled

electron-phonon system through increased absorption.[13] This effect is reflected in the relative occupancy of the second subband. As shown in Fig. 3, the occupancy of the second subband decays rapidly without the presence of hot phonons to maintain a thermal tail above the second subband energy.

There are several competing effects which tend to prevent a bottleneck from forming due to polar optical phonon suppression. One is inelastic e-e scattering which allows some of the electrons to be promoted above the effective threshold for scattering from subband 2 to subband 1. Another factor is e-e intersubband scattering which is always present. In the case of the 230Å well, the total number of scattering events due to intersubband e-e scattering was about a tenth that due to POP intersubband scattering. Thus the contribution is relatively weak, although as mentioned previously, a more complete screening model for this mechanism could result in an increased intersubband scattering rate. Finally, in order for electrons to scatter from the lowest subband to the second subband via phonon emission, they have to have an energy at least one phonon energy (35meV) above the bottom of the second subband. Thus there is a barrier to repopulation of the second subband which opposes the formation of a bottleneck.

We have additionally run simulations of the experiments of Seilmeier et al.[5] and find no decreased intersubband relaxation rate as was measured experimentally. However, in their experiments, the second subband in 50Å quantum wells is close to the top of the barrier, so real space transfer effects could play an important role which was not considered here.

Acknowledgement - The authors would like to thank D. Oberli and J. Shah for useful discussions related to this work. This work was partially supported by the Office of Naval Research.

References:

1) N. von der Linde, J. Kuhl, and H. Klingenburg, Phys. Rev. Lett., 44, 1505 (1980)
2) J. Shah, A. Pinczuk, A.C. Gossard, and W. Wiegmann, Phys. Rev. Lett. 54, 2045 (1985)
3) W.H. Knox, C. Hirlimann, D.A.B. Miller, J. Shah, D.S. Chemla, and C.V. Shank, Phys. Rev. Lett. 56, 1191 (1986)
4) D.Y. Oberli, D.R. wake, M.V. Klein, J. Klem, T. Henderson, and H. Morkoc, Phys. Rev. Lett. 59, 696 (1
5) A. Seilmeier, H.J. Huebner, G. Abstreiter, G. Weimann, and W. Schlapp, Phys. Rev. Lett. 59, 1345 (1987)
6) F.A. Riddoch and B.K. Ridley, J. Phys. C 16, 6971 (1983)
7) P. Lugli and S.M. Goodnick, Phys. Rev. Lett. 59, 716 (1987)
8) S.M. Goodnick and P. Lugli, Appl. Phys. Lett. 51, 584 (1987)
9) S.M. Goodnick and P. Lugli, Phys. Rev. B37, 2578 (1988)
10) S.M. Goodnick and P. Lugli, Submitted for publication
11) W. Cai, M.C. Marchetti, and M. Lax, Phys. Rev. B37, 2636 (1988)
12) D. Oberli, private communication
13) W. Poetz and P. Kocevar, Phys. Rev. B 28, 7040 (1983)

Superlattices and Microstructures, Vol. 2, No. 4, 1986

MONTE CARLO STUDY OF HOT ELECTRONS IN QUANTUM WELLS

P. Lugli
Dipartimento di Fisica, Università di Modena, Via Campi 213/A, 41100 Modena, Italy

S. Goodnick and F. Koch
Physik-Department E 16, Technische Universität München
D-8046 Garching, Fed. Rep. of Germany

(Received: 18 August 1986)

We have performed an ensemble Monte Carlo calculation of the high field response at 77 K of two different two-dimensional systems, one a modulation doped (MD) single square well of GaAs/AlGaAs and the other a δ-doping layer formed by a sheet of donor impurities embedded in bulk GaAs. Results of this calculation show a reduced low field mobility and a decrease in the transient overshoot velocity in the δ-doping versus MD system due to the effect of impurity scattering. At high fields, however, the steady state saturated drift velocities appear to be similar in the two systems. Because of the higher carrier density, the performance of short-channel devices based on the δ-layer will be advantageous where high output currents are necessary.

In layered structures grown by molecular beam epitaxy (MBE), one is free to choose the position of the donor impurities, and thus various schemes are available in order to create a conducting layer for use as a channel in device applications. In modulation doped (MD) structures the dopants are spatially separated from the two-dimensional electron gas (2DEG) which results in very high low field mobilities for this system. The high electron mobility transistor (HEMT) is a device based on this doping scheme. Another type of doping, the so-called δ-function doping, places the impurities at the center of the potential well, thus localizing the charge carriers in the vicinity of the donors. Although this is a disadvantage in terms of achieving high mobilities, very high carrier concentrations ($10^{13}/cm^2$) are possible. MD structures typically have concentrations of order $10^{12}/cm^2$. Initial studies of δ-doping layers have shown the existence of a multi-subband 2DEG[1]. Field-effect-transistors have been fabricated utilizing such layers[2]. Since the carrier concentration is high in the δ-layer, transistors based on this system may be attractive for use in high power applications. Also, since the processing for such layers is the same as that for HEMT devices, it is feasible to consider hybrid circuits which combine devices of both types on the same chip, taking advantage of the relative virtues of each design, depending on the application.

Because of the possibility of integrated circuits based on such 2DEG systems, it is of interest to understand their high field performance and pico-second response, especially when submicron channel dimensions are considered. Here we report on the results of a Monte Carlo simulation of the hot electron behaviour. We compare the non-equilibrium response of a δ-doping layer with that of a modulation doped quantum well of GaAs-AlGaAs. We consider the response for a lattice temperature of 77 K which corresponds to a typical operating point for HEMT devices. We have also considered densities typical for the reported experimental results in both cases. For the quantum well, we assume a density of $5x10^{11}/cm^2$ carriers in the well coming from an equal number of ionized donors located in the AlGaAs layer. For the δ-doping layer, a free carrier density of $5x10^{12}/cm^2$ was used in the calculations. This value is close to the density measured in δ-doped field effect transistors[2].

Fig.1 shows the model potential considered for each case. For the square well, we calculate the eigenvalues and wavefunctions corresponding to the one-dimensional potential shown in the upper part of this figure with a GaAs well width of 150 Å and a barrier height of 0.28 eV between the GaAs and the AlGaAs. The central and satellite L-valleys are treated as parabolic. Details of the construction of the δ-layer subbands are given elsewhere[1,2]. The basic structure consists of a sheet of positive charge embedded in GaAs. This charge creates a potential well in which an equal number of free electrons is localized. The subband energies and wavefunctions are calculated for this system using the Hartree approximation in which the one-dimensional Schrödinger's equation is solved self-consistently with Poisson's equation for the electron charge distribution. The

0749-6036/86/040335+04 $02.00/0

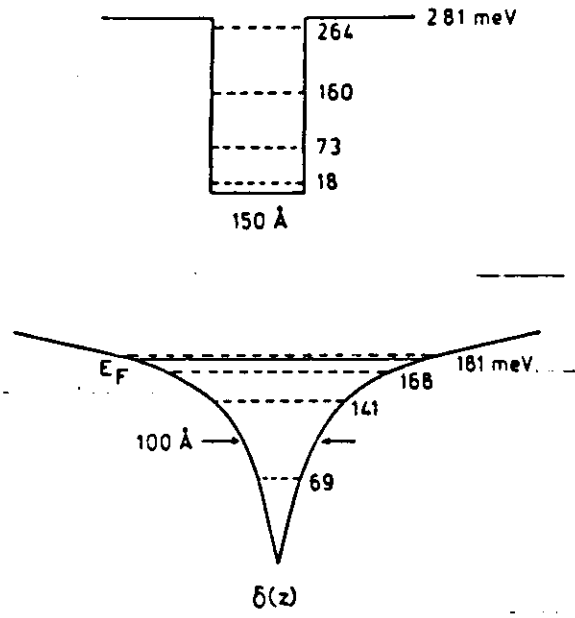

Fig. 1

subband energy levels and potential obtained using a density of $5 \times 10^{12}/cm^2$ are shown in Fig.1.

In the Monte Carlo calculation, we simulate the electron motion parallel to the well including polar optical phonon (POP)-, impurity- and non-equivalent intervalley-scattering, for both intra- and intersubband events. POP scattering is calculated assuming that the phonon modes are bulk-like interacting with quantized electrons via the Fröhlich Hamiltonian. Since self-consistent wavefunctions are used, all matrix elements are calculated numerically. The calculated POP scattering rates are not found to vary considerably between the quantum well and the δ-layer as the scattering rate depends primarily on the density of states and not details of the wavefunctions.

In this initial work, we treat impurity scattering as arising from a sheet of charge, both for the square well and for the δ-doping layer. For the square well, this sheet is embedded in the AlGaAs layer, here chosen as 75 Å from the interface between the GaAs and the AlGaAs, in order to simulate the effect of modulation doping. For the δ-layer, impurity scattering is due to the sheet of ionized donors at the center of the well. The interaction between the electrons and the impurities is taken as a screened Coulomb potential with a fixed screening constant given by the long wavelength limit of the 2D RPA dielectric function for a single subband. Because of the spatial separation of the 2D layer from the impurities in the case of the square well, the scattering rate as a function of energy for the same density of scatterers decays much more rapidly than the rate for the δ-layer. Since the density of impurities is also much higher in the δ-layer, the effect of impurity scattering is much stronger in this system.

With only the central valley present in the simulation, POP scattering alone is not sufficient to prevent a runaway in the electron energy for high electric fields (5 kV/cm). Thus we also include the 4-fold degenerate L-valleys in the simulation, also quantized as in the case of the central valley, but with a different effective mass. The scattering rate is calculated via the optical deformation potential between initial and final quantized states with the appropriate optical phonon linking the two valleys.

Because of the high carrier densities and low temperatures investigated here, the effect of degeneracy has to be included in the scattering rate. Here we use the method employed in bulk Monte Carlo studies[3] in which the k-space distribution is calculated at every time step in the simulation from the electron ensemble. In the 2D system, a separate distribution is kept for each subband, normalized to the effective area of the simulation (the number of electrons in the simulation divided by the density). After selecting the final state for a particular scattering event, a rejection technique is used to account for the probability that the final state is occupied.

In the ensemble Monte Carlo calculation we typically follow 2000 electrons during the simulation which are assumed to start at $t = 0$ with a Fermi-Dirac distribution in equilibrium with the lattice. In the present work, the subband energies are held constant, even though carrier heating and redistribution will change the well shape. However, the results of similar calculations which include dynamic effects in the subband energies do not seem to differ too dramatically from the case in which the energies are held constant[4].

For the δ-layer, no substantial electron heating was observed to occur up to 3 kV/cm. Due to the high sheet charge concentration, the system is extremely degenerate, and the scattering cross-section for POP scattering is strongly reduced with respect to the non-degenerate situation. In Fig.2 we plot the steady state energy distribution of central valley carriers in the δ-layer for two different fields. At 1 kV/cm (quasi-ohmic regime), the distribution appears Fermi-like due to the inclusion of degeneracy. Here carriers occupy primarily the first two subbands, each characterized by a well-defined electron temperature. At 5 kV/cm electrons are heated up by the field and 33% of them have transferred to the L-valleys. The electron heating in the Γ-valley is clearly shown by the slope of the distribution function. The subband structure of the δ-layer is also evident in this figure from the discontinuities in the distribution function (the arrows indicate the energies above the lowest ground subband).

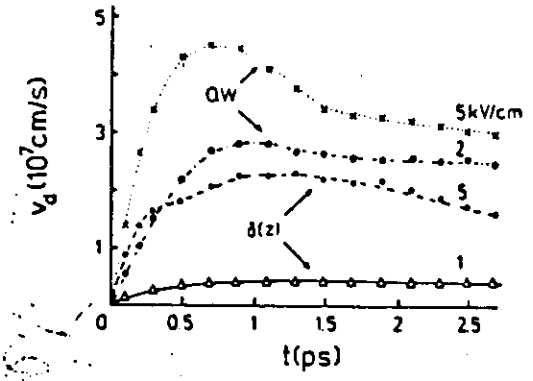

Fig. 2

The possibility for ballistic transport in 2D systems can be analysed by studying the time response of the electrons to a step-like uniform electric field. Fig.3 shows the drift velocity as a function of time after application of an electric field at 77 K for both the quantum well and the δ-layer. The quantum well exhibits a pronounced overshoot at 5 kV/cm. Here electrons accelerate quasi-ballistically until they gain enough energy to transfer into the upper valley where the higher effective mass of the L-valley causes a reduction of the carrier drift velocity. The steady state situation (with about 30% of the electrons occupying the quantized subbands of the satellite valley) is reached after about 3 ps. The average distance travelled by the ballistic electrons before transferring is about 0.35 μm. For this reason, heterostructure devices with submicron dimensions should exhibit improved performance over that of longer channel devices. As seen in Fig. 3 for the quantum well, as the electric field is lowered, the transfer to the L-valley is strongly reduced and the steady state condition is approached without any significant overshoot.

The situation is somewhat different when the δ-layer is considered. Due to the high impurity concentration, the momentum losses associated with this scattering mechanism force the mobility to be low with respect to the MD system. At 5 kV/cm, a slight overshoot is detected, but the peak value is much lower than for the quantum well structure. In the steady state, for a field of 5 kV/cm, the ratio of impurity scattering to POP scattering is found to be 28:1 for δ-layer in comparison to a factor of only 1.5:1 for the MD quantum well.

The drift velocity as a function of electric field is shown in Fig.4. The calculated steady state curve for bulk GaAs[5] with an impurity concentration of $10^{17}/cm^3$ is also shown for comparison. The low field mobility (taken from the slope of the velocity field curve at zero field) for the MD quantum well is found to be about 23000 $cm^2/Vsec$.

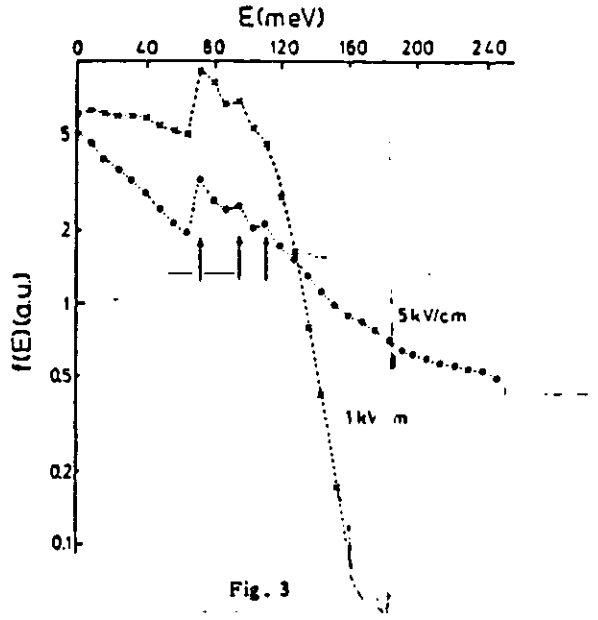

Fig. 3

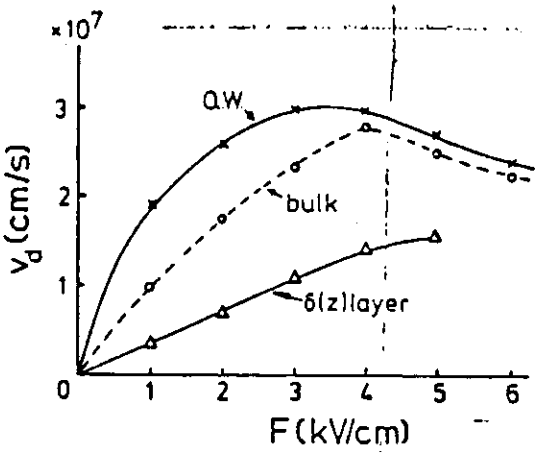

Fig. 4

The δ-layer has a much smaller low-field mobility of about 3400 $cm^2/Vsec$ as evidenced by the smaller slope of the velocity-field curve. This value is an average over the various filled subbands of the layer. Experimentally an average value of about 2000 $cm^2/Vsec$ at 77 K has been found[6]. As shown in Fig.4, the modulation doped structure has a higher velocity than the bulk at low and intermediate field strengths, but decreases to the same value asymptotically at fields above 5 kV/cm, showing a region of negative differential mobility. At these high fields, electrons are

heated well above the lattice temperature and the efficiency of impurity scattering is greatly reduced. Thus, the advantage of including a spatial separation between the donors and the charge carriers tends to disappear. At high fields, the δ-layer approaches the same bulk saturation velocity as the field is increased, but without showing negative differential mobility. Thus, the saturated drift velocity in these systems will be relatively unaffected by the doping scheme used.

In conclusion, we have studied the transient and steady state behaviour of a MO quantum well structure and a δ-doping layer. Due to the much higher density of impurities located in the center of the well, the low field response of the δ-layer is poorer than that of a modulation doped structure. At high fields, however, both systems approach the same asymptotic saturation velocity. Thus, in short channel devices where the saturated velocity plays a major role in the device speed, it is possible that the δ-layer could perform favorably, especially considering the higher channel densities possible with this type of doping.

Acknowledgement - The authors thank A. Zrenner and M. Zachau for useful discussions. This work was partially supported by the Alexander von Humboldt foundation and the ERO.

References:

1) A. Zrenner, H. Reisinger, F. Koch, K. Ploo and J.C. Maan, Physical Review B 33, 5607 (1986)
2) E.F. Schubert and K. Ploog, Japanese Journal of Applied Physics 24, 1608 (1985)
3) P. Lugli and D.K. Ferry, IEEE Transactions on Electron Devices, ED-32, 2431 (1985)
4) K. Yokoyama and K. Hess, Journal of Applied Physics 59, 3798 (1986)
5) J.G. Ruch and W. Fawcett, Journal of Applied Physics 41, 3843 (1970)
6) A. Zrenner, private communication

943-11

Monte Carlo simulation of sub-picosecond phenomena in semiconductor quantum wells and superlattices

Stephen M. Goodnick

Oregon State University, Center for Advanced Materials Research
Corvallis, Oregon 97331

and

Paolo Lugli*
Universitá di Modena
Dipartimento di Fisica
Via Campi 213/A, 41100 Modena, Italy

ABSTRACT

We have modeled ultra-fast processes occurring during photoexcitation in AlGaAs/GaAs quantum wells using an ensemble Monte Carlo simulation. This simulation models the dynamics of quasi-two-dimensional electrons and holes confined within a single quantum well including the effects polar optical and transverse optical phonons, intervalley scattering, ionized impurities, and intercarrier scattering. The effect of nonequilibrium phonons and degeneracy are also included. We have used our simulation to compare to time resolved photoluminescence and transmission experiments in semiconductor quantum wells. For the latter experiments (W.H. Knox et al., Phys. Rev. Lett. 56, 1191 (1986)) performed at low excitation energies in the band, the results of our simulation show that electron-electron scattering is the dominant mechanism in accounting for the experimentally observed relaxation. While the electrons relax to form a thermalized distribution over 200 fs, the heavy holes generated at the same time relax within 50 fs, and the corresponding differential transmission spectrum is primarily determined by electron relaxation in the conduction band. Thermalization of the electrons with the cooler holes occurs over a longer time scale of 1 ps via inelastic intercarrier scattering.

1. INTRODUCTION

Femtosecond laser excitation in semiconductor quantum wells has provided a unique probe of nonequilibrium carrier relaxation with picosecond and subpicosecond time resolution.[1-5] Such experiments are usually pump and probe studies in which an ultra-fast laser pulse is used to generate electron-hole pairs which are optically probed at time delays after the initial pulse. Such optical probes include photoluminescence,[1] Raman scattering,[2] and absorption bleaching experiments.[3-5] In the experiments of Knox et al.,[4,5] AlGaAs-GaAs multiple quantum wells were studied using a pump probe at 1.509 eV which generates electrons approximately 20 meV above the conduction band edge. Since this energy is below the energy of the longitudinal optical phonons (36 meV), it was argued that the carriers must relax through intercarrier interactions rather than through phonon emission. In undoped quantum wells with low intensity excitation, the differential transmission spectrum measured at various time intervals before and after the pulse was observed to evolve from an athermal distribution centered around the pump energy (hole burning) to a thermalized (i.e., Maxwellian) distribution over a time scale of 200 fs. For n-doped samples under high density injection, the thermalization time was much shorter, less than 50 fs.[5] This behavior was explained using a simple relaxation time model assuming electron-electron scattering. Monte Carlo simulation of these experiments[6,7] also showed that the experimentally observed relaxation could be accounted for by

*Permanent address: II Universitá di Roma, Dipartimento di Ingegneria Meccanica, Via O. Raimondo, 00173 Roma, Italy.

943-11

electron-electron scattering. Although e-e scattering does not change the average energy of the carriers since energy is conserved, it does allow electrons to scatter to different energy shells, and hence band filling is simply a result of diffusion or spreading of the injected pulse in momentum space.

Although the experimental results seem to be adequately accounted for by e-e scattering, the actual situation is much more complicated due to the presence of equal numbers of holes generated at the same time as the electrons. In fact, the absorption coefficient (neglecting the excitonic part) depends not only on the electron distribution but on the hole distribution as well

$$\alpha(E_p)\alpha(1 - f_e - f_h), \tag{1}$$

where $\alpha(E_p)$ is the absorption coefficient at photon energy E_p, f_e is the electron distribution function and f_h is the hole distribution function. The differential transmission is therefore the sum

$$\Delta T/T_o = f_e + f_h . \tag{2}$$

which depends on the relaxation of both the electrons and the holes. The interpretation of the relaxation is also complicated because the electrons and the holes scatter inelastically exchanging kinetic energy between both systems of carriers. Thus, electron-hole scattering could also be responsible for the observed relaxation.

In the present article, we investigate the role that holes play in the interpretation of these bleaching experiments through Monte Carlo simulation of these experiments. We present a model for the coupled electron-hole system described in the following section. From the calculated results of this model, we show that the observed evolution of the differential transmission spectrum is indeed primarily due to relaxation of the electron distribution as the holes thermalize on a much shorter time scale. However, substantial heating of the hole distribution occurs in room temperature experiments due to the absorption of TO and LO phonons by the holes which are injected at an energy below the lattice temperature.

2. Monte Carlo Simulation

In a Monte Carlo simulation of transport in semiconductor materials, the motion in k-space of charge carriers (and other quasi-particles as well) is simulated as a function of time subject to external fields and the various collision processes present in the material.[8] Numerically, the free flights between scattering events are generated stochastically using the computer random number generator according to the scattering probabilities calculated using time dependent perturbation theory. In an ensemble Monte Carlo, the trajectories of many particles (which in general may interact) are modeled simultaneously so that macroscopic quantities such as drift velocity and mean energy are calculated as averages over the ensemble as a function of time. Thus the transient time evolution of a system of nonequilibrium carriers may be simulated with no assumptions made concerning the form of the distribution function, which makes the Monte Carlo method well suited to study ultra-fast phenomena such as the pump and probe experiments discussed earlier.

The basic model that we have employed to study carrier relaxation in quantum wells as been discussed in detail elsewhere.[9] Essentially we use a simplified model for the quantum well subband structure, that of a square well potential determined by the band offset between $Al_xGa_{1-x}As$-GaAs. Parabolic bands are assumed for both the electrons and the holes, so that for the hole subbands, two sets of subbands arise due to light and heavy holes. In reality, the subband structure in the valence band is much more complicated due to the admixture of light and heavy hole states caused by the well potential[10] which is beyond the scope of the present paper.

We include scattering due to longitudinal polar optical (LO) phonons for electrons and holes and transverse optical (TO) phonons for the holes only. In the former case, the Froehlich coupling describes the interaction between quasi-two-dimensional charge carriers and bulk-like phonons[9,11,12] for both intra- and intersubband scattering events. The TO phonon scattering rate is calculated using the deformation potential Ansatz which has been calculated by Ridley[11] for quasi-two-dimensional systems and generalized to include arbitrary shaped wells. The deformation potential constant for heavy holes was taken as $1x10^9$ eV/cm. For the LO phonons, we include the effect on the scattering rate of the nonequilibrium distribution of phonons which may be generated by the optically injected carriers.[13] This is accomplished by keeping a detailed balance of phonon emission and absorption processes and otherwise relaxing the phonon distribution via a phenomenological time constant. For the time scales considered in the present study, hot phonon effects do not play an important role. For the time scales and energies involved, acoustic mode and intervalley scattering are also negligible.

Intercarrier scattering is calculated in a similar manner to our previous calculation of e-e scattering in a multi-subband system[6,9] where we consider two particle interactions through a screened Coulomb potential with the reduced mass replacing the electron mass for electron-hole events. Off-diagonal screening in the matrix dielectric function of the electron-hole multisubband system is neglected and the long-wavelength Fermi-Thomas limit is assumed generalized for an arbitrary distribution function of carriers.[6] As in the case of e-e scattering alone, intrasubband transitions are much stronger than those associated with intersubband scattering due to the overlap integral of subband functions and the large q vectors involved in intersubband transitions. The intraband scattering includes scattering events in which the two particles are in different subbands (but remain in the same subband after the collision), and thus this type of interaction is effective in transferring energy

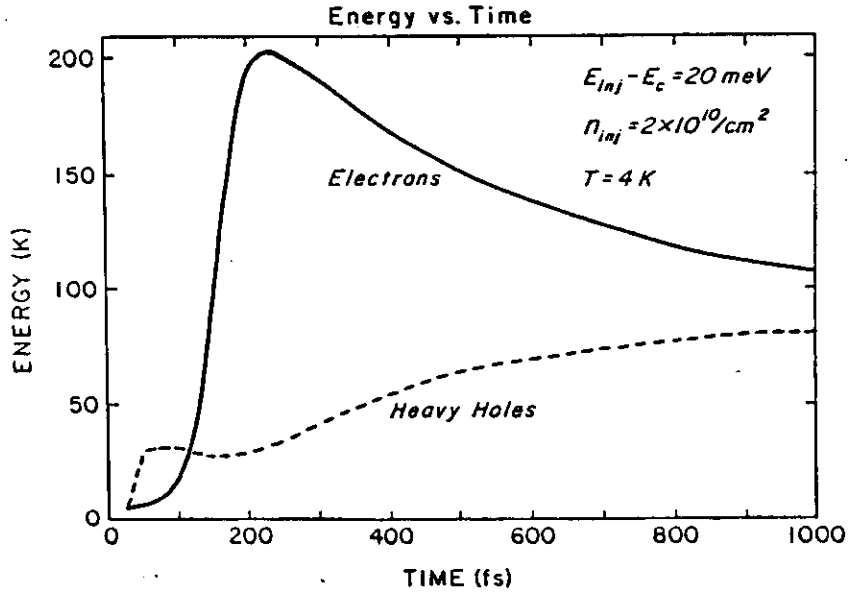

Figure 1. Energy versus time at 4.2 K for electron and holes during photoexcitation. The pulse is 100 fs wide and peaks at 200 fs.

943-11

between subbands and between the electron and hole systems which is important in ultra-fast relaxation experiments. For the low injection energies involved, light holes are not found to be present in substantial numbers, and thus we consider only the heavy holes in the following results.

In addition to the above, we include the effects of the Pauli exclusion principle on the scattering probability through a self scattering technique discussed elsewhere.[9] We neglect the contribution of the overlap integral of the Bloch states on the calculalated scattering rates[14] which to first order is unity for small angle scattering. This assumption is true for LO phonons and intercarrier scattering, but less so for TO phonon scattering which is isotropic.

3. SIMULATED RESULTS

To simulate the laser pulse, we introduce carriers around the injection energy at each time step of the simulation according to the time duration of the pulse.[9] For the experiments of Knox et al.,[4,5] the laser pulse duration was 100 fs with a spectral broadening of 20 meV. We simulate this spectral broadening by generating carriers in a Gaussian distribution centered at the pulse energy. To compare with the results of Knox et al.[4] for low injection densities, we use a well width of 95 Å and a background density of $2x10^9/cm^2$ electrons in the well corresponding to the residual impurities in the unintentionally doped MBE layers. The injected density of electron-hole pairs due to the pulse was estimated at $2x10^{10}/cm^2$ from the total absorbed power in these experiments.[4,5] For the simulated results, we used 20000 to 40000 particles and a 5 fs time step.

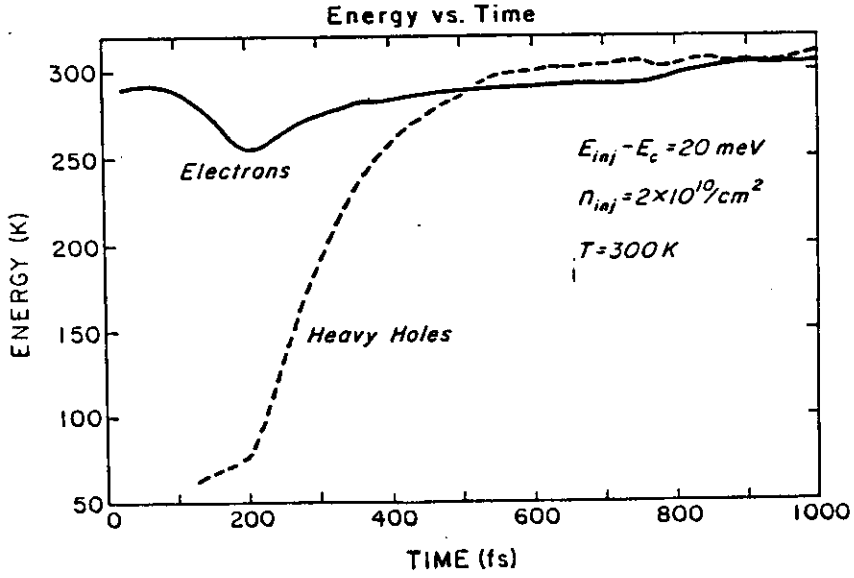

Figure 2. Energy versus time at 300 K for the same conditions as in Figure 1.

To illustrate the interaction of the electrons and holes during excitation, we show in Fig. 1 the average energy of the electrons and heavy holes as a function of time before and after excitation for carriers injected into system at 4.2 K. At this temperature, the contribution due to phonon absorption is negligible and the electrons are injected at a temperature greater than the lattice temperature. The maximum of the pulse occurs at t = 200 fs. The holes are observed to gain energy from the electron system which cools more rapidly than in the case in which the e-h interaction is shut off (dashed curved in Fig. 1).[6] Over the time scale of the plot, an equilibrium between the two systems is not reached, although they appear to be converging to the same energy. Thus the thermalization time between electrons and holes is estimated to be between 1 and 2 ps due to electron-hole scattering.

The situation is more complicated when injection occurs at 300K, as shown in Fig. 2. Here, both the electrons and the holes are injected with a mean energy less than the lattice temperature. This is particularly true for the holes which due to the larger effective mass are generated at very small excess energy above the band edge. A rapid increase in the hole energy over 200 fs is found due primarily to the absorption of TO and LO phonons and to a much smaller extent via e-h interaction. Thus, an equilibrium situation with the lattice is achieved quite soon after the end of the pulse due to the availability of thermal phonons which the cold carriers absorb. The electrons are also injected

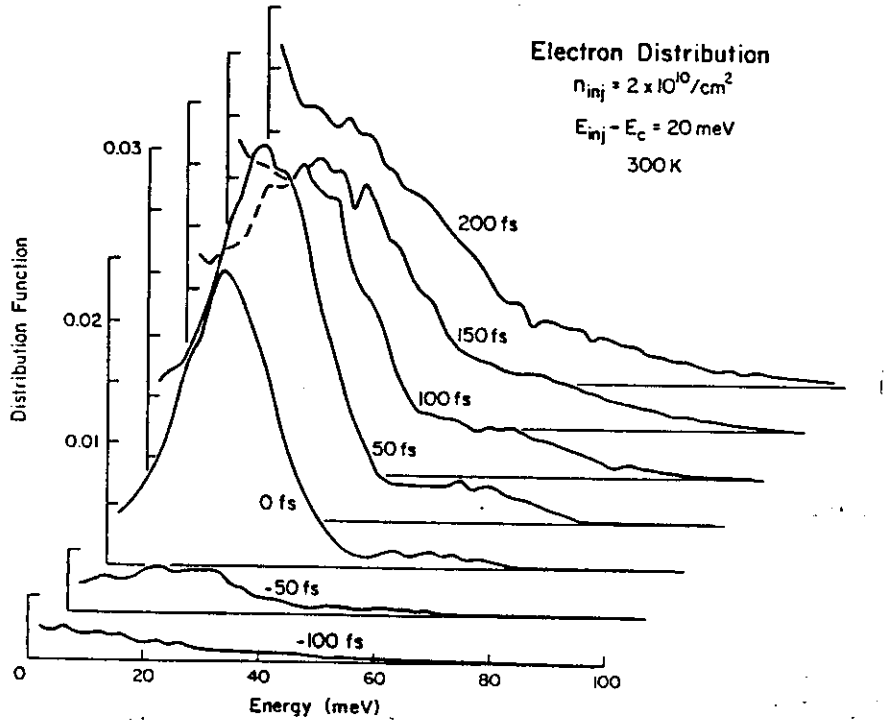

Figure 3. Electron distribution function as a function of energy at various times before and after a pump pulse at time t = 0.

943-11

with an average energy below the lattice energy, though only slightly less, and thus a lesser heating of the electron distribution is also observed in Fig. 2. This result indicates the possibility of creatinga nonequilibrium cold polar optical phonon distribution since LO phonons will be depleted due to excess absorption.

In Fig. 3 we show the calculated electron distribution function as a function of energy for various times before and after the pump pulse. As shown, the distribution evolves from a Gaussian shaped pulse to a Maxwellian shaped distribution over a time scale of about 200 fs. The simulated results for the electrons appear very similar to the experimental differential transmission spectrum[4,5] and are very similar to the results in which holes were not included[6,7] which supports the assertion that e-e scattering is the dominant relaxation mechanism. In simulations for which intercarrier scattering is 'shut off', the distribution is found to remain in its nonequilibrium shape without relaxing.

In Fig. 4 we show a similar plot for the calculated hole distribution at various times. The results here are quite different than for the electrons in Fig. 3. The hole distribution is located quite close to the band edge and thermalization occurs within 50 fs due to the smaller excess energy below the valence band edge and the increased h-h scattering rate due to the larger mass. More interesting is

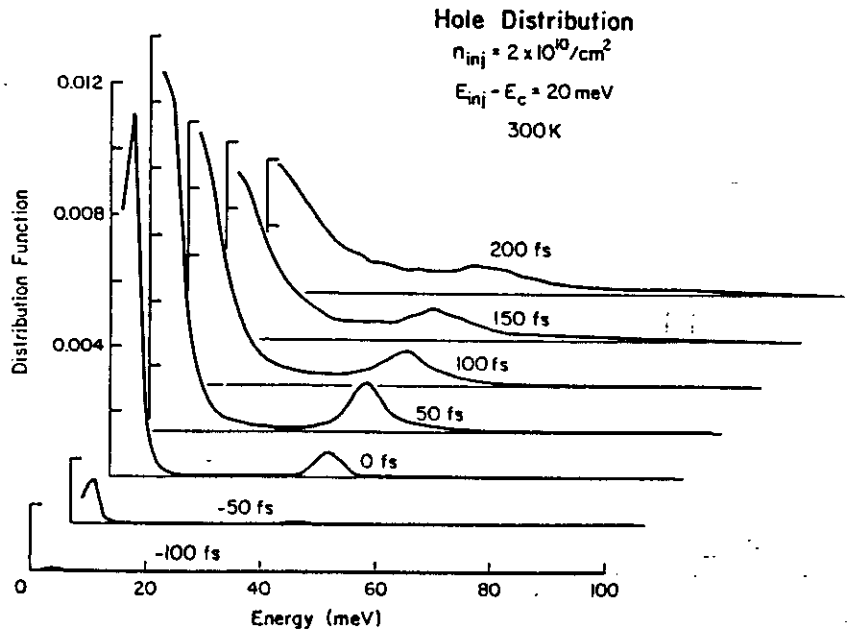

Figure 4. Hole distribution function as a function of energy at various times during a pump pulse at t = 0.

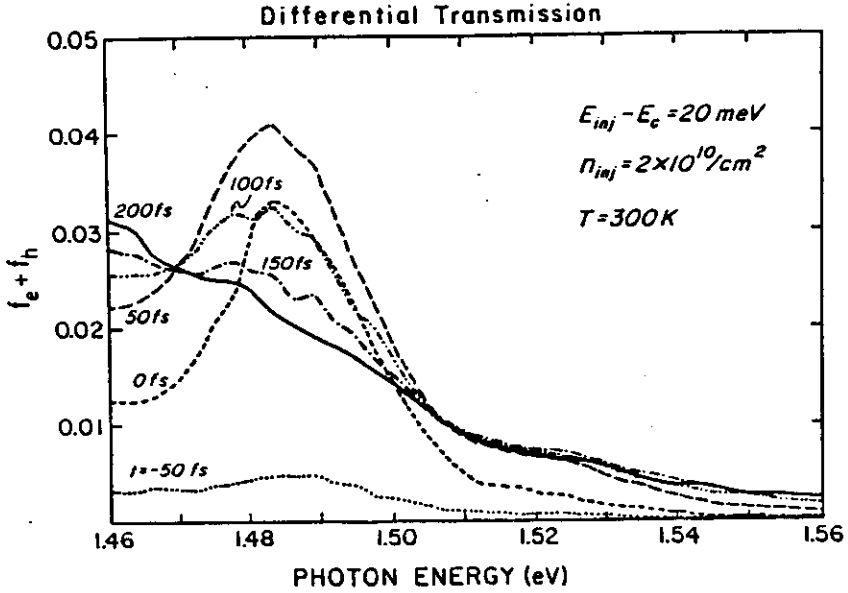

Figure 5. Differential transmission based on the distribution functions of Figs. 3 and 4 at the same times.

the evolution of a nonequilibrium distribution of holes after the pulse is over due to absorption of TO and LO phonons by the cold holes. Since the holes are generated in a very narrow energy range, a well developed phonon replica of this distribution appears at one phonon energy above the hole injection energy. This feature has not been observed in previous studies because the energy below the valence band edge corresponds to photon energies outside the optically coupled region of the experimental studies.[4,5] From a simple effective mass calculation, the expected photon energy range would be around 1.73 eV at room temperature. If such a phonon replica were experimentally observable, information on the hole-phonon coupling could be derived from the delay time between the pump pulse and the maximum of the replica at different temperatures. At low temperatures, such a feature could be used as a measure of the presence of nonequilibrium phonons generated during the relaxation process which are reabsorbed by the holes.

Experimentally, as discussed earlier, the observed quantity in the differential transmission spectrum is the sum of the electron and hole distributions as given in (2). From the separate electron and hole functions plotted in Figs. 3 and 4, we calculate the differential transmission as a function of photon energy in Fig. 5. Here we consider only the contribution of occupancy to the absorption coefficient and neglect excitonic effects which are beyond the scope of the present investigation. The differential transmission in Fig. 5 is in good agreement with the experimental time evolution observed by Knox et al.[4,5] By comparing Fig. 5 with those of Fig. 3 and Fig. 4, we see that the essential features of the spectrum follow those of the electron distribution which relaxes slower than the hole distribution.

943-11

Thus the simple minded assertion that the differential transmission spectrum represents the electron distribution seems to be correct, at least in this particular experiment.

To ascertain the dominant contribution to the energy relaxation in this experiment, we have calculated the power gain as a function of time for the electrons for the various scattering mechanisms and power exchanged via intercarrier collisions. As discussed earlier, inelastic scattering is necessary to provide diffusion in momentum or energy space in order to occupy states at the band edge after the pump pulse. Here, the power gain is calculated from the energy gain per particle over a fixed time step in the simulation (25 fs). The energy exchange is magnitude of the energy lost or gained per collision over the same time step. The results are shown in Fig. 6 for the electron system where we see that the e-e energy exchange rate is the dominant inelastic process followed by that of e-h scattering. The net LO phonon rate is only substantial for a short time during the pulse since the electrons are injected cooler than the lattice. The electron-hole power gain is slightly negative since part of the electron energy is transferred to the hole system which is initially much cooler.

Finally, in Fig. 7 we show the calculated differential transmission spectrum corresponding to n-doped samples with a background doping of $3.5\times10^{11}/cm^2$. An injected density of $3.5\times10^{11}/cm^2$ is generated by the laser pulse at 20 meV excess energy above the conduction band edge as in the previous case. As seen in Fig. 7, the relaxation occurs much more rapidly with an athermal peak observed for only 50 fs after the peak of the pulse. Intercarrier inelastic scattering is increased due

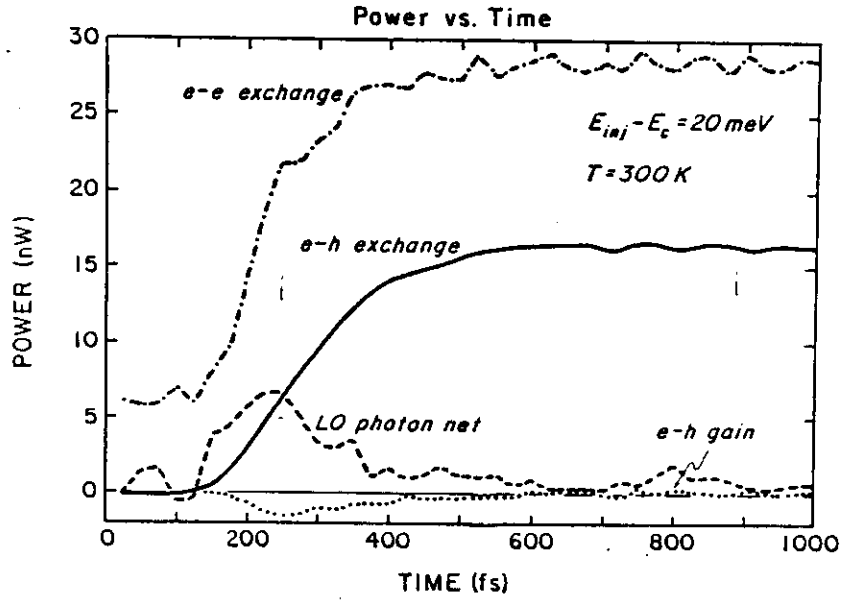

Figure 6. Power gain and exchange due to various scattering mechanisms for low density excitation into the quantum well.

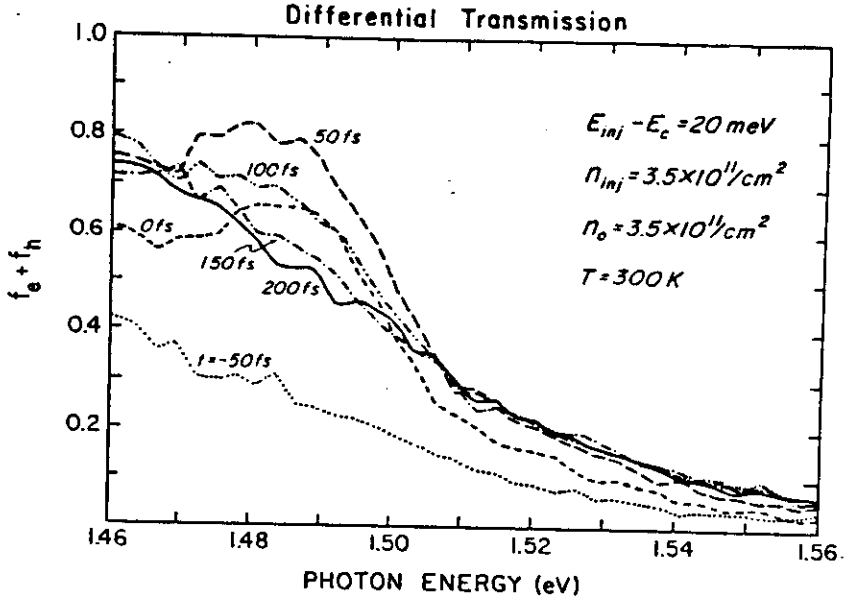

Figure 7. Differential transmission spectrum calculated for an injection density of $3.5 \times 10^{11}/cm^2$ and a background electron density of the same value at 300 K.

to the increased carrier density, particularly with the background carriers, which accounts for the increased relaxation rate in this case.

4. CONCLUSIONS

From the present Monte Carlo simulation of electron-hole excitation into a quantum well system, we conclude that the dominant features observed in the time resolved differential absorption measurements of Knox et al. are associated with relaxation of the electron distribution. This relaxation is primarily due to e-e interaction with e-h scattering playing a lesser role due to the heavier mass which tends to make the scattering more elastic. The apparent relaxation is increased for higher injection densities and for n-type samples due to increased intercarrier scattering. During and after excitation into the well, substantial heating of the hole distribution occurs at room temperature which should result in a phonon replica observable at higher photon energies in the differential transmission.

5. ACKNOWLEDGEMENTS

The authors would like to thank Wayne Knox for helpful discussions related to this work. The research was supported under ONR Contract No. N00014-87-K-0686.

943-11

6. REFERENCES

1. J.F. Ryan, R.A. Taylor, A.J. Turberfield, and J.M. Worlock, Surf. Sci. 170, 511(1986).
2. D.Y. Oberli, D.R. Wake, M.V. Klein, J. Klem, T. Henderson, and H. Morkoc, Phys. Rev. Lett. 59, 696 (1987).
3. M. Rosker, F. Wise, and C.L. Tang, Appl. Phys. Lett. 49, 1714 (1986).
4. W.H. Knox, C. Hirlimann, D.A.B. Miller, J. Shah, D.S. Chemla, and C.V. Shank, Phys. Rev. Lett. 56, 1191 (1986).
5. W.H. Knox, D.S. Chemla, and G. Livescu, HCIS-5 conference proceedings, to be published.
6. S.M. Goodnick and P. Lugli, Appl. Phys. Lett. 51, 585 (1987).
7. D.W. Bailey, M. Artaki, C. Stanton, and K. Hess, J. Appl. Phys. 62, 4639 (1987)
8. C. Jacoboni and L. Reggiani, Rev. Mod. Phys. 55, 645 (1983).
9. S.M. Goodnick and P. Lugli, Phys. Rev. B37, 2578 (1988)
10. M. Altarelli, in Heterojunctions and Semiconductor Superlattices, G. Allan, G. Bastard, N. Boccara, M. Lannoo, and M. Voos, eds., Springer-Verlag, Berlin, 1986, pp. 12-37.
11. B. K. Ridley, J. Phys. C15, 5899 (1982).
12. M. Yokoyama and K. Hess, Phys. Rev. B33, 5595 (1986).
13. P. Lugli and S.M. Goodnick, Phys. Rev. Lett. 59, 716 (1987).
14. J.D. Wiley, in Semiconductors and Semimetals: Vol. 10, R.K. Willardson and A.C. Beer, eds., Academic Press, New York, 1975, pp. 91-174.

To be published in "Spectroscopy of Nonequilibrium Electrons and Phonons", Eds. C.V Shank and B.P. Zakharchenya

MONTE CARLO CALCULATION OF HOT ELECTRONS AND HOT PHONONS

P. Lugli

Dipartimento di Ingegneria Meccanica

II Università di Roma

Via E. Carnevale

00173 Roma, Italy

ABSTRACT

The Monte Carlo (MC) technique has been over the last couple of decades a very useful tool for the study of hot carrier transport in semiconductors. In the following we will concentrate on a fairly new development of the MC algorithm, directed towards the study of ultrafast phenomena. In particular we will show haw it is possible to simulate the carrier dynamics in parallel to the evolution of the phonon distribution, thus accounting for hot-phonon effects. Furthermore we will concentrate on the methods that allow to incorporate intercarrier scattering into the simulation. The fact that no assumptions on the form of the phonon or the electron distributions are required, makes the MC method preferable with respect to other techniques.

The study of LO-phonon perturbations as a result of the relaxation of photoexcited carriers in polar semiconductors is presented. Bulk GaAs and InP, as well as GaAs-AlGaAs heterostructures are analized. Good agreement is found with available experimental results from time resolved luminescence and Raman measurements. The strong phonon emission by the high-energy photoexcited electrons in the first stage of their relaxation (within a few tenths of a picosecond) is found to drive the phonon distribution strongly out of equilibrium. After the excitation, reabsorption of the emitted phonons by the carriers and nonelectronic phonon-decay processes bring the distribution back to its equilibrium value. The field dependent case in GaAs is also discussed, showing peculiar drag and heating phenomena associated to phonon perturbations.

1. Introduction

As the name suggests, the Monte Carlo method (MC) is based on the selection of random numbers (Hammersley and Handscomb 1964; Yu Schreider 1966; Spanier and Gelbard 1969; Jacoboni and Reggiani 1983; Jacoboni and Lugli 1989). In its present form, the method is attributed to Fermi, Von Neumann, and Ulam, who developed it for the solution of problems related to neutron transport. In principle, the MC method can be considered as a very general mathematical tool for the solution of a great variety of problems.

Among the various applications of the method the following are probably the most important:

* Integro-differential equations
* Matrix inversion
* Transport of nuclear particles
* Transport in semiconductors
* Modeling of semiconductor devices
* Process simulation

An important feature of the MC technique is that more precise results can be obtained by generating larger numbers of points. More generally, being based on random numbers, the results obtained with a MC procedure are never exact, but rigorous in a statistical sense: the exact result lies in given intervals with given probabilities. The uncertainty on the results is strictly related to the variance of the possible outcomes and it is smaller if the size of the sample (i.e. the amount of computations devoted to the solution of the problem) is larger. One basic element of the numerical procedure is the possibility to generate random numbers with given distributions starting from pseudorandom numbers uniformly distributed between 0 and 1. Modern computers provide sequences of numbers obtained with precise mathematical

algorithms, starting from a given element (seed). For each seed, the sequence is perfectly predictable. However it satisfies a large number of statistical test of randomness. Those pseudorandom numbers offer two great advantages: they can be generated in a very fast way, and they are reproducible, when desired, as for example in debugging.

The applications of MC methods can be divided into two major groups. One consists of direct reproduction on a computer of the microscopic dynamics of the physical process in a system which is already statistical in its nature. We use in this case the term "MC simulation". The second group consists of MC methods devised for the solution of well defined mathematical equations. In such cases the methods are used to solve the equations that describe the problem of interest. The majority of real cases are a mixture of the two extreme limits indicated above. The application to the study of semiconductor transport is a good example. In fact, transport problems are statistical in nature, but are also accurately described by well defined transport equations. A MC method applied to the solution of such equations may or may not correspond to the direct simulation of the physical system under examinatiopn. For instance, the MC solution of Boltzmann equation (BE) not only gives the distribution function that verifies the equation, but also yields information that are lost in BE itself. On the hand, the direct simulation is at times very inefficient, as for example in the analysis of situations that are rare in the actual physical system. In such cases it is necessary to distort the simulation by applying some more sophisticated MC techniques that reduce the variance of the quantity of interest, giving up the advantages offered by the direct simulation.

In the present work we will briefly discuss the principle of the MC method, and illustrate in some detail how it is possible to account for special effects related to the microscopic phenomena involved in semiconductor transport under highly nonequilibrium conditions. In particular we will address the question of possible effects of nonequilibrium optical phonon

distributions on the dynamics of hot carriers. Such problem has been discussed since a long time, expecially in connection with fundamental aspects of charge transport (Peierls 1930; Klemens 1951; Parrot 1957). Steady state phenomena associated to high field transport have later been addressed (Kocevar 1972,1985; Rieger et al. 1988, 1989). More recently, the influence of phonon disturbances optically excited charge carriers in semiconductors is becoming a widely investigated and debated topic (Shah et al. 1970; Von der Linde et al. 1980; Pötz and Kocevar 1983; Collins and Yu 1984; Kash J. et al. 1985; Price 1985; Shah et al. 1985; Kash K. et al. 1985; Ryan et al. 1986; Pugnet et al. 1986; Leo et al. 1988; Lugli 1988; Lugli and Goodnick 1987; Lugli et al. 1987a,1987b,1989; Mickevicius and Reklaitis 1987). The main scientific motivation comes from the rapid development of picosecond and subpicosecond laser spectroscopy, which allows the study of the fastest relaxation phenomena in solids and thereby also some fundamental hot carrier-hot phonon processes.

As the hot carrier system loses its energy mainly through emission of phonons, the mean phonon occupation number of the most strongly coupled vibrational modes will increase over its thermal equilibrium Planck distribution N_L at the lattice temperature T_L. This phonon amplification will ultimately depend on the rate at which the perturbed modes dissipate their excess energy by way of phonon-decay processes into the "heat bath" of the electronically inactive lattice modes. Figure 1 shows the energy flow to, within and out of a coupled carrier-phonon system for the most general case of several types of carriers and electronically active phonons: electrons in different conduction band valleys of Γ-,L- and X-symmetry, long wavelength longitudinal (LO) and transverse (TO) optical phonons, and the remaining types of intervalley and acoustical phonons. Depending on the material, on the excitation level and on temperature, different types of carriers, lattice modes and carrier-phonon (c-ph) coupling will dominate the overall energy transfer from the external d.c. or laser field into the lattice. Direct experimental evidence for strongly amplified optical phonon distributions has come

from time-resolved Raman spectroscopy. The ensuing feedback of energy into the carrier system through the relative increase of phonon reabsorptions has been only indirectly evidenced through a heavily reduced cooling rate of highly laser-pulse excited electron-hole systems. However, for the high carrier concentrations involved in most of these experiments, possible contributions of carrier-carrier (c-c) scattering, screening of long-range c-ph couplings, spatial carrier diffusion, and collective plasma effects have not allowed an unambiguous separation of hot-phonon effects from the experimental data. Great efforts are therefore presently undertaken towards a sufficiently accurate theoretical description of highly excited c-ph systems to achieve deeper insights into the transient high-field response of semiconductors and solids in general. The best-suited framework for such investigations is the semiclassical transport theory, and most of the work on hot phonons has indeed been formulated in terms of the Boltzmann equation for the phonons, but always with simplifying assumptions about the functional form of the distribution function of the carriers (Kocevar 1985; Luzzi 1985; Poetz 1987; Cai et al. 1987).

The corresponding transport model for the carriers and optical phonons is set up in Sect. 2. The principles of the Monte Carlo method are outlined in Sect. 3, together with specific features directed to the study of carrier-carrier scattering and hot-phonon effects. Section 4 deals with applications on the photoexcitation of polar semiconductors, for the simplified case of monoenergetic electron excitation in bulk GaAs and GaAs/GaAlAs quantum wells (QW) (here the role of slab modes will be also discussed). The more realistic case of electron excitation out of the threefold valence band of GaAs and InP will be presented in Sect. 5. A direct comparison of the MC results with existing experimental data will be given. Section 6 will illustrate the MC analysis of the field-dependent case in GaAs.

2. The Transport Model

The dynamical evolution of the carrier phonon system under space-homogeneous conditions can be adequately described by the coupled Boltzmann equations:

$$\frac{\partial f_{\mathbf{k}}}{\partial t} = \frac{\partial f_{\mathbf{k}}^{(i)}}{\partial t}\Big|_{c-ph} + \frac{\partial f_{\mathbf{k}}^{(i)}}{\partial t}\Big|_{c-c} + \frac{\partial f_{\mathbf{k}}^{(i)}}{\partial t}\Big|_{c-impurity} \tag{1}$$

$$\frac{\partial N_{\mathbf{q}}^{(j)}}{\partial t} = \frac{\partial N_{\mathbf{q}}^{(j)}}{\partial t}\Big|_{ph-c} + \frac{\partial N_{\mathbf{q}}^{(j)}}{\partial t}\Big|_{ph-ph} \tag{2}$$

where $f_{\mathbf{k}}$ and $N_{\mathbf{q}}$ are respectively the carrier and the phonon distribution functions. The superindex i and j indicate respectively the type of carrier (electrons or holes) and of phonon modes (LO, TO,...) considered. As long as the carrier densities are not too high (typically lower than $10^{17} cm^{-3}$) , so that no efficient coupling exists between electrons and holes only the electron dynamics need to be accounted for. In the same spirit, we assume unscreened electron-phonon interactions.

The time-dependent transport equations for carriers and phonons are coupled through the occurence in the carrier-phonon collision integrals of both carrier and phonon distribution functions (Conwell 1967). A decisive simplification of the phonon equation comes from the possibility to use a temperature-dependent relaxation time for the phonon-phonon interactions, τ_{op}, in the form:

$$\frac{\partial N_{\mathbf{q}}}{\partial t}\Big|_{ph-ph} = -\frac{N_{\mathbf{q}} - N_L}{\tau_{op}}, \tag{3}$$

where N_L is the thermal Plank distribution

$$N_L = \left(e^{\hbar\omega/k_B T_L} - 1\right)^{-1}, \tag{4}$$

and $\hbar\omega$ is the phonon energy.

The relaxation-time approximation is justified by the fact that the phonon-phonon interactions are dominated by the decay of the LO phonons into pairs of electronically nonactive phonons from zone-boundary modes. Zero-temperature values of the phonon lifetime, τ_{op},

are generally of the order of 10 ps, with a weak decrease with temperature (Klemens 1966). Time-resolved phonon spectroscopy has yielded a rather wide range of values for τ_{op}, between 7 ps (Von der Linde at al. 1980) and 28 ps (Mooradian and Wright 1966). The reason for this spread of experimentally determined LO phonon lifetimes seems to have two sources. Firstly, the quality of the sample surface can strongly influence the decay dynamics within the thin light-absorption layer (Damen et al. 1970). Secondly, the decay rate of a nonthermal phonon population might contain strong contributions from the reabsorption by the photogenerated carriers of the initially excited phonons. This point will be discussed in detail later. Our choice of τ_{op} equal to 7 ps at 77 K and 3.5 at 300 K is in agreement with the most recent experimental results (Kash J. et al. 1985).

Several theoretical approaches for the solution of Eqs. 1 and 2 have been presented in the literature. Details about the various methods can be found in Pugnet et al. (1981), Pötz and Kocevar (1983), Cai et al. (1987), Pötz (1987). Certainly one of the most interesting is due to Collet and Amand (1986) who directly solved the coupled transport equations through a discretization in q-space and in time to obtain the evolution of the carrier and phonon distributions and of the mean electron-hole plasma energy during and after 80 femtosecond laser excitation pulses of varying intensity. Another method, based on the carrier-temperature concept, is of particular interest here since it originated the MC investigation of phonon perturbations. In this approach to d.c. field transport, the carriers are assumed to be characterized by a heated and drifted Maxwellian (HDM) distribution (Kocevar 1981, 1985). In the first attempt to use a MC technique in the study of phonon perturbations, an iterative hybrid procedure was developed that coupled the HDM scheme to a one-particle MC simulation of nonohmic transport (Bordone et al. 1986,1987).

The full consistent Monte Carlo simulation, developed for the case of photoexcitation in bulk GaAs (Lugli et al. 1987a, 1987b; Lugli 1988; Lugli et al. 1989) and in QW's (

Goodnick and Lugli 1986; Lugli and Goodnick 1987), and of high fields in GaAs (Rieger et al. 1988,1989) , will be presented in the next section.

3. The Monte Carlo Algorithm

The basic principles of the MC simulation of semiconductor transport will be illustrated. A more detailed analysis can be found in Jacoboni and Reggiani (1983) and Jacoboni and Lugli (1989).

3.1 Fundamentals

The Monte Carlo method, as applied to charge transport in semiconductors, consists of a simulation of the motion of one or more electrons inside the crystal, subject to the action of external forces due to applied electric and magnetic fields and of given scattering mechanisms (Kurosawa 1966; Fawcett et al. 1970; Price 1979; Jacoboni and Reggiani 1983; Jacoboni and Lugli 1989). The durations of the carrier free flights between two successive collisions and the scattering events involved in the simulation are selected stochastically in accordance with some given probabilities describing the microscopic processes. As a consequence, any Monte Carlo method relies on the generation of a sequence of random numbers with given distribution probabilities.

When the purpose of the analysis is the investigation of a steady-state, homogeneous phenomenon, it is sufficient in general to simulate the motion of one single electron; from ergodicity we may assume that a sufficiently long path of this sample electron will give information on the behaviour of the entire electron gas. When, on the contrary, the transport process under investigation is not homogeneous or is not stationary, then it is necessary to simulate a large number of electrons and follow them in their dynamic histories in order to obtain the desired information on the process of interest. We will refer to the latter as

"Ensemble Monte Carlo" (EMC).

Let us summarize here the structure of a typical Monte Carlo program. The details of each step of the procedure will be given in the following sections. For the sake of simplicity we shall refer to the case of electrons in a simple semiconductor subject to an external electric field $\mathbf{E}$. The simulation starts with one electron in given initial conditions with wavevector $\mathbf{k}_o$; then the duration of the first free flight is chosen with a probability distribution determined by the scattering probabilities. During the free flight the external forces are made to act according to the relation

$$\hbar\dot{\mathbf{k}} = -e\mathbf{E} \tag{5}$$

Then a scattering mechanism is chosen as responsible for the end of the free flight, according to the relative probabilities of all possible scattering mechanisms. From the differential cross section of this mechanism a new $\mathbf{k}$ state after scattering is randomly chosen as initial state of the new free flight, and the entire process is iteratively repeated.

3.2 Definition of the physical system

The starting point of the program is the definition of the physical system of interest, including the parameters of the material and the values of physical quantities, such as lattice temperature T and electric field. The dispersion relation $\epsilon(\mathbf{k})$ is usually given in the form

$$\epsilon(\mathbf{k}) = \frac{\hbar^2 k^2}{2m}, \tag{6}$$

$$\epsilon(\mathbf{k}) = \frac{\hbar^2}{2}\left[\frac{k_l^2}{m_l} + \frac{k_t^2}{m_t}\right], \tag{7}$$

$$\epsilon(\mathbf{k}) = ak^2[1 \mp g(\vartheta, \psi)]. \tag{8}$$

Equation (6) (spherical case) represents a band with spherical equienergetic surfaces with a single scalar effective mass m, and it is appropriate for the minimum of the conduction

band located at Γ and for the maximum of the split-off valence band. This simple case is generally adopted as a model for any material when rough estimates of transport properties are sought.

Equation (7) (ellipsoidal case) represents a band with ellipsoidal equienergetic surfaces, with a tensor effective mass. The ellipsoids have rotational symmetry around the crystallographic directions which contain the centers of the valleys. Here, k_l and k_t are the longitudinal and transverse components of k with respect to these directions; $1/m_l$ and $1/m_t$ are the longitudinal and tranverse components, respectively, of the inverse effective-mass tensor. This case is appropriate for the minima of the conduction band located at L and along Δ; for symmetry reasons several equivalent valleys are present (many-valley model).

Equation (8) is appropriate for the two degenerate valence bands,where the definition of an effective mass tensor is not possible. This equation represents bands with warped equienergetic surfaces (here $\mp$ refer to heavy and light holes, respectively). ϑ and ϕ are the polar and azimuthal angles of k with respect to crystallographic axes. $g(\vartheta,\phi)$ contains the angular dependence of the two degenerate bands, given by (Ottaviani et al. 1975)

$$g(\vartheta,\phi) = \left[b^2 + c^2(sin^4\vartheta cos^2\phi sin^2\phi + sin^2\vartheta cos^2\vartheta)\right]^{1/2},$$

with

$$a = \frac{\hbar^2|A|}{2m_0},\ b = \frac{|B|}{|A|},\ c = \frac{|C|}{|A|},$$

where A,B and C are the inverse valence-band parameters (Dresselhaus et al. 1955)

For values of k far from the minima of the conduction band and/or from the maxima of the valence band, the energy deviates from the simple quadratic expressions seen above, and nonparabolicity occurs. For the conduction band, a simple analytical way of introducing nonparabolicity is to consider an energy-wavevector relation of the type

$$\epsilon(1+\alpha\epsilon) = \gamma(\mathbf{k}) \qquad (9)$$

or

$$\epsilon(\mathbf{k}) = \frac{-1+\sqrt{1+4\alpha\gamma}}{2\alpha}, \qquad (10)$$

where $\gamma(\mathbf{k})$ is given by one of the right-hand sides of Eqs. (6) and (7). α is a nonparabolicity parameter, which can be related to other band quantities.

It is also possible to use the full band structure $\epsilon(\mathbf{k})$, calculated for example by pseudopotential methods and tabulated in a 3-dimensional grid (Tang and Hess 1983; Fischetti and Laux 1988). It is worth noting that, among the parameters that characterize the material, the least known are the coupling strengths describing the interactions of the electron with the lattice and/or extrinsic defects inside the crystal.

At this level we also define the parameters that control the simulation, such as the duration of each subhistory, the desired precision of the results, and so on.

The next step in the program is a preliminary calculation of each scattering rate as a function of electron energy. This step will provide information on the maximum value of these functions, which will be useful for optimizing the efficiency of the simulation. Finally, all cumulative quantities necessary for the calculation of average values must be put at zero in this preliminary part of the program.

3.3 Initial conditions

If a very high electric field is applied, and an energy of the order of K_BT is initially given to the electron, this energy will be much lower than the average energy in steady-state conditions, and during the transient it will increase towards its steady-state value. As a consequence, the electron response to the field, in terms of mobility, may be initially much higher than that of stationary conditions. This phenomenon corresponds to the transient overshoot and it is reflected in real space by initial free flights which are much longer than in stationary conditions because of an abnormally large momentum relaxation time.

When a simulation is made to study a transient phenomenon and/or a transport process in a nonhomogeneous system (as in the case of device simulation), then it is necessary to simulate many electrons separately; in this case the distribution of the initial electron states for the particular physical situation under investigation must be taken into account and the initial transient becomes an essential part of the problem to be solved (an example will be given later describing the photoexcitation case).

3.4 The free flight, self scattering.

The electron wavevector $\mathbf{k}$ changes continuously during a free flight because of the applied field, according to Eq. 5. Thus if $P[\mathbf{k}(t)]dt$ is the probability that an electron in the state $\mathbf{k}$ suffers a collision during the time interval dt, the probability that an electron which had a collision at time $t = 0$ has not yet undergone another collision after a time t is

$$exp\left[-\int_0^t P[\mathbf{k}(t')]dt'\right]. \tag{11}$$

Consequently, the probability $P(t)$ that the electron will suffer its next collision during dt around t is given by

$$P(t)dt = P[\mathbf{k}(t)]exp\left[-\int_0^t P[\mathbf{k}(t')]dt'\right]dt. \tag{12}$$

Because of the complexity of the integral at the exponent, it is impractical to generate stochastic free flights with the distribution of Eq. (11) , starting from evenly distributed random numbers r and applying the direct or rejection techniques; with this approach an integral equation would need to be solved for each scattering event. Rees (1968,1969) has devised a very simple method to overcome this difficulty. If $\Gamma \equiv 1/\tau_0$ is the maximum value of $P(\mathbf{k})$ in the region of $\mathbf{k}$ space of interest, a new fictitious "self-scattering" is introduced such that the total scattering probability, including this self-scattering, is constant and equal to Γ. If the carrier undergoes such a self-scattering, its state $\mathbf{k}'$ after the collision is taken

to be equal to its state $\mathbf{k}$ before the collision, so that in practice the electron path continues unperturbed as if no scattering at all had occured. Generally it is sufficient that Γ be not less than the maximum value of $P(\mathbf{k})$; furthermore, as we shall see below, Γ can be extended to a convenient function of energy.

Now, with a constant $P(\mathbf{k}) = \tau_0^{-1}$, Eq. 12 reduces to $P(t) = \frac{1}{\tau_0}exp(-t/\tau_0)$ and random numbers r can be used very simply to generate stochastic free flights t_r from

$$t_r = -\tau_0 ln(r). \tag{13}$$

The computer time "wasted" in taking care of self-scattering events is, in general, more than compensated for by the simplification in calculating the free-flight duration.

As regards the choice of the constant Γ, we note that in general $P(\mathbf{k})$ is a function of the electron energy ϵ; a suitable choice for Γ is then the maximum value of $P(\epsilon)$ in the region of energies which are expected to be sampled during the simulation. When $P(\epsilon)$ is not a monotonic function of ϵ, its maximum value must be estimated in some way, for example, with a tabulation at the beginning of the computer program. When $P(\epsilon)$ is an increasing function of ϵ, as is often the case, one can take $\Gamma = P(\epsilon_M)$, where ϵ_M is a maximum electron energy with negligible probability of being achieved by the carrier during the simulation. It must be observed, however, that the range of energy "visited" by the electron during the simulation is not known at the beginning, when Γ is to be chosen. Therefore, an estimate must be made for ϵ_M, keeping in mind that ϵ_M cannot be taken too large, if one is to prevent an unnecessarily large value of Γ that would result in a waste of computer time for self-scattering events. Appropriate action must be taken if the energy during the simulation becomes larger than ϵ_M.

For a semiconductor model that contains several valleys, a different value of ϵ_M may be appropriately taken in each type of valley.

Sometimes the total scattering probability $P(\epsilon)$ has a large variation around some threshold value due to a strong scattering mechanism with a given activation energy (a typical case is intervalley scattering from central to upper valleys in polar semiconductors). In this case, a single value of Γ may result in a very large number of self-scattering events at low electron energies. It is then possible to introduce a piecewise functions $\Gamma(\epsilon)$ with more than one step. In this case, the straightforward extension of Eq.(13) is given by

$$t_r = t_i + \tau_i[-ln(r) - \sum_{j=1}^{i-1}(t_j - t_{j-1})/\tau_j] \qquad (14)$$

where the subindeces refer to the discretization of the energy domains. The effectiveness of the procedure depends critically on the additional computation time required by the calculation of the free flight compared to the time saved through the reduction of self-scattering events.

3.5 The scattering process

During a free flight, the electron dynamics is governed by Eq. (5) so that at its end the electron wavevector and energy are known, and all scattering probabilities $P_i(\epsilon)$ can be evaluated, where i indicates the ith scattering mechanism. The probability of self-scattering will be the complement to Γ of the sum of the P_i's. A mechanism must then be chosen among all those possible: given a random number r, the product $r\Gamma$ is compared with the successive sums of the P_i's, and a mechanism is randomly selected.

If all scattering have been tried and none of them has been selected, it means that $r\Gamma > P(\epsilon)$, and a self-scattering occurs. A self-scattering event is therefore most time consuming, since all P_i's must be explicity calculated. However, the process may be shortened by use of an expedient that might be called fast self-scattering. It consists of setting up a mesh of the energy range under consideration at the beginning of the simulation and then recording in a vector the maximum total scattering probability $P^{(l)}$ in each energy interval $\Delta\epsilon^{(l)}$ (energy

intervals equally distributed on a logarithmic scale may be useful). At the end of the flight if the electron energy falls in the nth interval, before trying all P_i's separately, one compares $r\Gamma$ with $P^{(n)}$. At this stage if $r\Gamma > P^{(n)}$ then a self-scattering certainly occurs; otherwise all P_i's will be successively evaluated. Thus only when $P(\epsilon) < r\Gamma < P^{(n)}$ does a self-scattering occur which requires the evaluation of all P_i's.

It is in general more convenient to tabulate all scattering probabilities in a mesh of the energy axis and to use look-up tables during the simulation. This is particularly true when very sophisticated scattering probabilities are used which require a large amount of computation, as, for example, when the full three-dimensional band structure is taken into account.

As a final consideration we may note that some scattering mechanisms may depend on the distribution function itself, which is the final result of the simulation, and therefore they are not known at the beginning, when the program is set up. This is the case, for example, of intercarrier scattering and of phonon or impurity scattering when screening is to be considered, since the screening depends on the carrier distribution. In these cases it is necessary to establish some self consistent procedure, as will be shown later.

3.6 The choice of the state after scattering

Once the scattering mechanism that caused the end of the electron free flight has been determined, the new electron state after scattering, $\mathbf{k}_a$, must be chosen as final state of the scattering event. If the free flight ended with a self-scattering, $\mathbf{k}_a$ must be taken as equal to $\mathbf{k}_b$, the state before scattering. When, in contrast, a true scattering occured, then $\mathbf{k}_a$ must be generated stochastically, according to the differential cross section of that particular mechanism.

3.7 The Ensemble Monte Carlo (EMC)

We shall consider here the case of a homogeneous electron gas with time-dependent behavior. In particular, it is of interest to study the transient dynamic response to a sudden change in the value of an applied field or in the presence of laser excitation. In this situation many particles must be independently simulated with appropriate distributions of initial conditions. Provided the number of simulated particles is sufficiently large, histograms obtained by reading the electron wavevectors or energies at regular intervals of time provide the distribution function $f(\mathbf{k},t)$ or $f(\epsilon,t)$, respectively. If a single quantity A is of interest, its average value can be obtained on this sample ensemble as a function of time. To determine the precision of the results obtained, one separates the entire ensemble into a certain number of subensembles and estimates for each of them the quantity of interest A. Then their avarage value and standard deviation can be taken, respectively, as the most probable value and the statistical uncertainty of A.

The transient dynamic response obtained by means of the simulation will, of course, depend upon the initial conditions of the carriers, and these must be assumed according to the situation to be explored.

3.8 Many particle effects

Many physical systems of interest are characterized by high carrier densities. In this respect, interparticle scattering and degeneracy effects might be of great importance. In the following we will describe possible algorithms used to include such phenomena in a MC simulation.

Carrier-carrier scattering

Following the analysis of Bohm and Pines (1962) two main contributions to the carrier -carrier scattering can be identified:

- the individual carrier-carrier interaction via a screened Coulomb potential of the form

$$V(r) = \frac{e^2}{\kappa r} e^{-\beta r} \tag{15}$$

which accounts for two-body short-range interaction, where β is the inverse screening length;
- the electron-plasmon interaction, which accounts for the collective long-range behaviour of the eletron gas.

The scattering rates for electron-plasmon interaction are calculated from Fermi Golden rule, as shown in Lugli and Ferry (1985a,1985b), and used directly in the MC simulation. Such scattering is particularly important when fast electrons are injected into heavily doped regions, as for example in ballistic devices.

In semiconductors, the plasmon energy at reasonable density can be of the same order of magnitude as the characteristic phonon energies (for example in GaAs at a concentration of $5 \times 10^{17} cm^{-3}$ the phonon energy $\hbar\omega_p$ is equal to 30 meV).

Using the screened potential of Eq. (15) the scattering rate for electron-electron (e-e) scattering is obtained using the Fermi Golden rule. For non-degenerate situations we have :

$$\Gamma_{e-e}(\mathbf{k}_0) = \frac{m e^4}{\hbar^3 V \kappa^2} \sum_{\mathbf{k}} f_{\mathbf{k}} \frac{|\mathbf{k}-\mathbf{k}_0|}{\beta^2(|\mathbf{k}-\mathbf{k}_0|^2+\beta^2)}. \tag{16}$$

The choice of the wave vector $\mathbf{k}$ determines the value of the wave-vector difference $\mathbf{g} = \mathbf{k} - \mathbf{k}_0$ of the two electrons before the collision. After the collision the relative wave vectors will be changed to $\mathbf{g}' = \mathbf{k}' - \mathbf{k}_0'$. Since the scattering conserves the magnitude of $\mathbf{g}$, the new vector $\mathbf{g}'$ can be determined from the angular distribution probability $P(\theta)d\theta$ with equal to the angle between $\mathbf{g}$ and $\mathbf{g}'$. The angular probability $P(\theta)d\theta$, determined from the differential scattering probability $S(\mathbf{g},\mathbf{g}')$ is given by

$$P(\theta)d\theta = \frac{sin\theta d\theta}{g^2 sin^2(\theta/2)+\beta^2}, \tag{17}$$

with $g = |\mathbf{g}|$.

The previous analysis can be easily extended to account for the electron-hole interaction (but the following is valid also for the interaction between electrons in different valleys). If the two body coulomb interaction can still be represented by a screened potential,with electrons and holes characterized by two different temperatures, respectively T_e and T_h, the inverse classical screening length β is given by :

$$\beta^2 = \frac{4\pi n e^2}{\kappa k_B}[\frac{1}{T_e} + \frac{1}{T_h}] \tag{18}$$

In the calculation of the scattering rates using Fermi golden rule, the same procedure seen before for the e-e scattering is followed, introducing the relative wavevector g and the reduced mass μ defined by

$$\mathbf{g} = 2\mu(\frac{\mathbf{k}_0}{m_e} - \frac{\mathbf{k}}{m_h}) \tag{19}$$

and

$$\mu = \frac{m_e m_h}{m_e + m_h}, \tag{20}$$

where m_e and m_h are respectively the electron and hole effective mass.

The total scattering rate for electron-hole interaction is then given by

$$\Gamma_{e-h}(\mathbf{k}_0) = \frac{2\mu e^4}{\hbar^3 \kappa^2 V} \sum_{\mathbf{k}} f_{\mathbf{k}} \frac{g}{\beta^2[g^2 + \beta^2]} \tag{21}$$

The inclusion of the screened Coulomb interaction into the standard MC algorithm presented some difficulties, due to the dependence of the total scattering rates on the carrier distribution function. In the one particle MC, the distribution function is one of the outputs of the calculation. Thus, some sort of self-consistent calculation must be performed in which an assumed $f(\mathbf{k})$ is used to evaluate scattering probabilities and the same $f(\mathbf{k})$ results as solution.

The use of the Ensemble Monte Carlo technique greatly simplifies the treatment of carrier-carrier scattering. Since the distribution function is built in the simulated ensemble of carriers, the sum over f_n in Eqs. (16) and (21) can be properly taken into account at any point of the simulation, even under transient conditions. To this aim two alternative methods have been proposed.

The first one (Lugli and Ferry 1983,1985b,1985c) starts from the realization that a sum over the distribution function is simply an ensemble average of a given quantity. Thus the scattering rate for a carrier-carrier scattering can be expressed as

$$\Gamma_{e-e}(\mathbf{k}_o) = \frac{2\mu e^2}{\hbar^3 \kappa^2 N} \sum_{all\ carriers} \frac{g}{\beta^2[g^2 + \beta^2]}, \tag{22}$$

where μ, g and β are given in general by Eqs. (18-20) which include the case of one-carrier plasma as well as the one of a many-component plasma. The sum is taken over all wavevectors of the sub-ensemble formed by the carriers of a given type. It is obvious that the scattering rate defined from the ensemble average does not require any assumption on the form of the distribution function. Furthermore, it is not limited to steady-state situations, but applies as well to the study of transient phenomena. The main limitation comes from the computational requirement of Eq. (22), which involves a tridimensional sum over the ensemble of carriers, and depends on k rather than on its amplitude. In the implementation in Lugli and Ferry (1983,1985c) the scattering rates are tabulated over a two-dimensional grid at fixed times during the simulation (a three-dimensional grid could also be used). The time step for the tabulation depends critically on the specific situation of interest. If the distribution function changes rapidly over short period of times (such as for examples following laser photoexcitation), the scattering rate should be calculated in such a way as to reproduce the changes in the distribution. Tipically, time-steps of 100 femtoseconds are used. On the contrary, if the time scale of the relevant physical processes is of the order of picoseconds

or longer, such a fine discretization in time is not necessary. In the limit of steady-state situations, no update is required any longer in the tabulation of the scattering rate. The carrier-carrier scattering falls into the category of interactions whose rate changes in time. It is therefore important to let the maximum scattering rate adjust itself during the simulation (that is to have a self-scattering variable in time), to avoid the unphysical occurence of negative rates for real processes.

A second method to treat the carrier-carrier scattering is based on a rejection algorithm (Brunetti et al. 1985; Goodnick and Lugli 1988a,1988b). A self-scattering internal to the interparticle scattering is introduced by substituing the term $g/(g^2+\beta^2)$ in Eq. (22) with its maximum value $1/2\beta$. This enhanced carrier-carrier scattering rate is introduced among the other mechanisms. When an intercarrier collision is selected during the simulation, the counterpart carrier is chosen at random from the ensemble. The internal rejection is performed by comparing a random number r between 0 and 1 with $2\beta g/(g^2+\beta^2)$. If the collision is accepted, the final state is then calculated as usual.

With respect to the previous method, the self-scattering algorithm for the carrier-carrier scattering does not require the tabulation of the scattering rates, which can be a strong limitation in terms of computer time and memory requirements. However, a large number of rejections occurs.

When an interparticle scattering is selected during the ensemble simulation, the k-vector of the second carrier involved in the binary collision can be taken at random from the ensemble. The selection of the final state $\mathbf{k}'_o$ of the simulated carrier is performed according to the prescription given earlier.

Two possibilities exist concerning the partner carrier involved in the collision. Since it has been selected from the ensemble, its state can be also changed to become $\mathbf{k}' = \mathbf{g}' + \mathbf{k}'_o$. In this way, the total energy would be conserved in the process. On the other hand, this would

force the second carrier to end its free flight at a time different from the one determined from its own scattering probability. To circumvent such a problem, the second electron state could be left unchanged. This procedure creates however another fault, as it introduces an artificial energy dissipation in the collision process.

An alternative method for the treatment of the electron-electron interaction has been proposed by Jacoboni (1976). It is based on a molecular dynamics simulation for the real-space trajectories of the ensemble of electrons interacting via a bare Coulomb potential, coupled to the usual EMC algorithm for the k-space dynamics.

The strength of the method lies in the fact that it does not require any assumptions on the screening between carriers. Furthermore, it naturally accounts for a fundamental component of a classical electron gas, namely the carrier density fluctuations. Applications of the molecular dynamics MC can be found in Lugli and Reggiani (1986), Lugli and Ferry (1986), Rota and Lugli (1989).

Degeneracy in Monte Carlo calculations

As shown in the previous sections, the Ensemble Monte Carlo method is a semiclassical technique, in that it simulates electrons as classical particles undergoing scattering events that are calculated according to the quantum mechanical transition probabilities. Classical statistics is used, and the Pauli exclusion principle is neglected. On the other hand, many of the situations of interest in semiconductor devices involve high concentrations of electrons, where degeneracy is expected to play an important role. In GaAs at 300K, this occurs for $n > 4.6 \times 10^{17} cm^{-3}$.

A powerful algorithm to include the Pauli exclusion principle in the MC technique has been proposed by Bosi and Jacoboni (1976) and extended to EMC by Lugli and Ferry (1985d).

The Pauli exclusion principle can be thought of as a many-body effect that influences

the transport properties of degenerate semiconductors by limiting the phase space available for electronic transitions. The probability of an electronic transition from a state $\mathbf{k}$ into a state $\mathbf{k}'$ is in general proportional to the probability $f(\mathbf{k})$ that the initial state is occupied and the probability $[1 - f(\mathbf{k}')]$ that the final state is unoccupied. Thus, the transition rate from $\mathbf{k}$ to $\mathbf{k}'$ is $S(\mathbf{k},\mathbf{k}') = P(\mathbf{k},\mathbf{k}')f(\mathbf{k})[1 - f(\mathbf{k}')]$, where $P(\mathbf{k},\mathbf{k}')$ is the scattering probability per unit time usually calculated from the Fermi golden rule. The standard MC procedure works within the approximation $f(\mathbf{k}') = 0$. That is, it considers all final states as being available. The latter method is only applicable to non-degenerate conditions, where the effect of the Pauli princile is negligible. The problem of working with the factor $[1 - f(k')]$ in the Monte Carlo algorithm lies in the fact that $f(\mathbf{k}')$ is not known *a priori*. However, with the EMC technique, the distribution function evolves with the ensemble and is known at every time.

The method of Bosi and Jacoboni, suggested for a one particle simulation, is based on the self-consistent iterative algorithm that resorts to the rejection technique to account for the occupation probability of the final state at each scattering event. At the time of the selection of the particular scattering process, the final state of the transition is still not known. The exclusion principle can at first be neglected for the determination of the lenght of the free flight, and for the choice of the scattering mechanism and of the final state. However, once the final state $\mathbf{k}'$ is selected, $f(\mathbf{k}')$ is, at least in principle, known from the simulation, and a random number between 0 and 1 can be used to accept or reject the transition. If $r > f(\mathbf{k}')$ the transition is accepted; if instead $r < f(\mathbf{k}')$, the scattering is treated as a self-scattering. This corresponds to the introduction of an auxiliary self-scattering mechanism with probability proportional to $[1 - f(\mathbf{k}')]$. This rejection procedure must be included since the factor $[1 - f(\mathbf{k}')]$ was ignore in earlier steps. As the procedure is iterated, a steady state will eventually be reached, with the probability of transitions into the state $\mathbf{k}'$ proportional to the occupancy of that state. In applying this procedure the normalization of the distribution

function must be carefully accounted for in such a way that the evaluated $f(\mathbf{k})$ represents the occupation number of the state $\mathbf{k}$. Such a normalization is to be performed by taking into account the number of states in the considered cell of k-space and the density of carriers in the physical system to be simulated.

The extension of the procudure to ensemble simulation is straightforward. In this case the distribution function is evaluated over the grid in k-space by countung the number of electrons in each cell. The distribution function so defined is then properly normalized as indicated above, taking also into account the number of particles in the ensemble.

When a scattering event occurs in the EMC simulation, the cell c containing the final state for the selected transition, is found. The normalized distribution f_c, corresponding to that cell, is compared with a number r randomly choosen between 0 and 1, and the scattering event is accepted or rejected as indicated above.

As it is always the case for an EMC simulation, the algorithm just described allows the analysis of the transient evolution of any given initial distribution to its steady-state.

3.9 Hot Phonon algorithm

We present here an Ensemble Monte Carlo algorithm for the study of non-equilibrium-phonon effects under hot electron conditions. This procedure allows us to follow the time evolution of the phonon distribution. A collection of results has already been presented in Lugli et al (1985,1987a,1987b,1988a,1988b) and Rieger et al. (1988,1989)

In the case of laser excitation, the photogeneration is reproduced by adding particles to the simulation, distributed in time according to the lineshape of the laser pulse, as shown in the insert of Fig. 3. The simulation is subdivided in time intervals Δt (with Δt typically much shorter than the average scattering time for the LO phonon scattering). At time $T = j\Delta t$, the number of Monte Carlo electrons is updated from the previous step according to the

expression :

$$N(T) = N(T - \Delta t) + C \ \Delta t \ cosh^{-1}(\omega_0 T), \tag{23}$$

where ω_0 and C are the parameters which model the width and power of the laser pulse.

Electrons are excited in the conduction band centered around a given energy E_{inj}, with a small broadening depending on the width of the laser pulse (typically around 20 meV). Since the excitation energies considered here are below the threshold for intervalley scattering (0.3 eV for Γ to L transitions), there is no significant transfer to the satellite valleys.

For the d.c.-field case, the number of simulated particles is fixed and the initial distibution is usually assumed to be Maxwellian.

The disturbances of other types of phonons are negligible in the situation examined here. The LO-phonon distribution function is followed in its time evolution, and phonon-induced modifications to the relaxation rates of the electrons are considered. In a finite difference scheme, Eq. (2) for the phonon evolution can be written in the form:

$$N_q(n\Delta t) = N_q\big((n-1)\Delta t\big) + \delta N_q(n\Delta t)\Big|_{ph-c} - \big(N_q(n\Delta t) - N_L\big)\frac{\Delta t}{\tau_{op}} \quad ; \quad n = 1,2,3... \tag{24}$$

The procedure set up to account for the LO-phonon disturbances has the following features:
i) the time evolution of the LO-phonon distribution N_q is calculated as a function of wavevector q from the MC simulation , by setting up a histogram h_q defined over a grid in q-space of mesh size Δq. After each scattering event involving an LO phonon, the histogram is updated. In the absence of external d.c. fields, because of the full spherical symmetry only the amplitude of q is relevant, thus reducing the complexity and the storage requirements of the simulation. A detailed analysis of such a situation (Rieger et al. 1987) will be given in the last section

ii) At fixed times T = jΔt during the simulation , N_q is calculated as

$$N_q(j\Delta t) = \tilde{N}_q(j\Delta t) + |\tilde{N}_q(j\Delta t) - N_L|\frac{\Delta t}{\tau_{op}}, \tag{25}$$

where

$$\tilde{N}_q(j\Delta t) = N_q((j-1)\Delta t) + A\Delta h_q . \tag{26}$$

The term A Δh_q gives the dynamical contribution of the electronic processes to the phonon distribution during the time step Δt. Here, Δh_q is the contribution of the c-ph processes to the histogram, and A is a normalization factor accounting for the density of states in q -space and for the concentration of excited electrons, given (for the spherically symmetric case) by

$$A = \frac{2\pi^2}{q^2 \Delta q}\frac{n_0}{N}, \tag{27}$$

where n_0 is the electron concentration and N the number of simulated particles.

The second term on the right hand side of Eq. (7) accounts for phonon decays during Δt due to phonon-phonon processes. The algorithm for the phonon counting can be viewed as a hybrid MC solution of the phonon Boltzmann equation within a finite difference scheme.
iii) to account for the modifications induced by the phonon disturbance on the rate of electron-phonon scatterings, the integrated scattering probabilities for LO-phonons are calculated and tabulated at the beginning of the simulation using an artificially high value N_{max} for the phonon distribution. The choice of the final state of each scattering process involving an LO phonon is made using a rejection technique which compares the actual value of the differential scattering rate with the maximized one. In this way, we are able to discriminate between the scatterings that can be attributed to the enhanced phonon distribution versus those induced by the initial maximization (which are treated as self-scatterings in the simulation). A schematic plot of the rejection technique is presented in Fig. 2. In order to reduce the number of self scattering events , it is possible to recalculate the scattering rates at fixed times during the simulation. A numerical integration over the perturbed phonon distribution

function gives the exact scattering rates at a given time, which can be used directly on the simulation.

The suggested procedure is a full MC simulation of the dynamics of an interacting electron-phonon gas within the finite difference scheme indicated above, free of adjustable parameters. In the next section, the results of the MC simulation in the presence of laser excitation will be presented. The application of the algorithm in the presence of an applied electric field will be presented in Sect. 6.

4. Simple Case: Excitation from a single valence-band level

4.1 Bulk GaAs

A two-valley (Γ and L) model is used for GaAs (under the conditions considered here X valleys do not contribute significantly). The following scattering mechanisms are considered:

- deformation potential coupling to acoustic phonons ($D_{ac} = 7eV$), treated exactly according to the procedure given in (Jacoboni and Reggiani, 1983);
- unscreened polar optical coupling to LO phonons;
- unscreened scattering from ionized impurities, treated in the Conwell-Weisskopf formalism. Throughout the present section, nominally undoped materials (with a residual impurity concentration of $10^{14}\ cm^{-3}$) will be considered,
- deformation potential coupling to intervalley $\Gamma \rightarrow L$ phonons ($D_{iv} = 8\text{x}10^{8} eV/cm$),
- electron-electron scattering between Γ-valley electrons, which has been included using the algorithm described earlier (Lugli and Ferry 1983,1985a).

The algorithm described in the previous section has been applied to various situations to study the dynamics of the LO phonon, of the electron distributions, and their mutual effects. The time evolution of the perturbed phonon distribution is shown in Fig. 3 for an excited carrier density of $5\text{x}10^{16}\ cm^{-3}$. Electrons are excited at an energy of 0.25 eV above the bottom of the conduction band, corresponding to a photon energy of 1.8 eV. The lattice temperature is 77 K. The lineshape of the laser pulse is shown in the insert (halfwidth = 0.8 ps). The LO distribution is driven out of equilibrium even during the excitation, due to the fast power dissipation of the high-energy photoexcited electrons. The maximum is reached at a delay time of 1 ps for wavevectors of about $6\text{x}10^{5}\ cm^{-1}$. The small q values that are amplified during and immediately after the excitation are due to the polar nature of the electron-phonon coupling. At longer times, the phonon distribution relaxes

towards its equilibrium value as a result of two distinct processes, phonon reabsorption and phonon-phonon interaction. The first one is due to the fact that the group velocity of optical phonons is very small (less than $10^3 cm/s$), implying that the phonons cannot drift away of the excitation volume during their lifetime. Therefore, if the phonon lifetime is long enough and the coupling with the carriers sufficiently strong, emitted phonons can be reabsorbed.

It is important to notice that modes of different wavevector evolve in time in different ways, as indicated in Fig. 4. Those with the smaller q ($6x10^5\ cm^{-1}$) exhibit an exponential decay, immediately after the end of the excitation, with a characteristic decay time of 7 ps. At intermediate q's (8 and $10x10^5\ cm^{-1}$) the phonon distribution decay much faster at short times (up to 5 and 8 ps delay), approaching then the exponential behavior. The amplification of these large-q phonons is not as pronounced as that of the small-q ones.

The time evolution of the phonon distribution reflects the microscopic details of the cooling processes in the coupled electron-phonon system. While phonon-phonon processes are always active, and their effect is independent of wavevector, phonon reabsorption varies drastically as a function of time and wavevector. In fact, the very rapid changes in the electron distribution function (that will be examined below) modify the range of phonon transitions that are allowed by energy and momentum conservation. Figure 5 shows the minimum q for LO-phonon absorption and emission as a function of electron energy in a parabolic band. At high energy, electrons can emit phonons with very small q, but as they cool the minimum allowed q shifts to higher values. Such a shift appears in Fig. 3, hidden though by the strong initial amplification. Furthermore, an electron will not be able to reabsorb the earlier emitted phonons once it goes below a certain energy.

This simple analysis explains why the phonons with small q-vector excited during the first stages of the electron relaxation (up to 2 ps delay time) cannot be reabsorbed, and decay exponentially via nonelectronic phonon-phonon processes. On the other side, both the

reabsorption and the phonon-phonon terms will contribute to the damping of phonons of larger wavevector in the first few picoseconds, leading to their faster decay over this time interval.

The modification of the scattering rates for the electron-LO phonon interaction due to the phonon perturbation is presented in Fig. 6. There the total scattering rates for absorption and emission, obtained from a numerical integration over the perturbed distribution function N_q, are plotted at different time delays after the end of the laser pulse. Since at low temperature the value of the equilibrium phonon distribution is much smaller than unity, the emission probability is a few orders of magnitude higher than the absorption one. As the phonon population grows out of equilibrium, the absorption rate increases dramatically, relatively much faster than the emission one. The changes of the scattering rate with time reflect the temporal evolution of the phonon population. It is important to notice that even a few picoseconds after the pulse, a significant amount of phonons are still present and a considerable number of phonon reabsorptions are detected.

The time evolution of the electron distribution function, shown in Fig. 7, completes the previous analysis of the phonon amplification. The distinct peaks in the distributions at short time delays (0 and 1 ps) are due mainly to LO phonon emission which sets in already during the laser pulse (an average time of 160 fs for the emission of an LO phonon by electrons at the excitation energy is calculated from the simulation). At a time delay of 4 ps, the electrons mainly populate the low energy region below 100 meV. Many of them have an energy below the threshold for LO phonon emission. It will be seen later that in this case reabsorption can become very important.

As a last remark on the phonon dynamics, it is important to compare the previous considerations with the experimental results of Raman spectroscopy. The shaded area in Fig. 5 indicates the range of Raman-active wavevectors for the data given in Collins and Yu

(1984) and in Kash J. et al. (1985). The MC result for those modes (curve ⊔ in Fig. 4) is in good qualitative agreement with the findings of Kash J. et al. (1985), obtained for the same electron concentration but a higher excitation energy.

The effect of the phonon perturbation on the cooling of the photoexcited electrons is shown in Fig. 8. The electron relaxation rate is drastically reduced because of the presence of non-equilibrium phonons. The phenomenon is mainly due to the reabsorption of the LO phonons that have been emitted in the first stage of the relaxation without having had enough time to decay. The effect of phonon reabsorption grows with time as the electrons populate the low energy regions below the threshold for optical emission. Furthermore, the reduction in the cooling rate of the electrons is even larger at higher electron densities or higher injection levels, as found both experimentally (Kash K. et al. 1985; Leo et al. 1988; Ryan et al. 1988) as well as in our simulation.

The MC algorithm presented here has been compared with the models of Pötz and Kocevar (1983) and Collet and Amand (1986). At the low excitation energies used in Collet and Amand (1986), the phonon disturbance is reduced with respect to the case shown in Fig. 3, and reaches its maximum at higher q's. The result of the simulation obtained with an electron density of $10^{16} cm^{-3}$ and an 80 fs laser pulse with an initial electron energy of 80 meV is shown in Fig. 9. The MC result agrees quite well with that of the more sophisticated model of Collet and Amand (1986).

The temperature model of Pötz and Kocevar (1983) assumes that the carriers (electrons and holes) are characterized by a Fermi-Dirac distribution at any time during and after the laser pulse, corresponding to a very fast thermalization within the photogenerated plasma. In order to verify the consistency of our results, we have performed a simulation by assuming that the carriers are initially distributed according to a heated maxwellian distribution. The MC results, obtained using the same parameters as in the calculation of Fig. 3, indicate in

this case a much smaller phonon perturbation, with the maximum of the phonon distribution still reached at 1 ps delay time as in Fig. 3, but its value being reduced by a factor two. The reduction of phonon heating is related to the population of the low-energy region of the maxwellian distribution as compared to the sharp distribution at the excitation energy. The MC results agree very well with those we obtained from a temperature model for a one-component plasma. When both electrons and holes are considered, the temperature model, assuming the same temperature for both carriers, implies an inherent instantaneous energy transfer from the electrons to the holes and thereby a further reduction of the phonon heating by electrons. Although the latter result depends heavily on the assumptions of the single-temperature model, it nevertheless shows that the electron-hole interaction can be very important. A preliminary step to combine the effect of electron-hole scattering and non equilibrium phonons has been recently presented both for a two-temperature model (Pötz 1987) and a MC analysis (Osman et al. 1987).

Up to now we restricted our discussion to cases where only the central valley is important. In general, especially if the excitation energy is sufficiently high, the population of the higher valleys (L and X) is not negligible. For such cases the influence of the satellite valleys on the phonon disturbances can be very strong. Figure 10 shows the minimum q for LO-phonon absorption and emission as a function of electron energy for the Γ (same curve as Fig. 5) and the L valleys. Due to the higher effective mass of the latter valleys, the emitted LO phonons have a larger wavevector. Because of the increased area of phase-space, the contribution of the L-electrons to the phonon distribution function will be reduced. This is illustrated in Fig. 11, where an initial electron energy of 0.5 eV has been used (with a $\Gamma - L$ separation of 0.3 eV). The parameters of the simulation are the same as before. One picosecond after the excitation, about 60 percent of the electrons are found in the L valley. The MC histogram (Fig. 11a) confirms that the emission of LO phonons by L-valley electrons is

concentrated in the large-q region. The actual number of phonons reflects indeed the relative population of the two valleys. Nevertheless, the effect of those phonons on the perturbed distibution (Fig. 11b) is negligible. Furthermore, all of the L-valley phonon have q values too large to be detected spectroscopically. We can therefore expect that phonon amplifications experimentally detected would decrease in the presence of substantial intervalley transfer. We are assuming here that the four ellipsoidal valleys can be represented by an equivalent spherical valley with an average effective mass, although a study of the effect of the valley anisotropy is needed.

4.2 GaAs-AlGaAs Quantum Wells

Recent results obtained with time resolved photoluminescence have shown dramatically reduced energy relaxation rates for photo-excited electrons in GaAs-AlGaAs quantum wells (Ryan et al. 1986; Xu and Tang 1984). After some controversy whether the slow cooling rates are due to the effect of non-equilibrium phonons (Lugli and Goodnick 1987; Leo et al. 1988; Das Sarma et al. 1988; Shah et al. 1985), of screening (Yang et al. 1986; Das Sarma et al. 1987) or of some combined action of these mechanisms, hot phonons are now recognized as the main cause. The algorithm just presented has been applied to a single quantum well of GaAs-AlGaAs (150 $\AA$ wide and 0.28 eV deep), with subband energies given by the solution of the one dimensional wave equation for a square well potential. The bands are assumed to be parabolic. The scattering rates (both intra- and intersubband) of the quantized 2D electrons with bulk unscreened LO-phonons are calculated numerically without the use of momentum-conserving approximations (Riddoch and Ridley, 1983). It has been shown there that, for wells larger than 100 $\AA$, there is little difference between the scattering rates calculated accounting for phonon confinement (slab modes) and the one obtained using bulk modes. Intervalley transfer to the L-valleys (also quantized) is included as well. The

mechanism of 2D electron-electron scattering is introduced in the MC simulation through a generalization of the self-scattering technique described above (Brunetti et al. 1985) to the multi-subband quantized system (Goodnick and Lugli 1987,1988a). The various electrons are allowed to interact via a statically screened Coulomb interaction determined by the long wavelength limit of the two-dimensional Lindhard dielectric function. Degeneracy effects due to the Pauli exclusion principle are also considered. In the present simulation we have neglected electron-hole scattering and recombination, which might be of importance in some of the reported experiments.

In 2D, the component of the phonon wavevector in the direction of the well, q_z, is not conserved due to the spatial localization of the electrons there. In fact, the emitted phonons are spatially localized which causes problems as to their representation in terms of plane waves as was noted by Price (1981). This problem has been more recently addressed by Cai et al. (1988) who solve the coupled 2D electron-phonon kinetic equations considering off diagonal contributions of the phonon density matrix. In our model we considered a simpler approach, that is that the q_z components of the phonon distribution are localized in a region of wavevector space of extent 1/L, L being the width of the well. This choice is indicated by the probability amplitude for emission and absorption obtained from the 2D-electron-phonon scattering matrix element which has been shown to be a sinc function of width 1/L (Riddoch and Ridley 1983). We approximate this function by a flat distribution over the range 1/L. For intra-subband transitions, this function is centered around $q_z = 0$, whereas for inter-subband transitions, the sinc function is centered around a non-zero momentum related to the change in subband energy. Therefore, the phonon distribution is tabulated for discrete q_z corresponding to the varius inter- and intra-subband events, with the phonon wavevectors otherwise treated as two-dimensional. These assumptions are relaxed when slab modes are considered explicitely, as it will be indicated in the next paragraph.

The cooling of photoexcited electrons in an n-type GaAs-AlGaAs quantum well at low temperature (5 K) has been considered (Lugli and Goodnick 1987; Goodnick and Lugli 1988a). A background sheet density of 2.5×10^{11} cm^{-2} is used. The injected sheet density is 5×10^{11} cm^{-2} The GaAs parameters are the same as for the bulk case. The width of the simulated laser pulse is about 1 ps, during which time carriers are added to the simulation with an initial energy of 0.25 eV above the bottom of the lowest subband. The insert in Fig. 12 shows the position of the energy levels in the well. Figure 12 shows the evolution of the electron total energy (kinetic plus potential) as a function of time during and after the pulse. The excited electrons lose energy mainly through the interaction with the background electrons and through the emission of LO phonons. For equilibrium phonons ($\Box$), the hot electrons are found to reach equilibrium in about 3 ps. In contrast with the case of an unperturbed phonon distribution, a much slower relaxation is found when non-equilibrium phonons are accounted for (o , $\triangle$). The two cases in Fig. 12 correspond to different injection densities. At the excitation energy considered here, virtually no intervalley transfer occurs. It is worth noticing that no real dependence on well width has been found in the MC results. The reduction of the electron cooling rate is due to the reabsorption of non-equilibrium phonons which build up during the initial pumping and the first stage of the electron relaxation. This is evidenced by the time evolution of the phonon distribution at q_z=0 (intra-subband scattering) shown in Fig. 13. The same, although reduced, features are found also at $q_z \neq 0$. LO-phonon emission during the pulse and immediately after creates a large population of phonons at small q's. At longer times, phonon reabsorptions and phonon-phonon losses drive the distribution back to equilibrium. The secondary peak that develops at later times in the phonon distribution is due to phonon emission by electrons that have already relaxed to lower energy. As pointed out before, the reduction in the electron relaxation rate is mainly due to reabsorption of the emitted LO-phonons. The effect is stronger when a considerable number

of electrons have relaxed to the low energy region below the emission threshold.

Recently, a time resolved Raman analysis of the development of non-equilibrium LO phonons in narrow AlGaAs-GaAs quantum wells was presented (Tsen et al. 1988). There electrons were excited in the first subband with an excess energy of about 160 meV. From the anti-Stokes peak of the Raman signal it was possible to monitor the build up of the non-equilibrium LO-phonon population. For an experiment performed in back scattering geometry in a two dimensional system, the output (that is the LO phonon population) constitutes an average over all LO modes, contrary to the bulk case where a well defined region of q-space is analyzed. The experimental results (extracted from the time-resolved average of the anti-Stokes peak) indicates an "average" phonon lifetime of 8 ps at 10 K. The MC results for the same situation are shown in Fig. 14 for three different values of τ_{op}.

It is clear that reabsorption plays a very important role in the experiment. The more strongly amplified phonons (around $q \simeq 8 \times 10^6$ cm^{-1}) decay with a time constant which is much shorter than the ph-ph value introduced in the simulation. As pointed out in the discussion for the bulk case, this indicates a strong contribution of the electronic processes to the phonon lifetime. Therefore, even if it is hard to extract an average phonon lifetime from the results of Fig. 14, this seems to indicate that the measured phonon lifetime is not directly the nonelectronic ph-ph lifetime, but sets a lower limit for it.

Slab modes

So far, the standard three dimensional dispersion for the LO phonons has been used. Recently, a lot of activity has been directed to the study of the vibrational properties of QW's and superlattices (two excellent reviews on the subject can be found in Jusserand and Cardona, 1989, and Menendez, 1989). Most of the theoretical and experimental work has centered on the physics of phonons in such systems, without focusing on its implications

on carrier transport. On the other side, the transport community has so far neglected all the features connected to phonon confinement (except for some isolated attempts, such as Riddoch and Ridley 1985; Sawaki 1986; Babiker et al. 1987), relying on the well established bulk-phonon picture. While such approximation is justifiable for large QW's (well width of 10nm or more), a more creative and rigorous approach is needed for narrower wells.

It is well established that optical modes are localized in each layer of superalttices and QW's, with a small degree of penetration into adjacent layers depending on the properties of the interaface. Macroscopic models have been used to study the lattice dynamics of QW's and superlattices. On the basis of a dielectric continuum model, Fuchs and Kliever (1965) have analized the vibrational properties of ionic slabs. By treating the LO modes as consisting only of electrostatic fields, the solution of Laplace equation leads to two sets of modes, guided modes whose associated displacement is represented by sine and cosine functions, and surface modes, with displacement given by sinh and cosh functions. The standard electrostatic boundary conditions imposed on the field lead to a zero value of the potential at the boundaries, with the transverse displacement in anitiphase with respect to the potential. Such formalism has been used by Riddoch and Ridley (1985) to determine the scattering rates and by Jain and Das Sarma (1988) to calculate the energy loss rate due to polar optical scattering in QW's. Recently it has been pointed out (Cardona 1988) that mechanical boundary conditions must also be taken into consideration, by imposing phonon confinenemt via a zero dispacement at the boundaries. Accordingly, since the mechanical displacement is proportional to the electrical polarization, the potential is bound to have a maximum at the interface. Furthermore, because of the zero diplacement condition, no surface modes are allowed. Such conclusion is somewhat analogous to the results of Babiker (1986) based on a dispersive continuum model, and of microscopic models (Huang and Zhu 1989). The incompatibility of the two boundary conditions, and the consequent opposite symmetry

of the displacements and potentials have originated some controversy (Ridley 1989). It has recently been shown (Huang and Zsu 1989; Menendez 1989) that no controversy actaully exists, and that the proper account of the surface modes leads to a good agreement between Fuchs and Kiever model and microscopic calculations. The key point is that the interface modes of the dielectric continuum model (which for $k = 0$ become bulk-like vibrations) correspond to the first confined mode of the microscopic model. Once the "interface" mode are included in the picture, the symmetry of the successive confined modes coincides in the two models. The following results will be based on Fuchs and Kliever model.

The total scattering rate for electrons in the first subband of a 150 A QW due to guided modes (dashed line) and to surface modes (dotted line) at 10 K is compared with the bulk three-dimensional rate in Fig. 15. Under these circumstances the contribution of the surface modes is negligible. Such scattering rates are used for a MC simulation of the relaxation of a photoexcitec plasma. In this case electron-electron, hole-hole as well as electron-hole scatterings are accounted for (Goodnick and Lugli 1988b). A background electron density of $7 \times 10^{11} cm^{-2}$ is considered, while the excited plasma density is $3 \times 10^{11} cm^{-2}$. Electrons are injected with an excess energy of 200 meV at a lattice temperature of 10 K. Figures 16 and 17 show respectively the average electron and hole energy (in K degree) as a function of time. The three curves correspond to different values of the phonon lifetime τ, respectively 0 ps (i.e. unperturbed phonons, continous curve), 7 ps (dashed curve) and 25 ps (dotted curve). The different behaviour is attributed to the hot-phonon effect descrideb earlier. When phonons are kept in thermal equilibrium carriers exhibit a faster decay; the rate at which the cooling process takes place depends on the phonon lifetime, since the phonon reabsorption is directly proportional to N_q. Hole present the same type of behavoiur, with the reduced cooling associated mainly to the presence of nonequilibrium LO phonons. TO phonons are only slightly perturbed, mainly because of the large portion of q-space that the emitted phonons

fill up.

The phonon distribution of the three lowest guided mode at 1 *ps* time delay is shown in Fig. 18. Here, a phonon lifetime of 7 *ps* is assumed. The strongest amplification is found for the $m = 1$ mode, which, because of its parity, reflects mainly the contribution of intrasubband transistions. The non-equilibrium distribution for the first guided mode is plotted at three diffrent time delays in Fig. 19. The highest perturbation is found immedialtely after the excitation, very pronounced at small q's, indicating a major contribution from the photoexcited electrons. Holes contribute less to the heating of the slab modes, because of the eavier mass (which implies a larger q of the emitted phonons), the reduced excess energy, and the strong coupling to the TO phonons. The phonon perturbation is smaller than the one found in the previous section, since the intercarrier scattering constitues now the main channel for energy dissipation from the photoexcited plasma to the large background electron bath.

5. Realistic Model: Excitation from a three-valence band model

When the details of the band structure are taken into account for the photoexcitation process, a more elaborate description of the initial carrier distribution is necessary. As illustrated in Fig. 20 for bulk GaAs, the absorption of photons with considerable energy (typically around 2 eV) induces transitions from the three hole bands. Therefore, the energy distribution of the photoexcited electrons is characterized by three distinct peaks, slightly broadened because of the warping of the valence band and of the natural absorption linewidth. This condition enters as the initial condition (for the electron energy distribution function) in the MC program described earlier). The present MC algorithm has been used to analize the luminenescence spectra after photoexcitation with a 400 fs wide laser pulse at T_L=300 K (Shah et al. 1987) (see below). The physical parameters used in the simulation are shown in Tab. 1. Figure 21 shows the MC electron distribution at three different time delays in bulk

InP and GaAs. Some important differences are worth noticing. In GaAs, around 60% of the photoexcited carriers transfer to the satellite valleys during the laser pulse (the average time for $\Gamma \rightarrow$L transition via phonon emission or absorption is around 80 fs). This creates the depletion in the high-energy region, above 0.3 eV, noticeable in Fig. 21. Carriers return slowly to the Γ valley, with a characteristic time of 2 or 3 ps. The net $\Gamma \rightarrow$ L transfer is actually a complicated series of processes where electrons can scatter in and out of the L valleys before leaving the actively-coupled energy region (that is the range of energy above 0.27 eV). The L valleys in InP sit at a much higher energy, and do not significantly contribute to the cooling process. The electron distribution is smoother than in GaAs, and the population of the low-energy region is higher at all times, since the cooling process is not slowed down by intervalley transfer. In both cases, electrons are characterized at the shortest time (1 ps) by an athermal distribution. Even if the intercarrier scattering is not sufficiently strong, at the low densities considered here ($5 \times 10^{16} cm^{-3}$), to assure complete thermalization within the ensemble, it is nevertheless sufficient to smooth out the initially peaked distribution. This indicates the inadequacy even at the shortest times of the cascade model (Kash J. et al 1985).

A direct comparison with experiments requires the calculation of luimescence spectra, which is directly proportional to the product of the electron and hole distribution functions. By assuming that the holes relax to a thermal equilibrium at the lattice temperature within the laser pulse, it is possible to extract the spectra directly from the electron distribution functions shown in Fig. 21. The results are presented in Fig. 22 where spectra obtained for GaAs from the simulation at three different delays are compared to the experimental ones. The agreement is indeed extremely good. The most remarkable aspect of the data is that the luminescence intensity near the bandgap energy (as well as the integrated luminescence) show a significant increase for nearly 10 ps after the end of the excitation pulse. This is clearly shown from the luminescence intensity as a function of time in Fig. 23, where for comparison

the InP result is also shown. Once again the agreement between theory and experiment is excellent. For GaAs, this indicates for the $\Gamma - L$ deformation potential $D_{\Gamma L}$ a value of of $6.5 \pm 1.5 \times 10^8$ eV/cm.

The time behaviour of the electron average energy for InP and GaAs is presented in Fig. 24 for three different carrier concentrations. The density dependence of the results is due to hot phonon effects as described earlier. Clearly, other processes such as electron-hole scattering or free-carrier screening of the polar optical phonon coupling can have an influence on the carrier relaxation, especially at the highest carrier densities. However, screening has repeatedly been demonstrated to play a minor role in the presence of strong LO-phonon amplification (Pötz and Kocevar 1983; Kocevar 1987). At room temperature, the reduction of the cooling rate is not very pronounced, especially in GaAs, because of the large availability of LO phonons that limits the effectiveness of the reabsorption processes. The time behaviour of the average energy indicates a very rapid cooling of the photoexcited electrons in InP, due to the confinement of electrons in the Γ valley and to the stronger polar coupling of this material. Because of the high density of Γ electrons, the hot phonon effects noticeable in the first picoseconds after the excitation are stronger than in GaAs.

The characteristic behaviour of the two materials also shows up in the non-equilibrium LO phonon distributions shown in Fig. 25. A stronger and faster phonon build up is found in InP, with the maximum amplification reached at time delay of 1 ps. The time evolution of the Raman-active modes ($q_R \simeq 8 \times 10^5 \ \ cm^{-1}$) for GaAs is shown in Fig. 26. For the room temperature case (open circles) a plateau is observed in the first picoseconds after excitation, which is a direct evidence of the slow return of the electrons from the upper valleys. Such features are related to the fact that, within the spherical model for the upper valleys, phonons are emitted there with wavevectors outside the Raman-active area. Therefore, the contribution to the phonon amplification at q_R follows closely the loss of population of the

upper valleys. The comparison of the time behaviour of the phonon modes at two different temperatures is also presented in Fig. 26. After the initial delay, the populations decay with characteristic times of around 3.5 and 7 ps at 77 and 300 K respectively, in agreement with the experimental results (see insert).

A crucial point in the analysis of the experimental data and the comparison with theory concerns the determination of the effective temperature of the carriers. The effective temperature of the Γ-valley electrons (which for a thermal distribution is given by the slope of the energy distribution function) is usually extracted from the tail of the luminescence spectra as those shown in Fig. 22. It is important to notice that only the low-energy portion of the distribution function shown in Fig. 21 (below 0.2 eV) contributes to those spectra. In order to check how the effective temperature obtained from the slope of the energy distribution is representative of the electron average energy (shown in Fig. 5) of the central valley electron population, we have plotted in Fig 27 the electron distribution function in the range 0-0.2 eV for three different excitation densities in GaAs, and for the lowest density in InP. The effective temperature deduced from the slope of the curves (solid lines) are indicated. Clearly, within the first picosecond after excitation, the distribution function is not maxwellian, and the definition of an effective temperature is questionable. In fact, the effective temperatures deduced from the distribution function are always lower, expecially at very short times, than the average energies calculated from the MC simulation.

As a last point, we would like to comment on a previous determination of $D_{\Gamma L}$ for GaAs obtained from Raman data. In the experiment of Collins and Yu (1984), a value of $D_{\Gamma L}$ equal to 1.5×10^9 eV/cm was derived from the time evolution of the anti-Stokes peak for a much lower excitation density and a much longer laser pulse, compared to the situations examined above. The data were interpreted as indicating very little transfer of photoexcited carriers into the satellite valleys despite the very high excitation energy. Our MC simulation

of that experiment shows that the non-equilibrium phonon population is not very sensitive to the $\Gamma - L$ coupling, as shown in Fig. 28, mainly because of the long times and small densities involved. Figure 29 illustrates this point, by comparing the time evolution of the phonon disturbance (at q=$8 \times 10^5\ cm^{-1}$) obtained from the MC simulation with two values of $D_{\Gamma L}$ equal respectively to 1.5 and $7 \times 10^8\ eV/cm$. When the $\Gamma - L$ coupling is weak, the transfer of photoexcited electrons to the satelite valleys is drastically reduced. Therefore, a stronger phonon amplification is found at the shortest times, compared with the case ($D_{\gamma L} = 7 \times 10^8\ eV/cm$) when the intervalley transfer is dominant.

As it was shown by Shah et al. (1987), the MC analysis of time-resolved photoluminescence data indicates that a value of $D_{\Gamma L} = 1.5 \times 10^8\ eV/cm$ is far too low to interpret the experimental results, while an excellent agreement is found for $D_{\Gamma L} = 6.5(\pm 1.5) \times 10^8\ eV/cm$. If the experiment could be repeated under more favourable conditions (that is with a much shorter laser pulse and a higher density), the phonon distribution could be used to discriminate between different values of $D_{\Gamma L}$.

6. Field-dependent case

In the present section we will study the effect of non equilibrium polar optical phonons driven by an external electric field (Rieger et al. 1988,1989). We use a slightly different physical model than in the previous section. Static screening of the LO phonon interaction has been considered, and impurity scattering is treated in the Brooks-Herring formalism.

In this case, the LO phonon distribution has been collected on a two dimensional grid. Because of the small q involved in the polar optical scattering, the phonon amplification is strongest in the field direction. In order to allow a better comparison of our results with earlier work for phonon equlibrium, the material parameters have been taken here from the standard d.c. MC study of GaAs of Littlejohn et al. (1977). As for the previous sections,

acoustic-phonon disturbances are negligible at the high temperatures of the present study. The intervalley phonons are also assumed to be in equilibrium, since their disturbance is partitioned over large regions of q-space (Kim et al. , 1988). A range of electron and impurity concentrations from 10^{16} up to $10^{19} cm^{-3}$ is considered. Lower densities would in fact display negligible phonon disturbances, while at higher densities the electron mobility will be totally dominated by impurity scattering and hot phonon effects will vanish. As a particular interest for future device applications in quantum wells, a simulation has also been performed with a high carrier density in the presence of a negligible impurity concentation, so to reproduce the modulation-doping case.

6.1 Single-Valley Effects

In order to sudy the consequences of purturbed LO phonons on the mobility and average energy of Γ-valley electrons, the electric fields are kept below the threshold for noticable intervalley transfer. Figures 30, 31 and 32 show the results obtained for a field of $2kV/cm$, an electron and impurity concentrations of $3 \times 10^{17} cm^{-3}$, at 300 K. The first two figures diplay a comparison between the time evolution of the average drift velocity (Fig. 30) and average energy (Fig. 31) as obtained for phonon equilibrium ($r_0 = 0$, full lines) and disturbed phonons ($r_0 = 9ps$, dashed lines) respectively. The major effect of the phonon disturbances is a significant increase in v and E_Γ, showing the drag of the carriers by the most strongly amplified phonons and the reduced cooling of the carriers by hot phonons.

The time evolution of the forward distribution $N(q, cos\theta = -1)$ is separately shown in Fig. 32. The distribution, which exhibits its strongest amplification in this forward direction, approaches a steady-state value of 1.4, a substantial increase over the thermal equilibrium value of 0.34. The magnitude of the wavector corresponding to the maximum phonon amplification decreases with time, following the increase of E_Γ and the concomitant

population of higher energy regions. In this way a prononced low-q peak develops, down to a minimum value set by energy and momentum conservation requirement and by the static free-carrier screening of the polar optical coupling. Expecially at high fields such low-q peak is accentuated by the accumulation of Γ valley electrons at energies just below the valley transfer threshold.

It is important to correlate the q-space analysis of the amplified phonons with the information about the carrier distribution function $f(E)$ that can be extracted from the simulation. In contrast to the thermal equilibrium case, with equal rates for phonon emission and absorption, the presence of a d.c. field causes a relative increase of emissions over absorptions, to provide the net flow of energy from the external field through the carrier system into the lattice. In the presence of phonon disturbances, the statistical factors for induced emission and absorption processes increases in the same proportion N_q/N_L. Therefore, no change in the net energy transfer can be expected from the increased phonon occupancy alone. However, the resulting relative increase for the absorption rate is higher whenever the occupation probability $N(E) \propto e^{\frac{1}{2}} f(E)$ peaks below the threshold for LO phonon emission and near the favorable reabsorption range (see discussion of Fig. 5). In this way the relative statistical weight for absorptions is enhanced and the difference between emission and absorption rates reduced. Carrier are therefore "hotter"than in the case of phonon equilibrium. The simulated Γ-valley occupations are plotted for two different times in Fig. 33. Indeed most of the electrons are found at energies below the LO-phonon emission threshold, as required for marked phonon-reabsorption effects.

An interesting effect is connected to the interplay between ionized impurity (i-i) scattering and phonon reabsorption. Due to the higher electron average energy, a quite pronounced decrease of the screening parameter q_D is found during the phonon build up, which outweights the reduced efficiency one would find for the unscreened i-i scattering. As a result, a slight

increase of the number of i-i scattering and of the i-i momentum dissipation rate is detected in the simulation.

A related questions concern the influence of the screening model. Figures 34 and 35 swoh the results obtained for Debye-screened and unscreened polar optical coupling at 77 K. They confirm the old finding of the carrier-temperature models (Kocevar 1985) that screening plays a negligible role in the presence of strong phonon disturbances. As the use of static screening correspond to the assumption of the maximum possible scrrening efficiency of the free carriers, any more detailed dynamical screening model would give intramediate results between the two limiting case of statically screened and unscreened coupling. The only exception would be the case of antiscreening (Doniach,1959) where the results can be expected to extrapolate beyond the unscreened limit, but again with negligible effects on the average velocity.

6.2 Many-valley effects and velocity overshoot

At high electric fields, a substantial fraction of electrons scatters into the satelite valleys. Figure 36 shows the time evolution of the Γ-valley relative concentration (dashed and full lines) and average energy (dotted and dashed-dotted lines), with and without phonon disturbances, for an electric field of 8 kV/cm turned on at $t = 0$. The high field causes a sufficient heating of the Γ electrons to allow a very rapid onset of intervalley scattering, leading to a decrease of the Γ-valley mobility and a substantial transfer. The consequences of such transfer on the average total velocity and on the energy of the L-valley elecrons are shown in Fig. 37. No effect of the LO phonon disturbance on the velocity overshoot is detected, which is somewhat astonishing after the strong phonon-induced heating of the Γ-valley electrons found in the previous section. It is again of help to follow the time evolution of the LO-phonon disturbance and of the carrier occupation. Figure 38 shows the forward phonon distribution at three different times, corresponding to the velocity peak ($t = 0.5ps$), to the

maximum amplification of the electronically active modes ($t = 1.3ps$), and to the onset of the steady state ($t = 20ps$). The error bar indicate the statistical fluctuation connected to the choice of the discretization of q-space. In spite of the strong and rapid phonon amplification, the average energy of the Γ-valley electrons is still the same as for the unperturbed case. Therefore, the Γ valley population and the velocity overshoot remain practically unchanged.

While the phonon-excitation spectrum at $t = 0.5ps$ is very similar to the steady-state one of the previous section, the carrier occupation in the Γ valley is now much broader, peaking near the threshold for intervalley transfer and leaving only a small fraction of electrons to the dominant net-reabsorption region below the optical phonon energy. As a consequence, phonon reabsorption for Γ-valley electrons is strongly rediced with respect to the low field case, explaining the failure of the LO-phonon disturbance to intefere with the transfer to the upper valleys.

The decisive difference between low and high field cases is shown in Fig. 39, which shows the steady state carrier occupation at two different electric fields. At $2kV/cm$, a noticeable depletion of the low energy and corresponding enhancement of the high energy regions is induced by the phonon reabsorption. The average electron energy moves from 55 meV to $68meV$ when phonon disturbances are considered. At $8kV/cm$ the two distributions are practically identical within the statistical fluctuation in spite of the very strong phonon amplification shown in Fig. 38. A separate analysis of the average velocity of Γ and L valley electrons reveals very small nonequilibrium effects on v_L and a noticable effect on v_Γ. In contrast to the low-field case, however v_Γ is reduced. This change from a dominant phonon-drag effect at low fields to a frictional hot-phonon effect at high field cinfirms the finding of the temperature model.

The velocity-field curve for GaAs at 300 K is shown in Fig. 40 for two condition corresponding respectively to equilibrium (continuous curves) and perturbed phonons (dashed

curves). One set of curves refers to the case of uncompensated material with the electron concentration equal to the impurity concentration. The other situation is tipical of the remote impurity scattering characteristic of modulation doped structures, where the mobile carriers are spatially separated from the impurities they have been generated from. At low fields, below the threshold for intervalley transfer, the Γ electrons are dragged by the forward streaming phonons. As a result, the drift velocity increases. At high fields, the majority of the carries populate the L valleys. Because of the larger curvature of the L valley, most of the LO phonons are now distributed over a large range of q-values with small forward drift. The overall drag effect is therefore destroyed. The phonon amplification leads to a frictional effect responsable for a reduction of the drift velocity. Figure 41 also shows that for high mobility materials (when ionized impurity scattering is negligible) the drag effect is reduced, indicating even at low fields a stronger frictional action of the phonon disturbance.

As a final remark in the present section, it is important again to compare the optical injection case to the d.c. one, which exhibits much smaller hot phonon effects. In the photoexcitation case, carriers are generated at high energies, and relax towards the energy region where reabsorption plays a relevant role. Therefore, hot phonon effects become very important after the initial decay. On the contrary, for d.c. excitations, carriers start from an equilibrium configuration and are heated by the applied field. The higher the field, the smaller will be the effect of phonon reabsortion.

7. Conclusions

A full Monte Carlo technique for the study of electron and phonon dynamics in bulk GaAs, InP and in AlGaAs-GaAs quantum wells has been presented. The method does not require any assumption on the form of the distribution function, and provides a detailed microscopic description of the transport phenomena. For the photoexcitation case, it has been shown

that during the initial stage of the relaxation a strong emission of LO phonons occurs which drives the phonon distribution function out of equilibrium. The presence of a perturbed LO phonon population causes a reduction of the cooling rate of the photoexcited electrons. Such a reduction, which is a function of the excitation conditions and of the lattice temperature, is caused by a sizeable reabsorption of LO phonons by the cooling electrons. Peculiar differences in the time evolution of the electron and phonon distributions are found in GaAs vs InP, due to the contribution of the satellite valleys in the former material. The results of the Monte Carlo simulation compare favourably with available experimental results obtained with time resolved photoluminescence and Raman measurements. The slowing down of the photoexcited electrons due to the presence of hot phonons has also been found in GaAs-AlGaAs quantum wells.

In the d.c. field case, the phonon-induced modification in the energy dissipation of the hot carriers leads to a slight increase of the drift velocity at low field (drag effect) and to a small decrease at high fields (frictional effect).

I would like to acknowledge P. Bordone, B. Deveaud, D.K. Ferry, S.M. Goodnick C. Jacoboni, P. Kocevar, L. Reggiani, M. Rieger, and J. Shah for their contribution to part of the work reported here and for helpful discussions. Partial support from the Italian National Research Council (CNR) and the Computer Center of the Modena University (CICAIA) is gratefully acknowledged.

REFERENCES

Babiker, M., 1986, J. Phys. C **19**, 683

Babiker, M., M.P. Chamberlain, and B.K. Ridley, 1987, Semicond. Sci. Technol. **2**, 582

Bordone, P., C. Jacoboni, P.Lugli, L.Reggiani and P. Kocevar, 1985, Physica **134B**, 169

Bordone, P., C. Jacoboni, P. Lugli, L. Reggiani and P. Kocevar, 1987, J. Appl. Phys. **61**, 1460

Bosi, S., and C. Jacoboni, 1976, J. Phys. C. **9**, 315

Brunetti, R., C. Jacoboni, A. Matulionis, and V. Dienys, 1985, Physica **134B**, 369

Cai, W., C. M. Marchetti, M. Lax, 1987, Phys. Rev. B **35**, 1369

Cardona, M., 1988, Superlatt. and Microstr. **5**, 27

Collet, J., and T. Amand, 1986, J. Phys. Chem. Solids **47**, 153

Collins, C.L., and P.Y. Yu, 1984, Phys. Rev. **B30**, 4501

Conwell, E., 1967, "High Field Transport in Semiconductors", Academic Press, New York

Damen, T.C., R. C. C. Leite, and J. Shah, 1970, Proc. X Int. Conf. Semicon., Eds. S. P. Keller, J. C. Hensel, F. Stern, (U.S. Atomic En. Comm.)

Das Sarma, S., J.K. Jain and R. Jakabert, 1988, Phys. Rev. **B37**, 4560

Das Sarma, S., W.Y. Lai and A. Kobayashi, 1987, Proc. 18th ICPS, Ed. by O. Engrström, p.651, World Scientific, Singapore

Doniach, S., 1959, Proc. Phys. Soc. (London) **73**, 849

Dresselhaus, G., A.F.Kipp, and C.Kittel, 1955, Phys.Rev. **98**, 368

Fawcett, W., D.A.Boardman, and S. Swain, 1970, J. Phys. Chem. Solids **31**, 1963

Fischetti, M.V., and Laux, S.E., 1988, Phys. Rev. **38**, 9721

Fuchs, R., and K.L. Kliever, 1965, Phys. Rev. **A140**, 1076

Goodnick, S.M., and P. Lugli, 1986, in Proc. of XVIII Int. Conf. Phys. Sem., Ed. O. Engström, p. 1527, World Scientific, Singapore

Goodnick, S.M., and P. Lugli, 1988a, Phys. Rev. **B37**, 2578

Goodnick, S.M., and P. Lugli, 1988b, Phys. Rev. **14**, 3014

Huang, K., and B. Zhu, 1988, Phys. Rev. **B38**, 13377

Kash, K., J. Shah, D. Block, A.C. Gossard, and W. Wiegmann, 1985, Physica **134B**, 189

Kash, J.A., J.C. Tsang and J.M. Hvam, 1985, Phys. Rev. Lett. **54**, 2151

Kim, K., K. Hess, F. Capasso, 1988, Apll. Phys. Lett. **52**, 1167

Klemens, P.G., 1966, Phys. Rev. **148**, 845

Kocevar, P., 1981, Solid State Comm. **38**, 531

Kocevar, P., 1985, Physica **134B**, 155

Kocevar, P., 1987, Festkörperprobleme (Advanced in Solid State Physics) **27**, 197

Kurosawa, T., 1966, in *Proceedings of the International Conference on the Physics of Semiconductors, Kyoto* , J. Phys. Soc. Jpn. Suppl. **21**, 424

Hammersley, J.M., and D.C. Handscomb, 1964, "Monte Carlo Methods", Methuen, London

Jacoboni, C., 1976, Proc. 13th Intern. Conf. Phys. Semic., edited by G.Fumi, Marves, Roma, p.1195.

Jacoboni, C., and P. Lugli, 1989, "Monte Carlo Simulation of Semiconductor Devices", Springer, Wien, to be published

Jacoboni, C., and L. Reggiani, 1983, Rev. Mod. Phys. **55**, 645

Jain, K.J., and S. Das Sarma, 1988, Phys. Rev. Lett. **62**, 2305

Jusserand, B., and M. Cardona, 1989, in "Light Scattering in Solids", EDS. M. Cardona and G. Guntherodt, Springer, Berlin

Leo, K., W.W. Rühle, H.J. Queisser, and K. Ploog, 1988, Phys. Rev. **B37**, 7121

Littlejohn, M.A., J.R.Houser, and T.H.Glisson, 1977, J. Appl. Phys. **48**, 4587

Lugli, P., and D.K.Ferry, 1983, Physica, **117B**, 251

Lugli, P., and D.K.Ferry, 1985a, Appl. Phys. Lett. **46**, 594

Lugli, P., and D.K.Ferry, 1985b, IEEE El.Dev.Lett. **EDL6**, 25

Lugli, P., and D.K.Ferry, 1985c, Physica B **129**, 532

Lugli, P., and D.K.Ferry, 1985d, IEEE Trans. Electron Dev., **ED-32**, 2431

Lugli, P., and D.K.Ferry, 1986, Phys. Rev. Lett. **56**, 1295

Lugli, P., and L. Reggiani, 1986, in "Noise in Physical Systems and 1/f Noise", Eds. A. D'Amico and P. Mazzetti, Elsevier, p. 235

Lugli, P., C. Jacoboni, L. Reggiani, and P. Kocevar, 1987, Appl. Phys. Lett. **50**, 1251

Lugli, P., and S.M. Goodnick, 1987, Phys. Rev. Lett. **59**, 716

Lugli, P., 1988 Sol. St. Electr. **31**, 667

Lugli, P., P. Bordone, L. Reggiani, M. Rieger, P. Kocevar, and S.M. Goodnick, 1989, Phys. Rev. **B39**, 7852

Luzzi, R. 1985, J. Luminescence **30**, 318

Menendez. J., 1989, to be published in J. of Luminescence

Mickevicius, R., and A. Reklaitis, 1987, Solid State Comm., **64**, 1305

Mooradian, A., and G. B. Wright, 1966, Solid State Comm. **4**, 431

Osman, M.A., M. J. Kann, D. K. Ferry and P. Lugli, 1987, in "Picosecond Electronics and Optoelectronics II", Eds. F. Capasso, C.H. Lee, F.J. Leonberges and H. Morkoc, p. 82, Springer Verlag, Berlin

Ottaviani, G., L.Reggiani, C.Canali, F.Nava, and A.Alberigi-Quaranta, 1975, Phys.Rev. B **12**, 3318

Pötz, W., 1987, Phys. Rev. B **36**, 5016

Pötz, W., and P. Kocevar, 1983, Phys. Rev. **B28**, 7040

Price, P.J., 1968, Proc. 9th Int. Conf. Phys. Semic., Edited by S.M.Ryvkin (Nauka, Leningrad p.753.

Price, P.J., 1979, in *Semiconductors and Semimetals* (Academic, New York) p.249

Price, P.J., 1981 Ann. Phys. (N.Y.) **133**, 217

Price, P.J., 1985 Physica **134B**, 165

Pugnet, M., J. Collet and A. Cornet, 1981, Solid State Comm. **38**, 531

Rees, H.D., 1968, Phys. Lett. a **26**, 416

Rees, H.D., 1969, J. Phys. Chem. Solids **30**, 643

Riddoch, F.A., and B. K. Ridley, 1983, J. Phys. C: Solid State Phys. **16** , 6971

Riddoch, F.A., and B.K. Ridley, 1985, Physica **134B**, 342

Ridley, B.K., 1989, Phys. Rev. **B39**, 5282

Rieger, M., P. Kocevar, P. Bordone, P. Lugli, and L. Reggiani, 1988, Sol. St. Electr. **31**, 687

Rieger, M., P. Kocevar, P. Lugli, P. Bordone, L. Reggiani, S.M. Goodnick, 1989, Phys. Rev. **B39**, 7866

Rota, L., and P. Lugli, 1989, to be published in Solid State Electr.

Rubinstein, R.V., 1981 "Simulation and the Monte Carlo Method", Wiley, New York

Ryan, J.F., R. A. Taylor, A. J. Turbefield, and J. M. Worlock, 1986, Surf. Sci. **170**, 511

Ryan, J.F., M. Tatham, D.J. Westland, C.T. Foxon, M.D. Scott, and W.I. Wang, 1988, in "Proc. SPIE" **942**, p. 256

Sawaki, N.J., 1986, J. Phys. C. **19**, 4965

Shah, J., B. Deveaud, W.T. Tsang, A.C. Gossard, and P. Lugli, 1987, Phys. Rev. Lett. **59**, 2222

Shah, J., R.C.C. Leite and J.F. Scott, 1970, Solid State Comm. **8**, 1089

Shah, J., A. Pinczuk, A. C. Gossard, and W. Wiegmann, 1985, Phys. Rev. Lett. **54B**, 2045

Spanier, J., and E.M. Gelbard, 1969, "Monte Carlo Principles and Neutron Transport Problems", Addison-Wesley, Reading

Tang, J.Y., and K.Hess, 1983, J. Appl. Phys. **54**, 5139

Tsen, K.T., R.P. Joshi, D.K. Ferry, and H. Morkoc, 1988, Phys. Rev. **B39**, 1446

von der Linde, D., J. Kuhl and H. Klingenberg, 1980, Phys. Rev. Lett. **44**, 1505

Xu, Z.Y., and C. L. Tang, 1984, Appl. Phys. Lett. **44**, 692

Yang, C.H., J.M. Carlson-Swindle, S. A. Lyon, and J. M. Worlock, 1986, Phys. Rev. Lett. **54**, 2045

Yu. Shreider, A., 1966, Ed., "The Monte Carlo Method", Pergamon, Oxford

FIGURE CAPTIONS

Fig. 1. Schematic representation of the energy flux in a typical semiconductor.

Fig. 2. Schematic of the rejection technique used for the selection of the final state in the Monte Carlo algorithm for hot-phonon effects. The two random numbers r_1 and r_2 are uniformely distributed in the range $(0,q_{max})$ and $(0,N_{max})$, respectively. The case illustrated in the figure represents an accepted scattering event.

Fig. 3. Non-equilibrium LO-phonon distribution functions at three different delay times as a function of the phonon wavevector. The insert shows the shape of the laser pulse.

Fig. 4. Time evolution of four different modes as a function of delay time.

Fig. 5. Energy dependence of the minimum wavevector for absorption and emission of LO phonons, as a function of energy in a parabolic band. The shaded area indicates typical Raman-active phonon wavevectors and E_{inj} is the energy value at which carrier are initially injected measured from the bottom of the conduction band.

Fig. 6. Total scattering rates for polar-optical interaction at different times after the excitation as compared with their equilibrium value.

Fig. 7. Electron distribution function of carrier energy, at different delay times.

Fig. 8. Average electron energy, measured in equivalent temperature, as a function of time with (continuous curve) and without (dashed curve) hot-phonons.

Fig. 9. Non-equilibrium phonon distribution for an excitation energy of 80 meV and an electron concentration of $10^{16}cm^{-3}$ for an 80 fs laser pulse at two different delay times.

Fig. 10. Minimum wavevector for absorption and emission of LO phonons as a function of energy in a parabolic band for the Γ and the L valleys of GaAs.

Fig. 11. Phonon histogram (a) and distribution function (b) at 1 ps after the excitation, for an initial electron energy of 0.5 eV.

Fig. 12. Average electron energy, measured in equivalent temperature, as a function of time during and after the laser excitation for two different excitation sheet densities. The position of the energy levels in the well is shown in the insert.

Fig. 13. LO-phonon distribution as a function of total parallel momentum (for $q_z = 0$) for times during and after the laser excitation.

Fig. 14. Time evolution of various phonon modes obtained by using three different values for τ_{op}.

Fig. 15 Scattering rate for optical phonon emission in a 150 A QW at 10 K. Dashed and dotted lines show respectively the contribution of guided and surface modes, compared with the 3D bulk rate (continuous curve)

Fig. 16 Electron average energy as a function of time after excitation (with a 1ps laser pulse) for three different values of the phonon lifetime

Fig. 17 Hole average energy as a function of time after excitation (with a 1ps laser pulse) for three different values of the phonon lifetime

Fig. 18 Nonequilibrium phonon distribution for three guided modes ($m = 1,2,3$) at 1ps time delay

Fig. 19 Nonequilibrium phonon distribution for the first ($m = 1$) guided modes, at three different times after photoexcitation.

Fig. 20. Schematic representation of the excitation process in polar semiconductors.

Fig. 21. Energy distribution function for Γ-valley electrons in GaAs (a) and InP (b) at three different time delays after the excitation. The excitation density is 5×10^{16} cm^{-3} and the lattice temperature is 300 K.

Fig. 22. Luminescence spectra of GaAs at three different delays after excitation. Zero delay correspond to the center of the excitation pulse (of 400 fs at $2.04eV$. Full circles indicate the MC results, the continuos lines the experimental data.

Fig. 23 Luminescence intensity versus time for GaAs and InP at room temperature

Fig. 24. Average energy, measured in equivalent temperature, of the Γ-valley electrons for different excitation densities in GaAs (a) and InP (b) at T_L=300 K.

Fig. 25. LO-phonon distribution for Γ-valley electron in GaAs (a) and InP (b) for three different time delays after the excitation at T_L=300 K.

Fig. 26. Time evolution of the Raman-active modes for two different temperatures. The experimental results of Kash et al. (1985) are shown in the insert.

Fig. 27 Detailed view of the low-energy portion of the energy distribution function in GaAs at three different densities and in InP at the lowest density. The values indicate the electron temperature deduced from the slope of the curves.

Fig. 28 Monte Carlo calculations of the Raman-active modes as a function of the laser-pulse

energy under the condition of Collins and Yu's experiment [31] for two different values of the Γ-L coupling; (∩) $D_{\Gamma L} = 7.0 \times 10^8$ eV/cm, (•) $D_{\Gamma L} = 1.5 \times 10^8$ eV/cm.

Fig. 29 Monte Carlo calculations of the Raman active modes as a function of time under the condition of Shah et al. experiment [46] for two different values of the Γ-L coupling; (∩) $D_{\Gamma L} = 7.0 \times 10^8$ eV/cm, (•) $D_{\Gamma L} = 1.5 \times 10^8$ eV/cm.

Fig. 30 Average electron velocity as a function of time with (dashed line) and without (continous line) phonon disturbance

Fig. 31 Average electron energy in the Γ valley as a function of time with (dashed line) and without (continous line) phonon disturbance

Fig. 32 Forward LO phonon distribution function at two different times.

Fig. 33 Electron occupation of Γ valley at two different times

Fig. 34 Average electron velocity as a function of time: with phonon disturbances (dashed line) for both screened and unscreened coupling; without phonon disturbances for screened (full line) and unscreened (dashed-dotted) coupling.

Fig. 35 Average electron energy in the Γ valley as a function of time: with phonon disturbances for screened (dashed line) and unscreened (dotted line) coupling; without phonon disturbances for screened (full line) and unscreened (dashed-dotted) coupling.

Fig. 36 Average energy and relative valley population of Γ-valley electrons as a function of time with (dashed lines) and without (continuous lines) phonon disturbances.

Fig. 37 Average electron velocity and average energy of L-valley electrons as a function

of time with (dashed and dotted lines) and without (continuous and dashed-dotted lines) phonon disturbances.

Fig. 38 Perturbed LO phonon distribution for forward modes at two different times after turning on the electric field.

Fig. 39 Occupation number for the Γ Valley electrons for two electric fields below (a) and above (b) the threshold for intervalley transfer, with and without phonon disturbances.

Fig. 40 Steady state drift velocity as a function of electric field with (dashed lines) and without (continuous line) phonon amplification.

Fig. 41 Steady state drift velocity as a function of electric field for the case of remote ionized-impurity scattering with (dashed lines) and without (continuous line) phonon amplification.

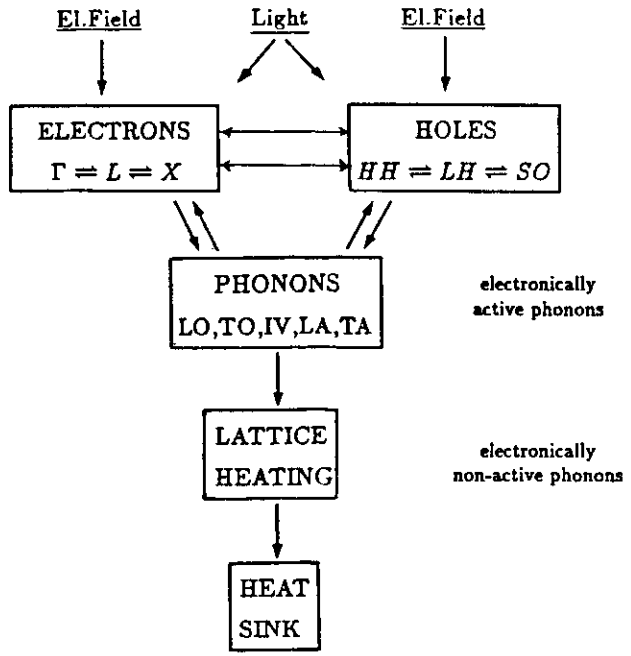

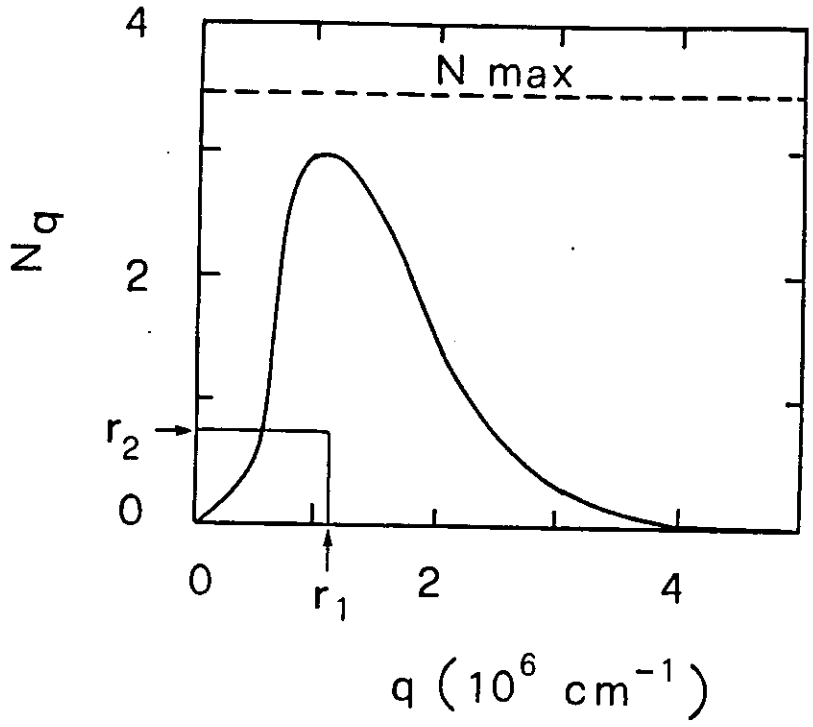
4
N max
N_q
2
r_2
0
0
r_1
2
4
q (10^6 cm^{-1})

Fig 2

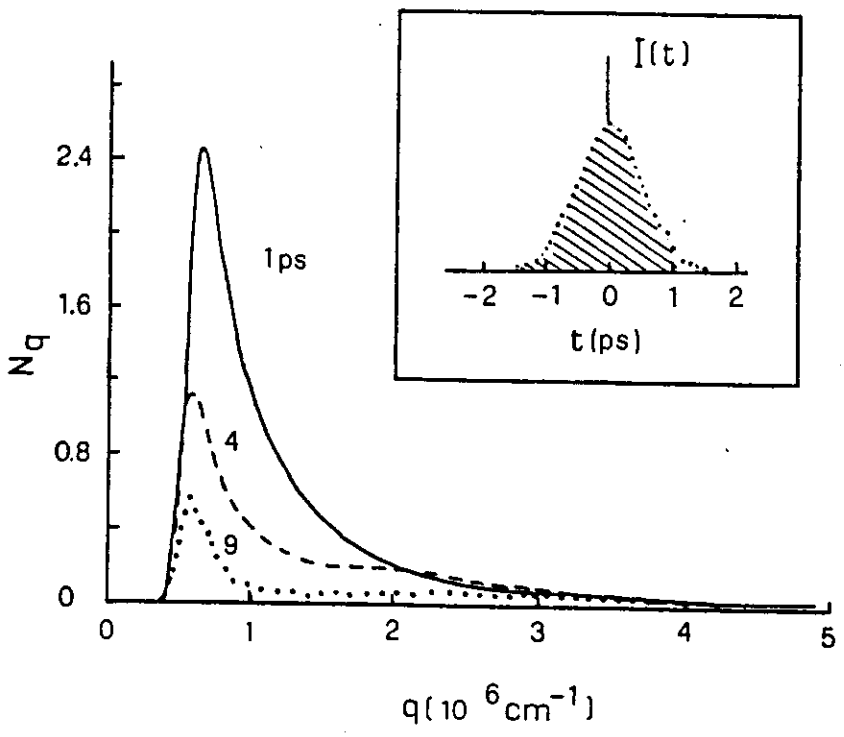
I(t)
-2
-1
0
1
2
t(ps)
2.4
1.6
0.8
0
N_q
1ps
4
9
0
1
2
3
4
5
q(10^6 cm^{-1})

Fig 3

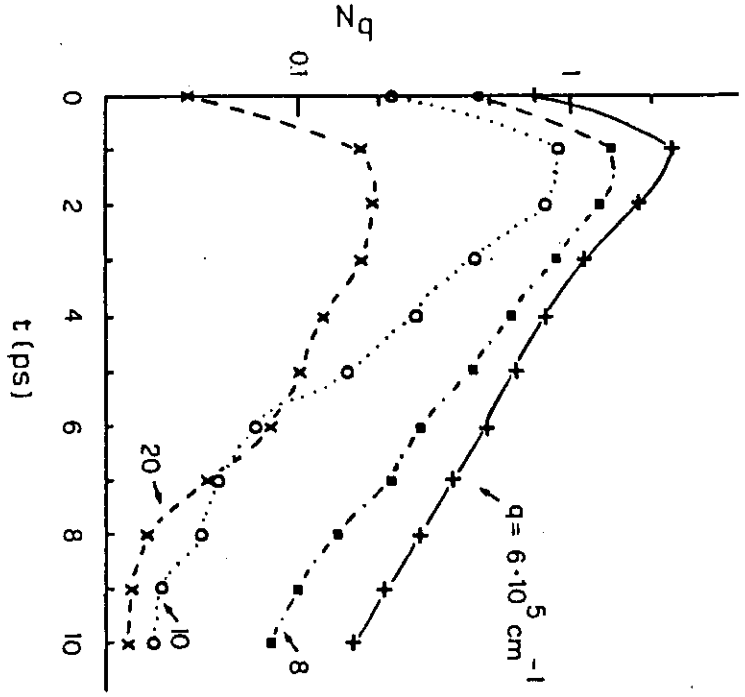
Nq
t (ps)
20
10
8
q= 6·10^5 cm^-1

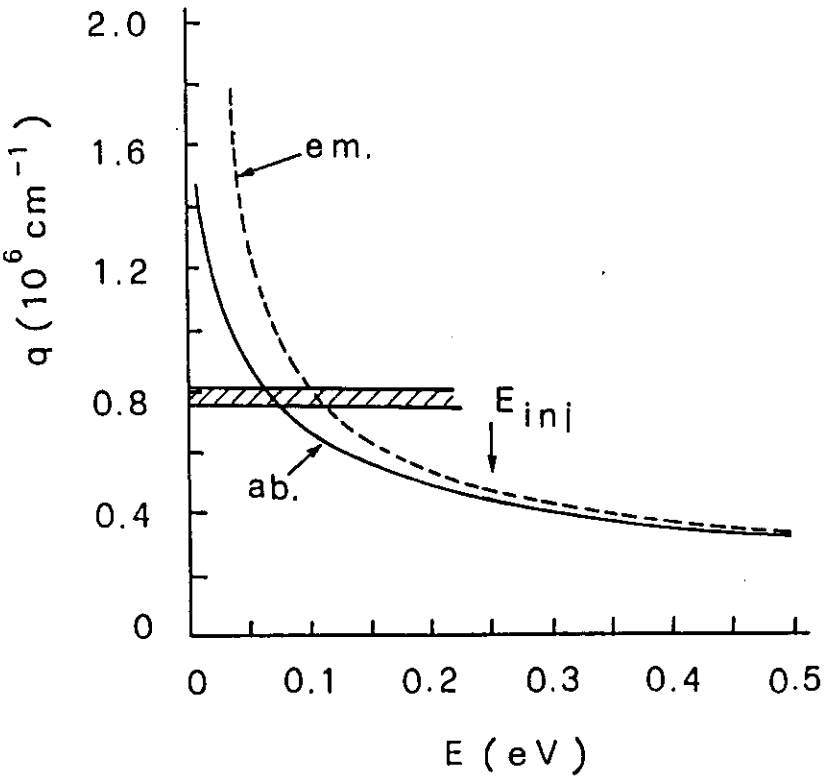
q (10^6 cm^-1)
em.
ab.
E inj
E (eV)

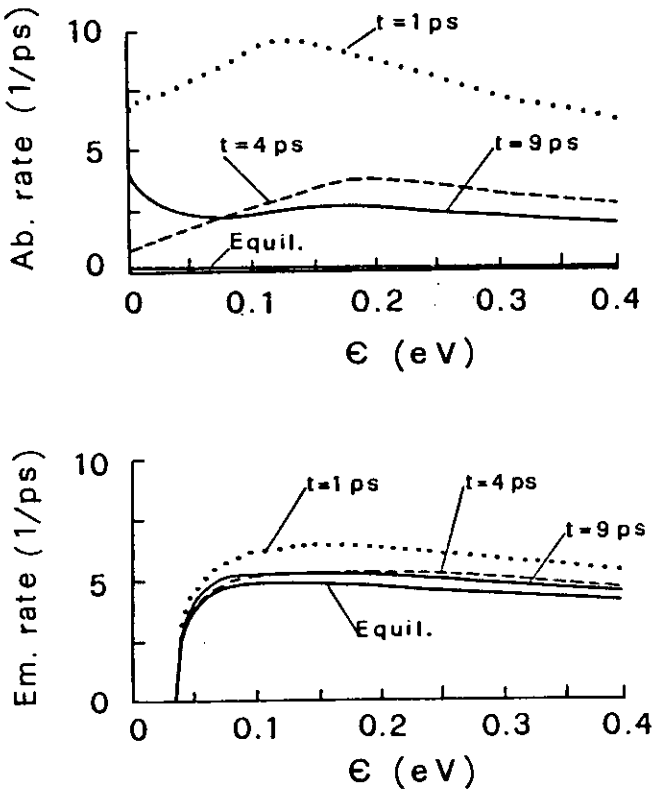
Ab. rate (1/ps)
10
5
0
t = 1 ps
t = 4 ps
t = 9 ps
Equil.
0
0.1
0.2
0.3
0.4
ϵ (eV)
Em. rate (1/ps)
10
5
0
t=1 ps
t=4 ps
t=9 ps
Equil.
0
0.1
0.2
0.3
0.4
ϵ (eV)

Fig 6

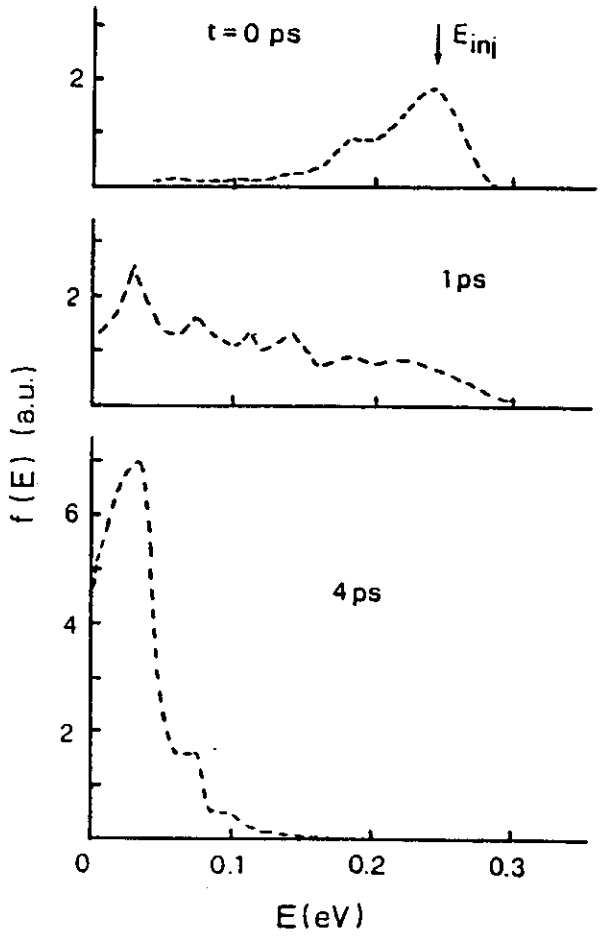
t = 0 ps
E_inj
2
2
1ps
f (E) (a.u.)
6
4
2
4ps
0
0.1
0.2
0.3
E(eV)

Fig 7

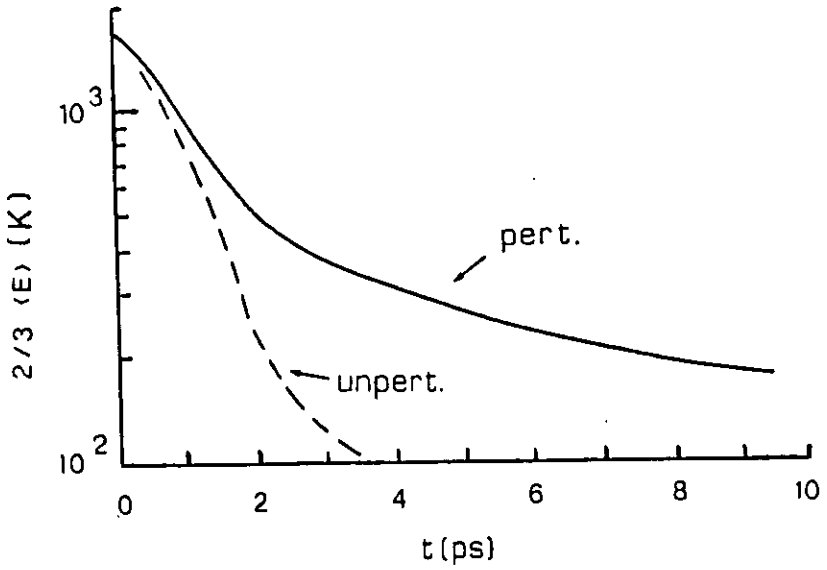
10^3
10^2
2/3 ⟨E⟩ (K)
pert.
unpert.
0
2
4
6
8
10
t(ps)

Fig 8

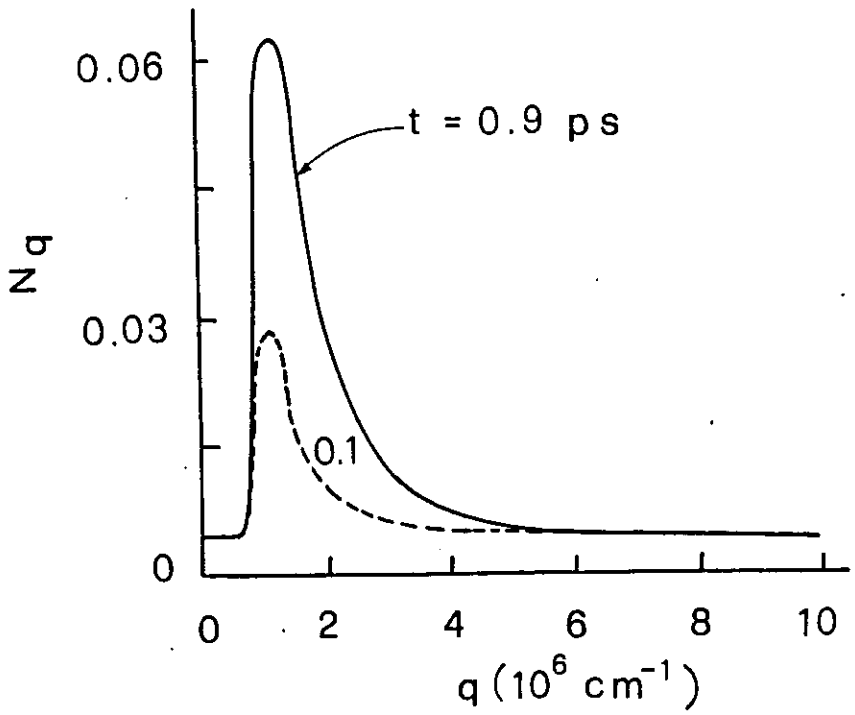
0.06
0.03
0
N_q
t = 0.9 ps
0.1
0
2
4
6
8
10
q (10^6 cm^{-1})

Fig 9

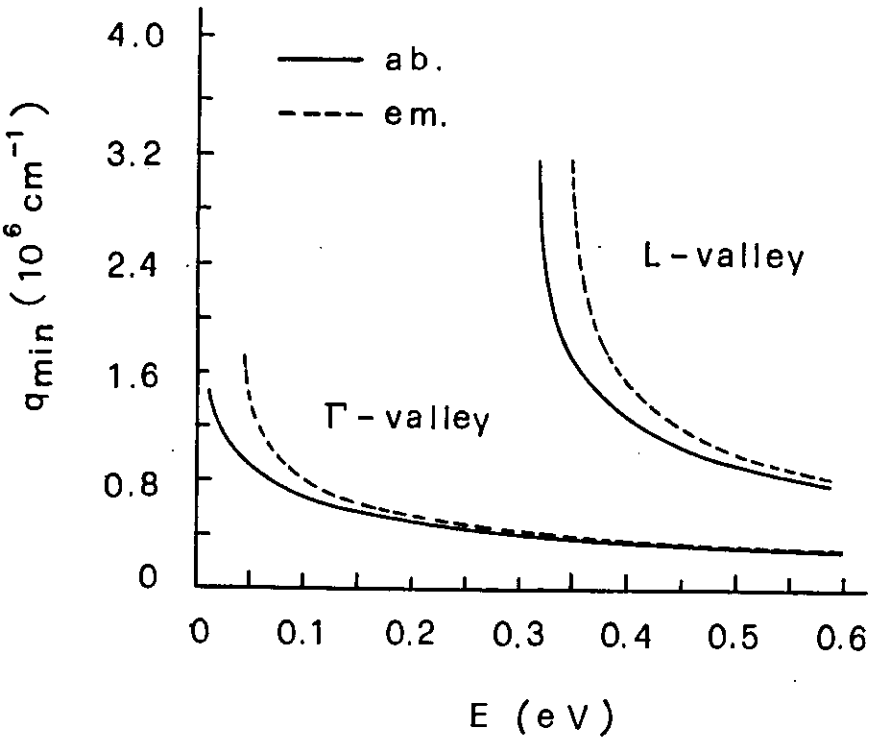
4.0
3.2
2.4
1.6
0.8
0
q_{min} (10^6 cm^{-1})
ab.
em.
L-valley
Γ-valley
0
0.1
0.2
0.3
0.4
0.5
0.6
E (eV)

Fig 10

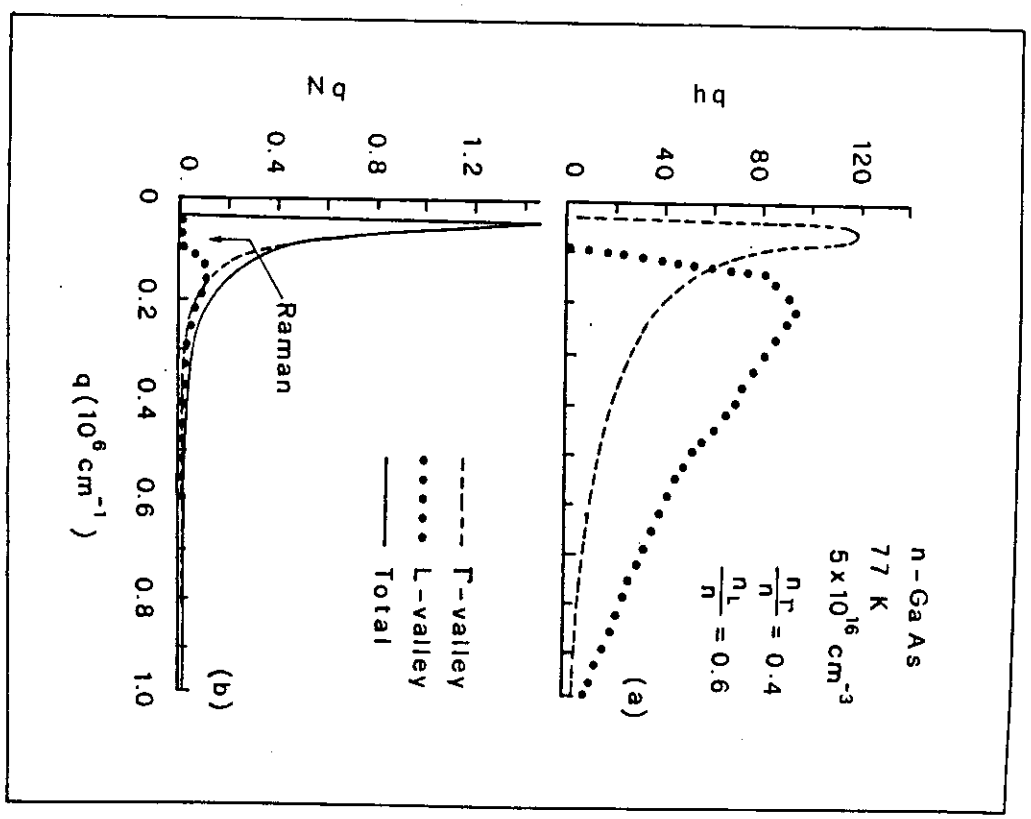
Nq
hq
0
0.4
0.8
1.2
40
80
120
Raman
Γ-valley
L-valley
Total
n-GaAs
77 K
5×10^{16} cm^{-3}
$\frac{n_\Gamma}{n} = 0.4$
$\frac{n_L}{n} = 0.6$
(a)
(b)
q (10^6 cm^{-1})
0.2
0.4
0.6
0.8
1.0

Fig 11

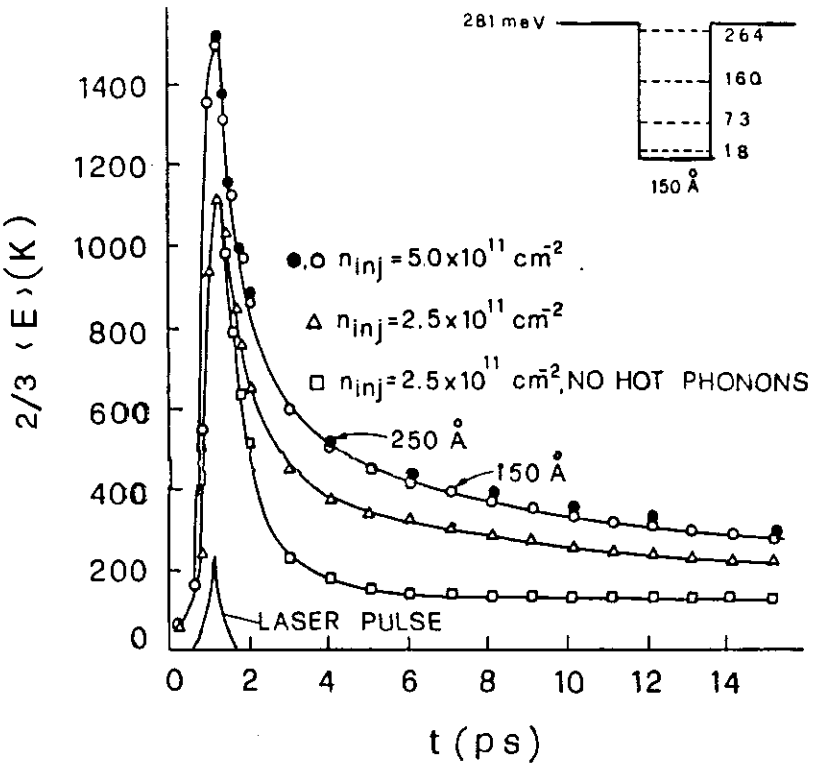
281 meV
264
160
73
18
150 Å
1400
1200
1000
800
600
400
200
0
2/3 ‹E›(K)
●,o $n_{inj}=5.0\times10^{11}$ cm^{-2}
△ $n_{inj}=2.5\times10^{11}$ cm^{-2}
□ $n_{inj}=2.5\times10^{11}$ cm^{-2}, NO HOT PHONONS
250 Å
150 Å
LASER PULSE
0 2 4 6 8 10 12 14
t (ps)

Fig 12

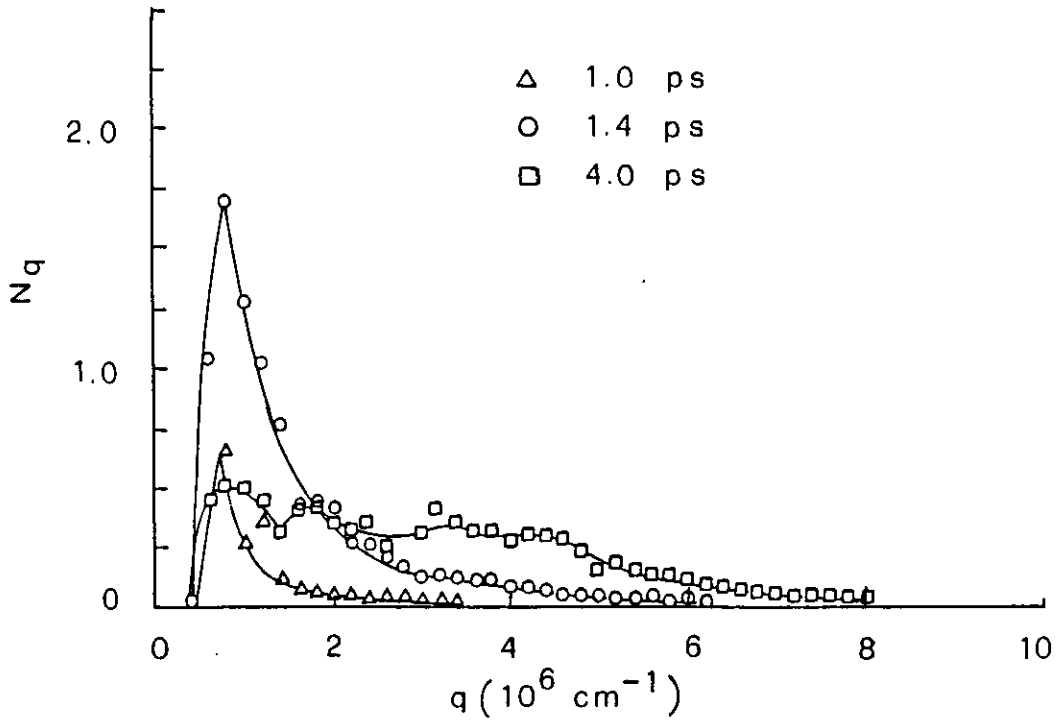
△ 1.0 ps
○ 1.4 ps
□ 4.0 ps
2.0
1.0
0
N_q
0 2 4 6 8 10
q (10^6 cm^{-1})

Fig 13

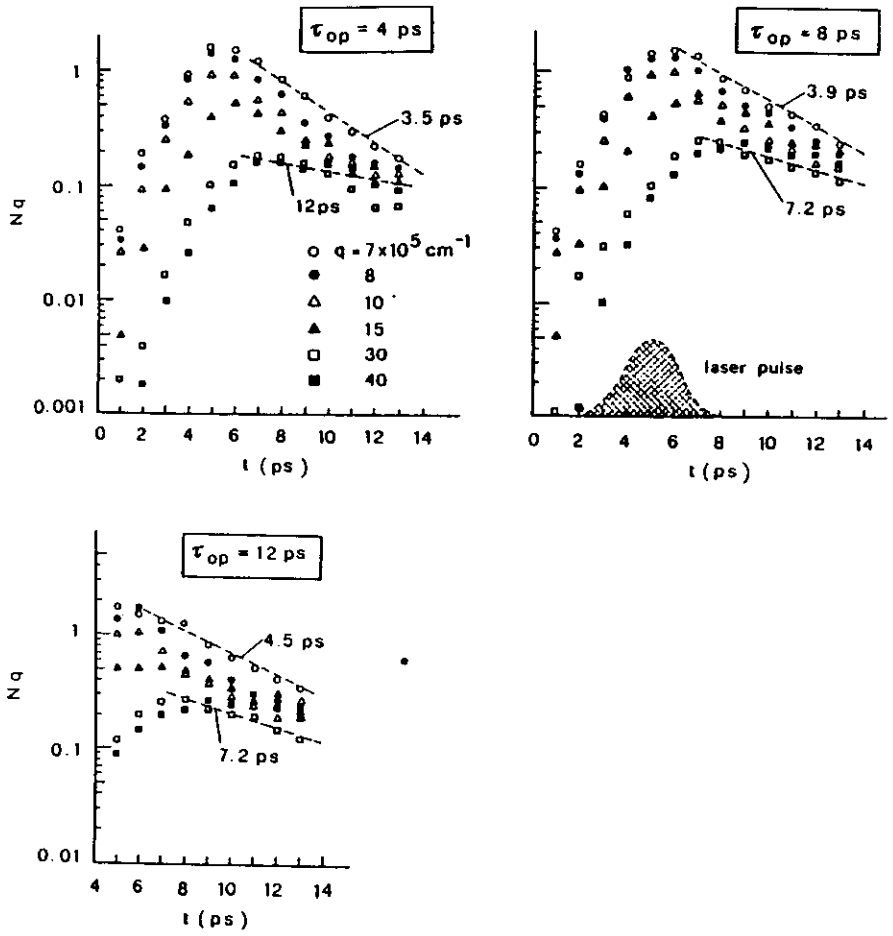
τ_{op} = 4 ps
3.5 ps
12ps
q = 7x10^5 cm^{-1}
8
10
15
30
40
Nq
t (ps)
τ_{op} = 8 ps
3.9 ps
7.2 ps
laser pulse
τ_{op} = 12 ps
4.5 ps
7.2 ps

Fig 14

Fig 15

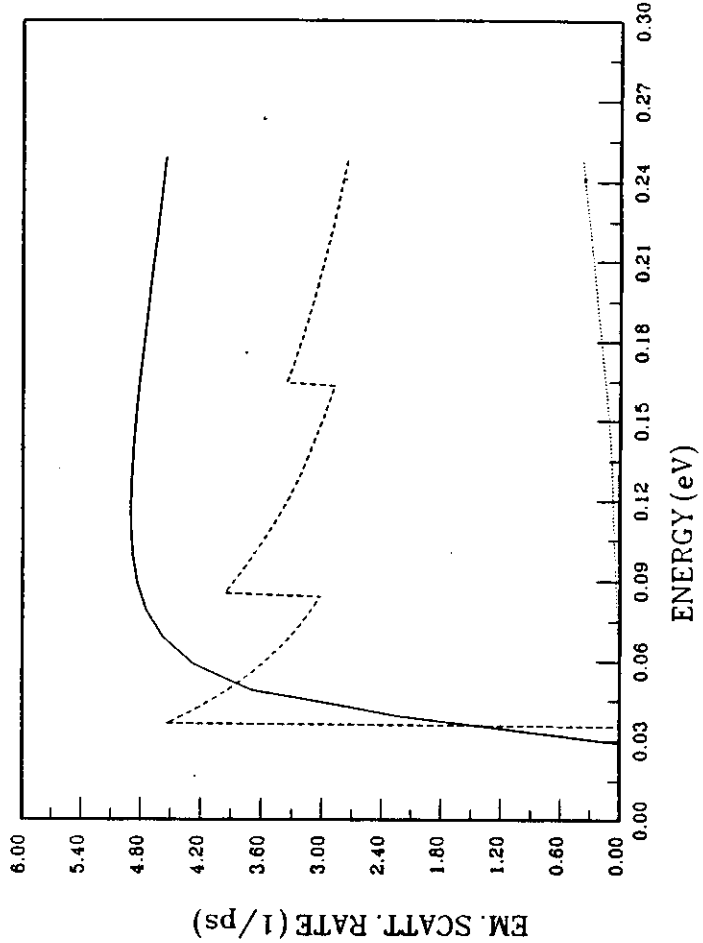
EM. SCATT. RATE (1/ps)
6.00
5.40
4.80
4.20
3.60
3.00
2.40
1.80
1.20
0.60
0.00
ENERGY (eV)
0.00
0.03
0.06
0.09
0.12
0.15
0.18
0.21
0.24
0.27
0.30

Electron average energy

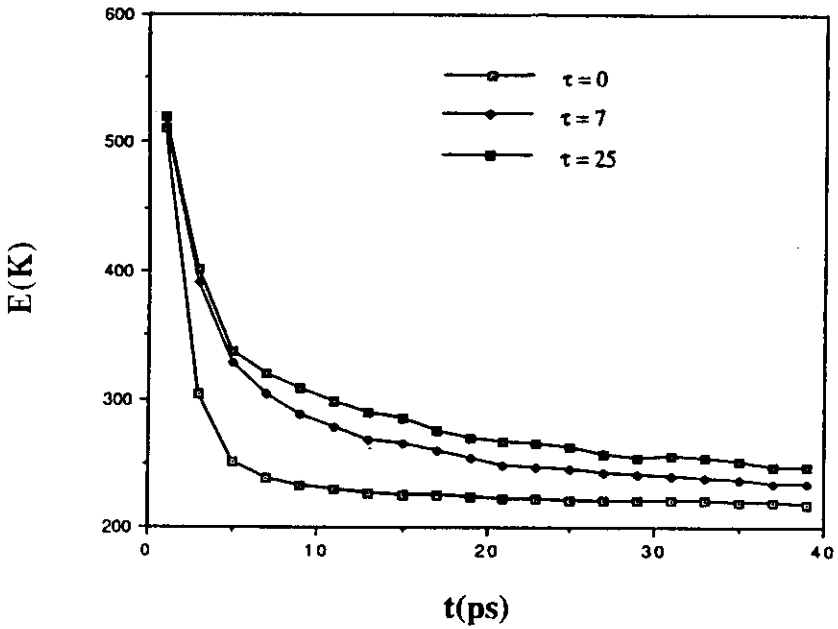

Hole average energy

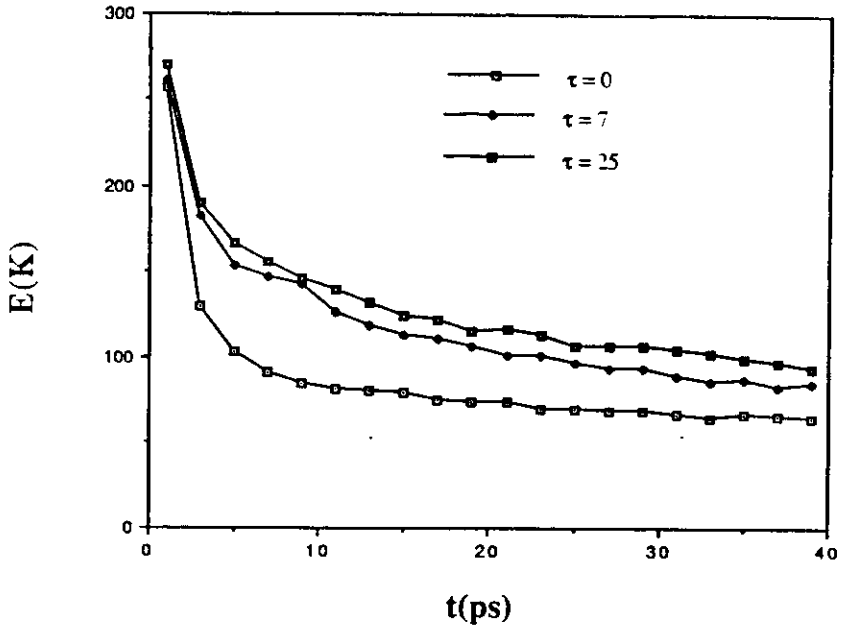

-123-

LO phonon distribution (guided modes) t = 1 ps

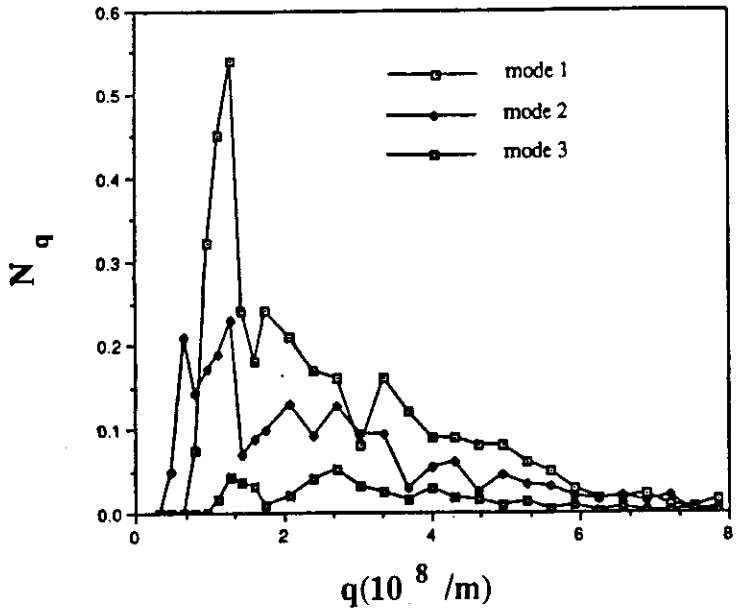

Fig. 18

-124-

LO phonon distribution (guided modes)

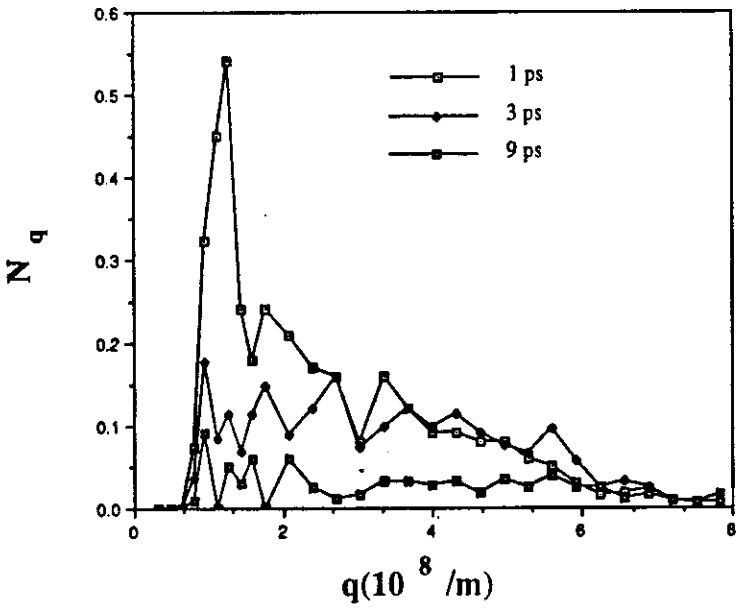

Fig. 19

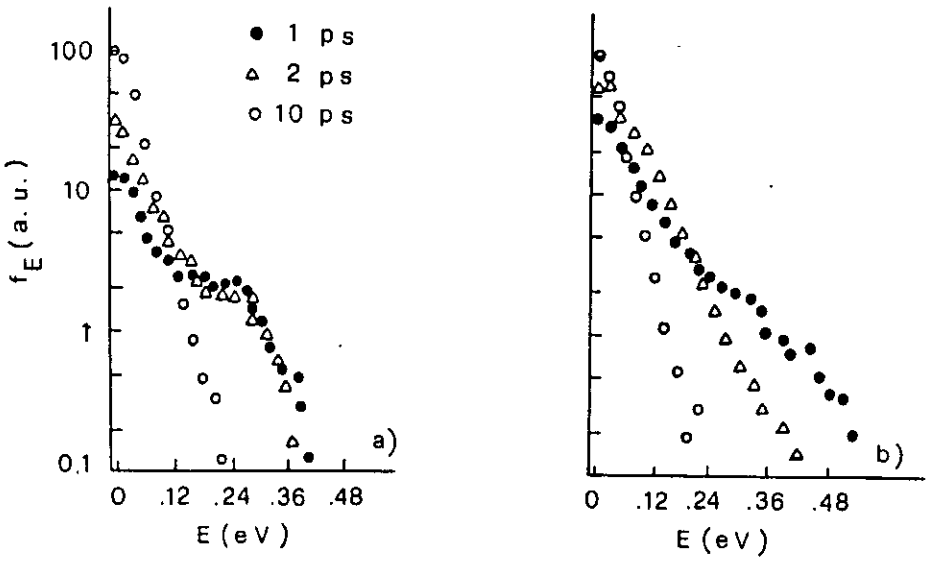
1 ps
2 ps
10 ps
100
10
1
0.1
f_E (a.u.)
0
.12
.24
.36
.48
E (eV)
a)
b)

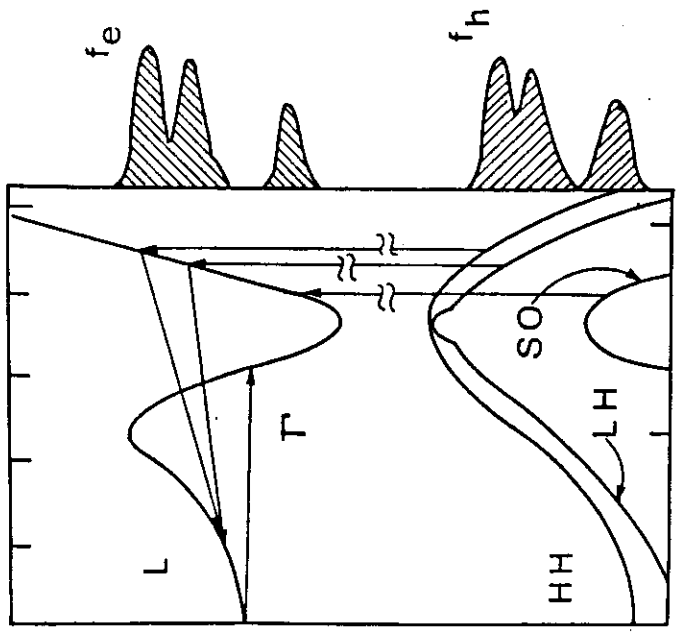
f_e
f_h
Γ
L
SO
LH
HH

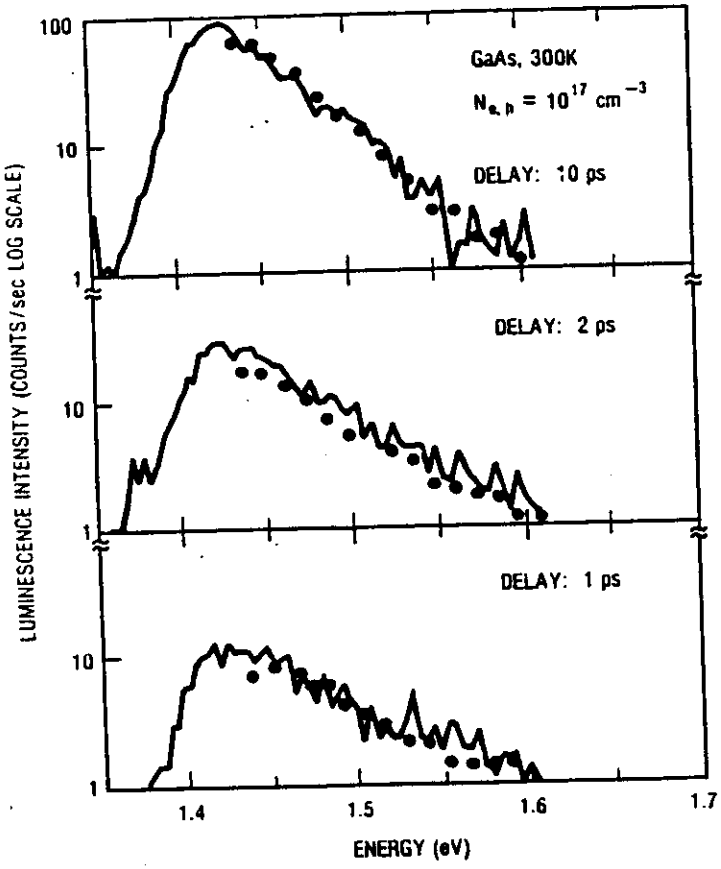
GaAs, 300K
$N_{e,h} = 10^{17}$ cm^{-3}
DELAY: 10 ps
DELAY: 2 ps
DELAY: 1 ps
LUMINESCENCE INTENSITY (COUNTS/sec LOG SCALE)
100
10
1
1.4
1.5
1.6
1.7
ENERGY (eV)

Fig. 22

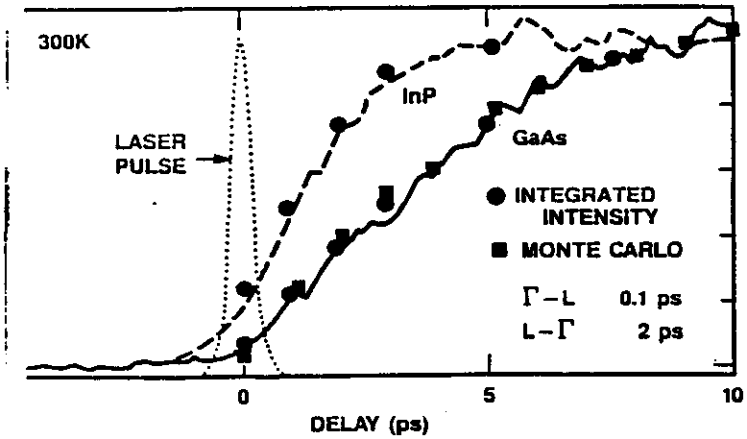
300K
LASER PULSE
InP
GaAs
INTEGRATED INTENSITY
MONTE CARLO
Γ–L 0.1 ps
L–Γ 2 ps
0
5
10
DELAY (ps)

Fig 23

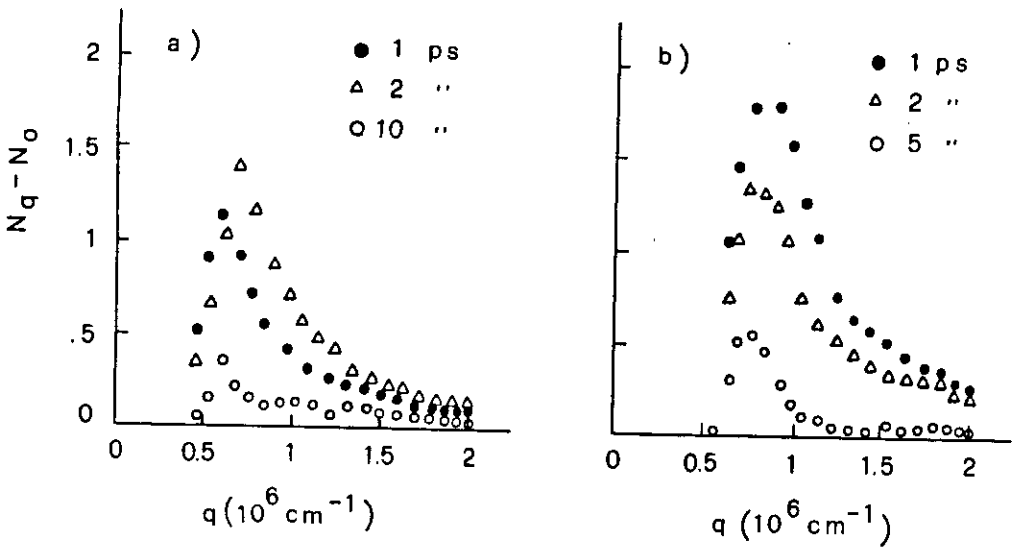
a)
1 ps
2 "
10 "
$N_q - N_o$
$q(10^6 cm^{-1})$
b)
1 ps
2 "
5 "
$q\ (10^6 cm^{-1})$

Fig 25

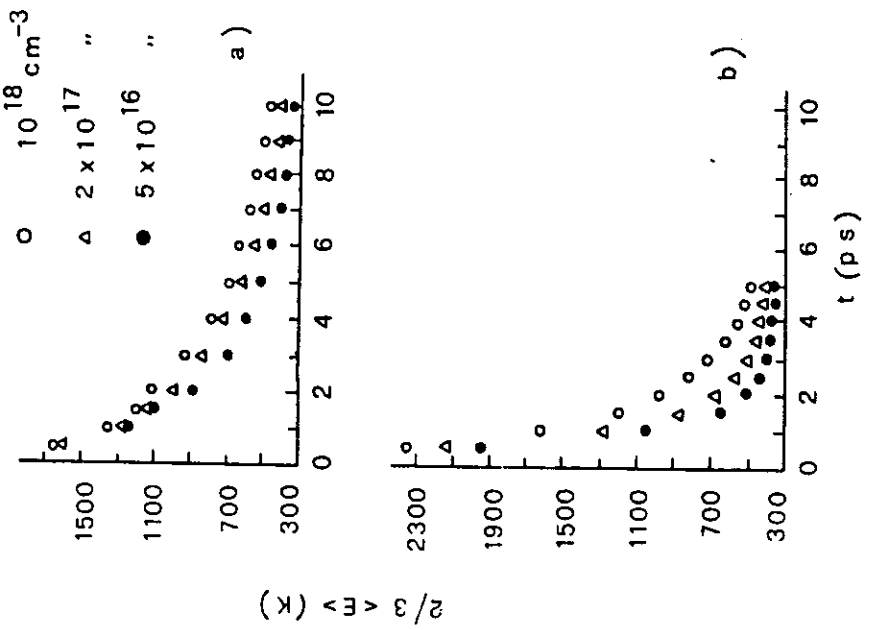
a)
$10^{18} cm^{-3}$
2×10^{17} "
5×10^{16} "
b)
t (ps)
$2/3 < \varepsilon > (K)$

Fig 26

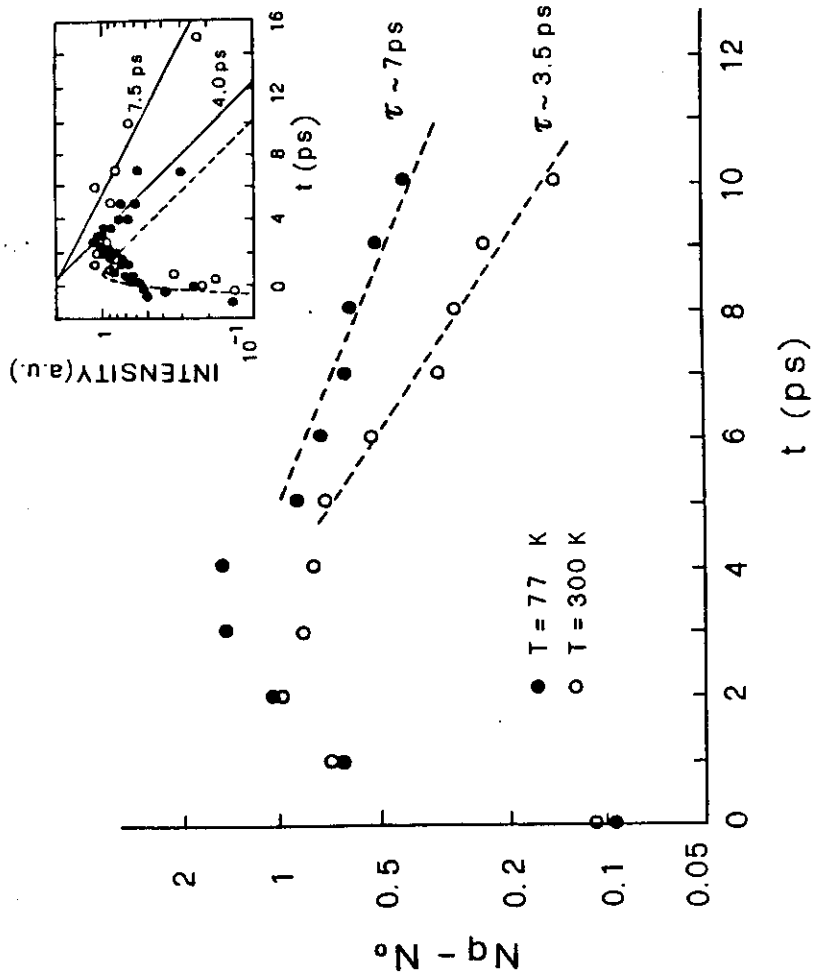
INTENSITY (a.u.)
7.5 ps
4.0 ps
t (ps)
τ ~ 7ps
τ ~ 3.5 ps
T = 77 K
T = 300 K
t (ps)
$N_0 - N_0$

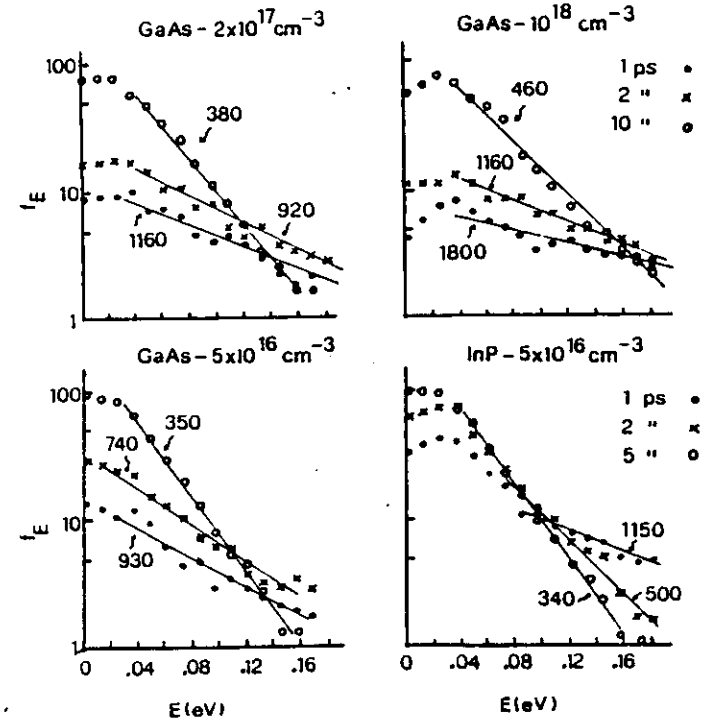
GaAs - 2x10^17 cm^-3
GaAs - 10^18 cm^-3
GaAs - 5x10^16 cm^-3
InP - 5x10^16 cm^-3
1 ps
2 "
10 "
5 "
380
460
1160
920
1800
350
740
930
1150
340
500
E(eV)

Fig 27

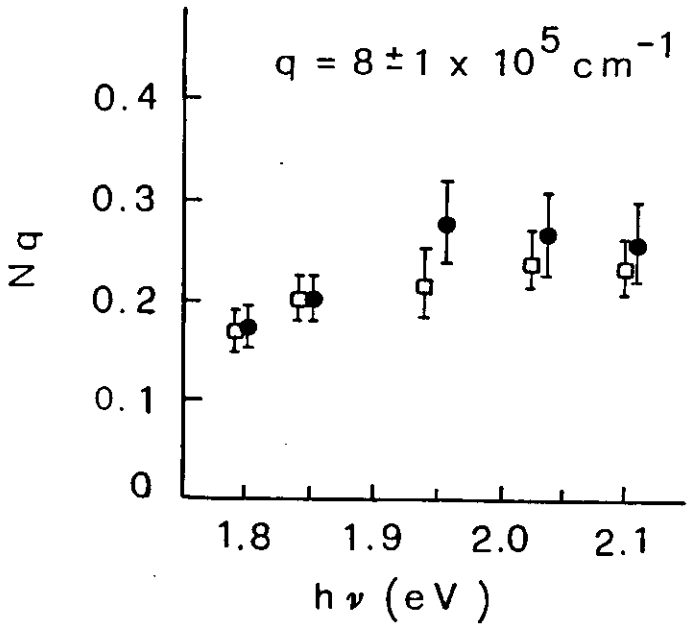
q = 8 ± 1 x 10^5 cm^-1
Nq
0.4
0.3
0.2
0.1
0
1.8
1.9
2.0
2.1
hν (eV)

Fig 28

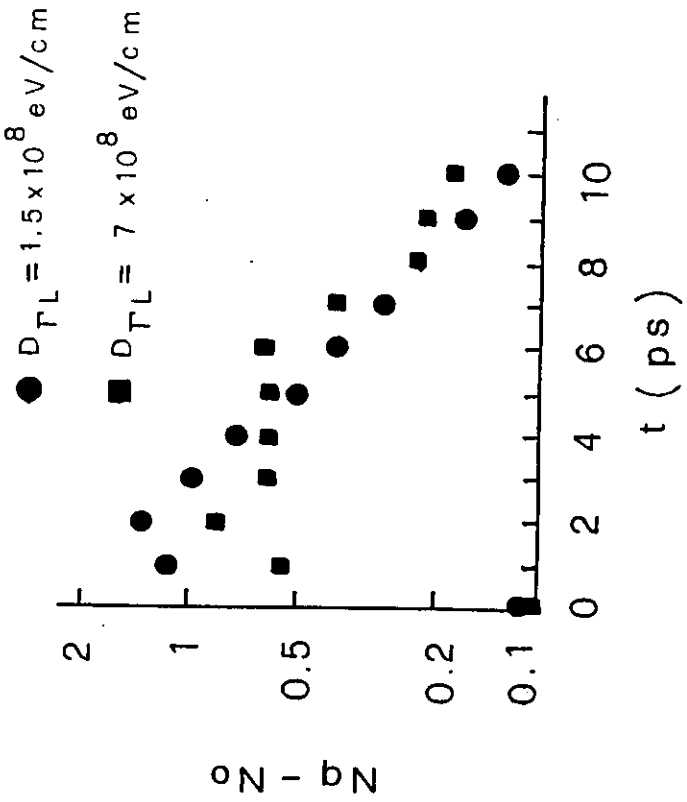
D_TL = 1.5 x 10^8 eV/cm
D_TL = 7 x 10^8 eV/cm
2
1
0.5
0.2
0.1
0
2
4
6
8
10
t (ps)
oN - bN

Fig 29

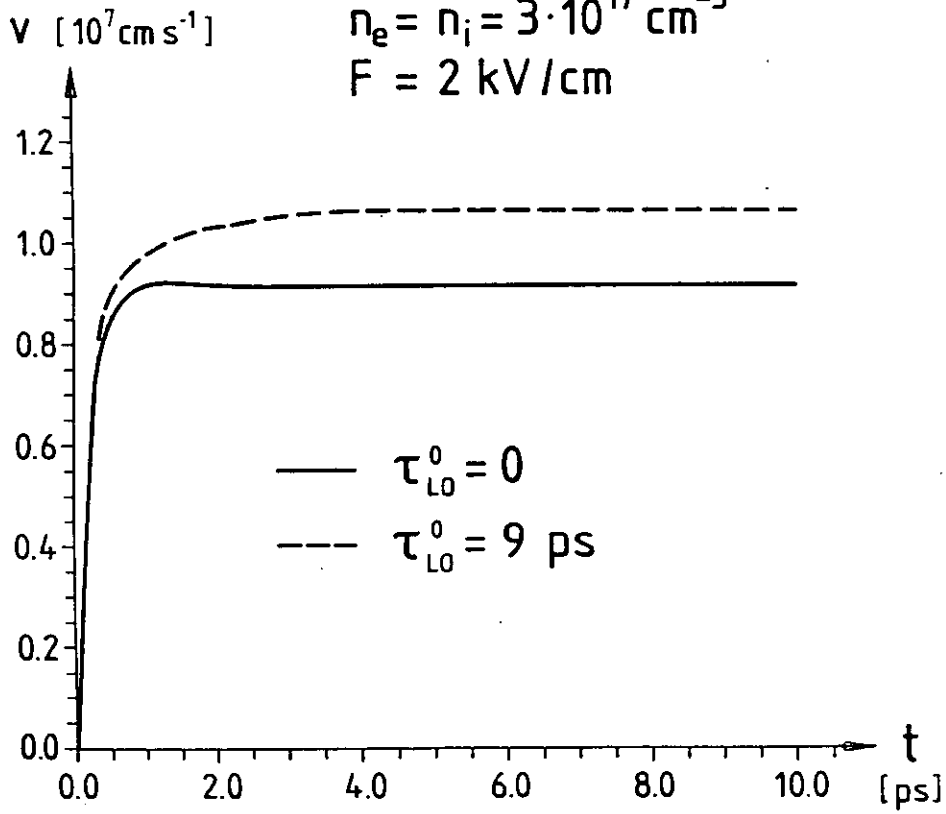

Fig 30

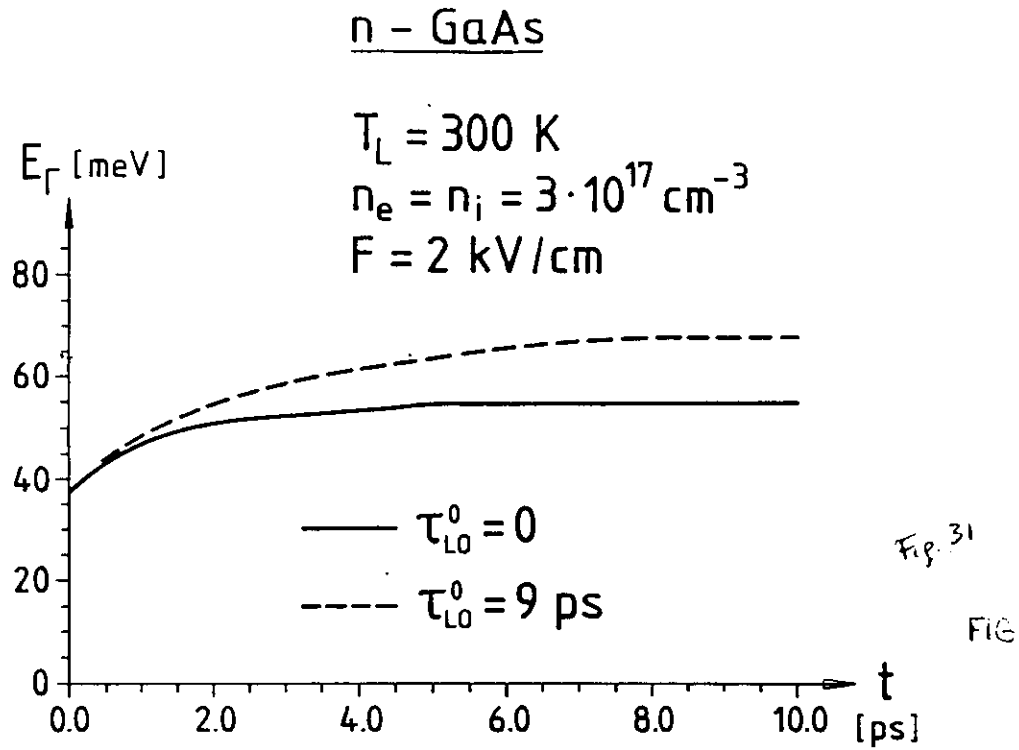

Fig 31

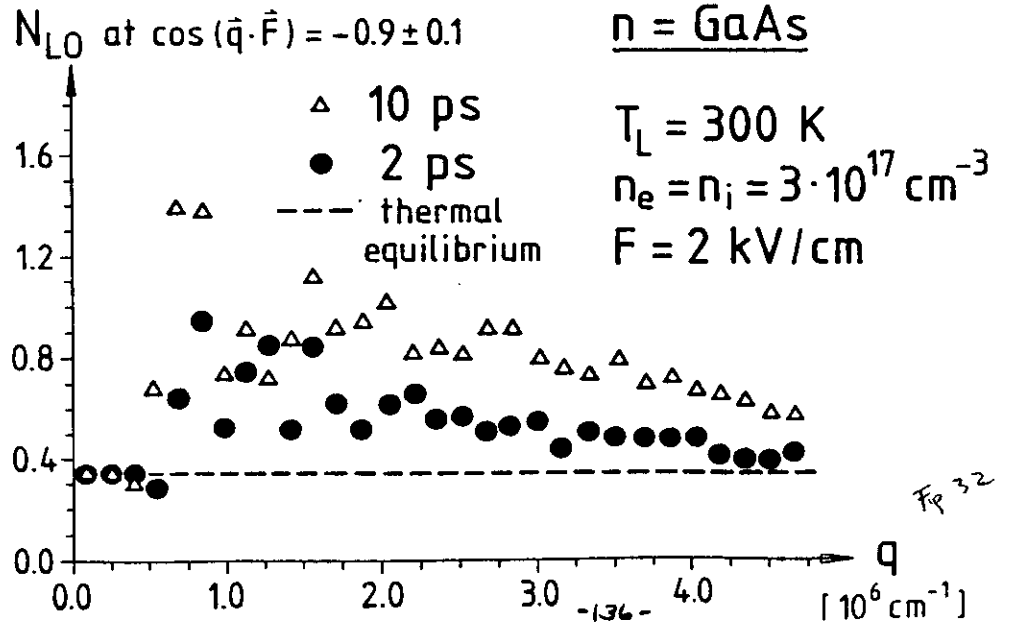

Fig 32

n – GaAs

$T_L = 300$ K
$n_e = n_i = 3 \cdot 10^{17}\ cm^{-3}$
$F = 2$ kV/cm
$\tau^0_{LO} \doteq 9$ ps

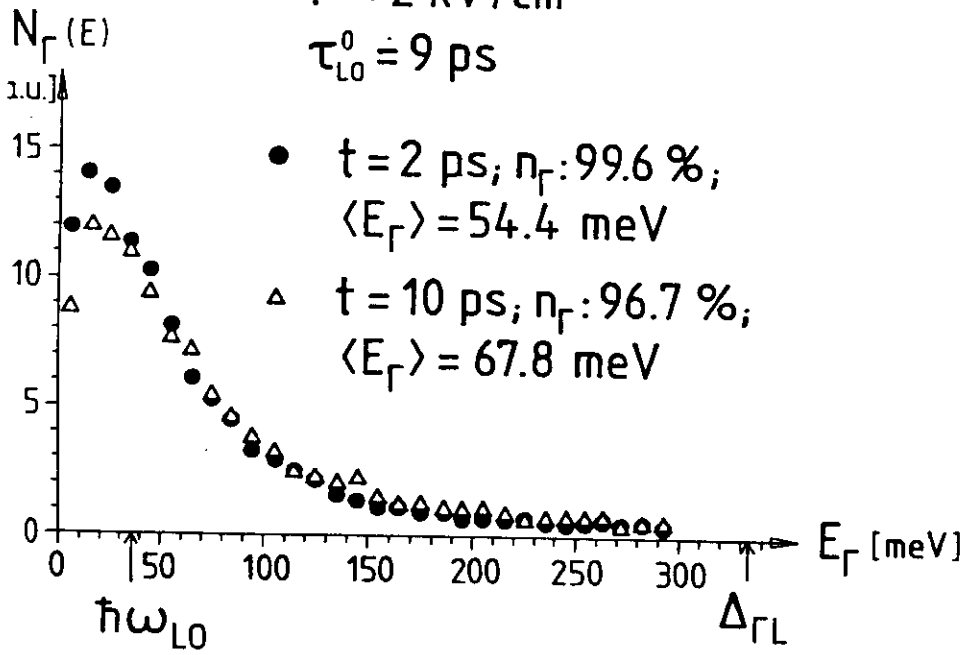

● $t = 2$ ps; n_Γ: 99.6 %; $\langle E_\Gamma \rangle = 54.4$ meV

△ $t = 10$ ps; n_Γ: 96.7 %; $\langle E_\Gamma \rangle = 67.8$ meV

Fig. 33

n – GaAs

$T_L = 77$ K
$n_e = n_i = 3 \cdot 10^{17}\ cm^{-3}$
$F = 2$ kV/cm

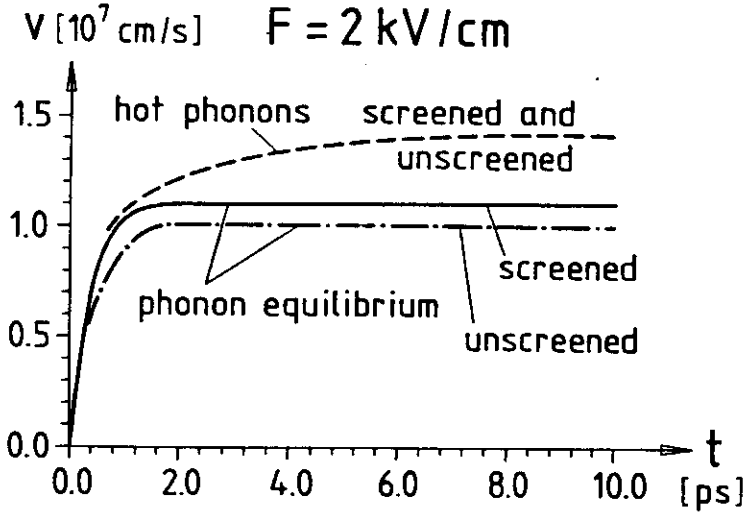

Fig. 34

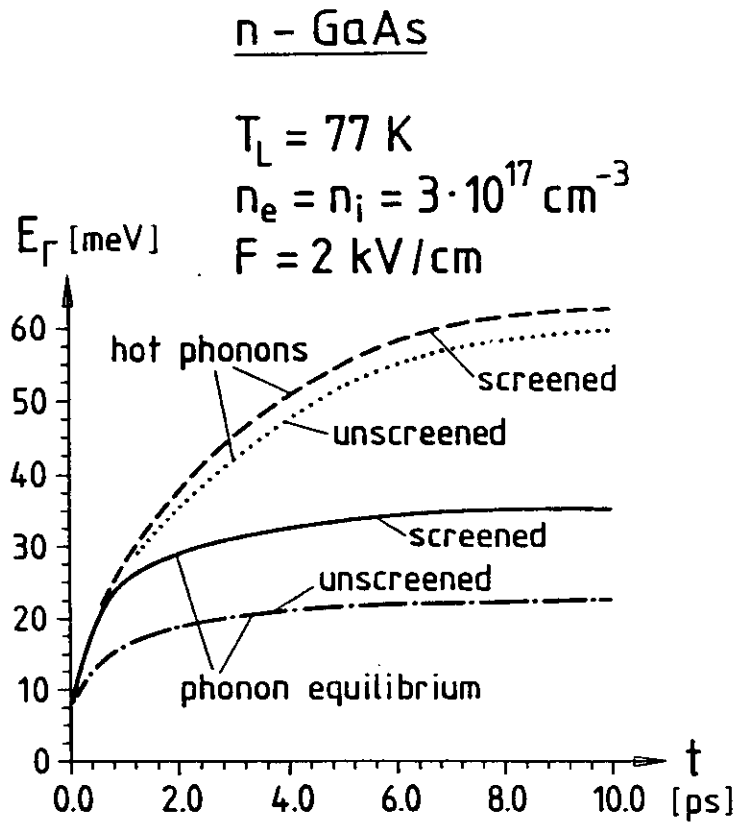
n - GaAs
T_L = 77 K
$n_e = n_i = 3 \cdot 10^{17}\,cm^{-3}$
F = 2 kV/cm
E_Γ [meV]
hot phonons
screened
unscreened
screened
unscreened
phonon equilibrium
t
[ps]
0
10
20
30
40
50
60
0.0
2.0
4.0
6.0
8.0
10.0

Fig 35

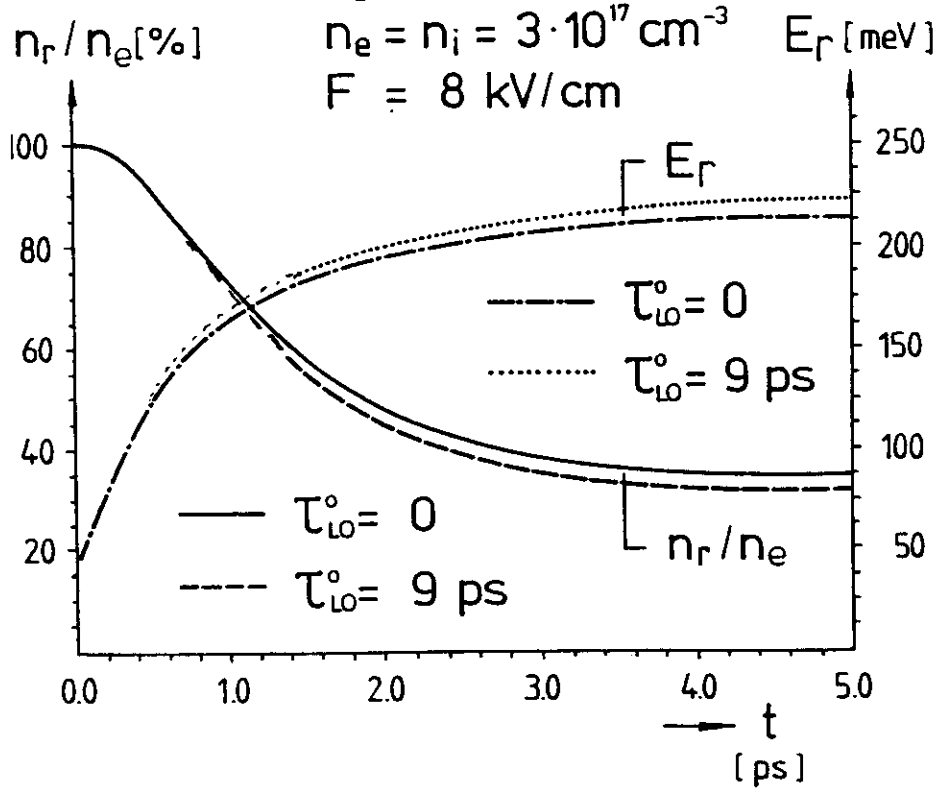
n - GaAs
T_L = 300 K
$n_e = n_i = 3 \cdot 10^{17}\,cm^{-3}$
F = 8 kV/cm
n_Γ / n_e [%]
E_Γ [meV]
E_Γ
τ^o_{LO} = 0
τ^o_{LO} = 9 ps
τ^o_{LO} = 0
τ^o_{LO} = 9 ps
n_Γ / n_e
t
[ps]
20
40
60
80
100
50
100
150
200
250
0.0
1.0
2.0
3.0
4.0
5.0

Fig 36

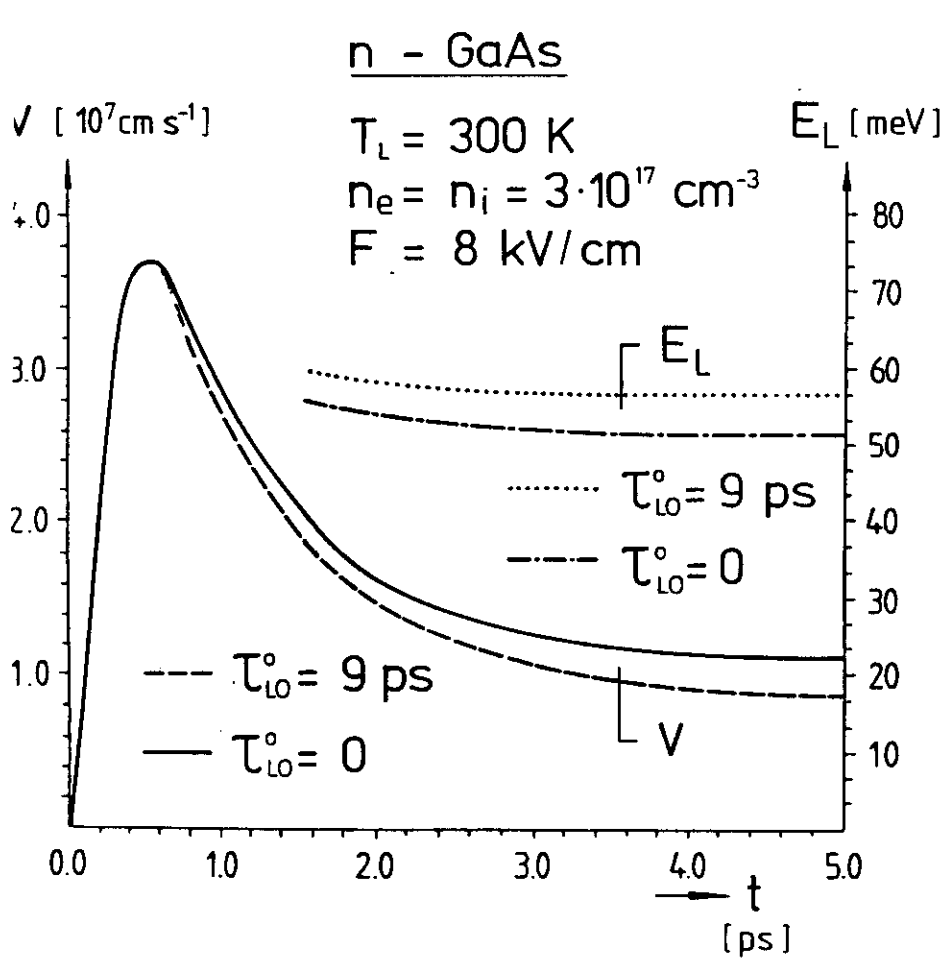
n - GaAs
T_L = 300 K
$n_e = n_i = 3 \cdot 10^{17}$ cm^{-3}
F = 8 kV/cm
v [10^7cm s^{-1}]
E_L [meV]
E_L
τ^o_{LO}= 9 ps
τ^o_{LO}= 0
τ^o_{LO}= 9 ps
τ^o_{LO}= 0
v
t
[ps]

Fig 37

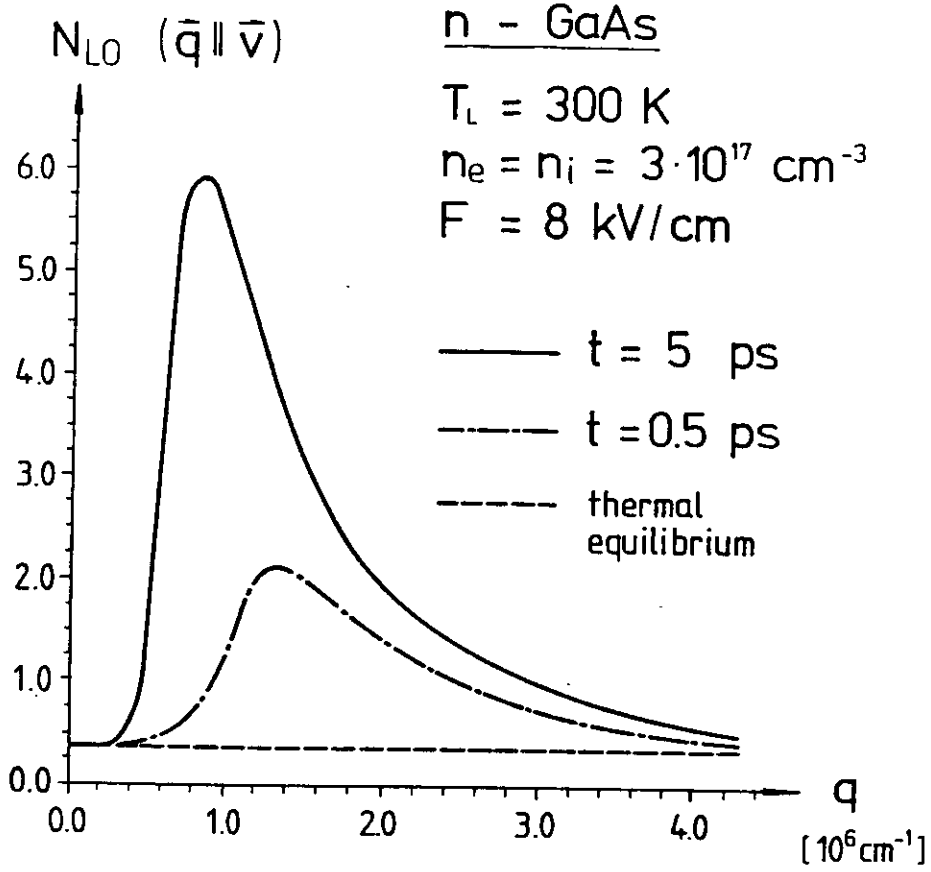
N_{LO} ($\vec{q} \parallel \vec{v}$)
n - GaAs
T_L = 300 K
$n_e = n_i = 3 \cdot 10^{17}$ cm^{-3}
F = 8 kV/cm
t = 5 ps
t = 0.5 ps
thermal equilibrium
q
[10^6cm^{-1}]

Fig 38

a)

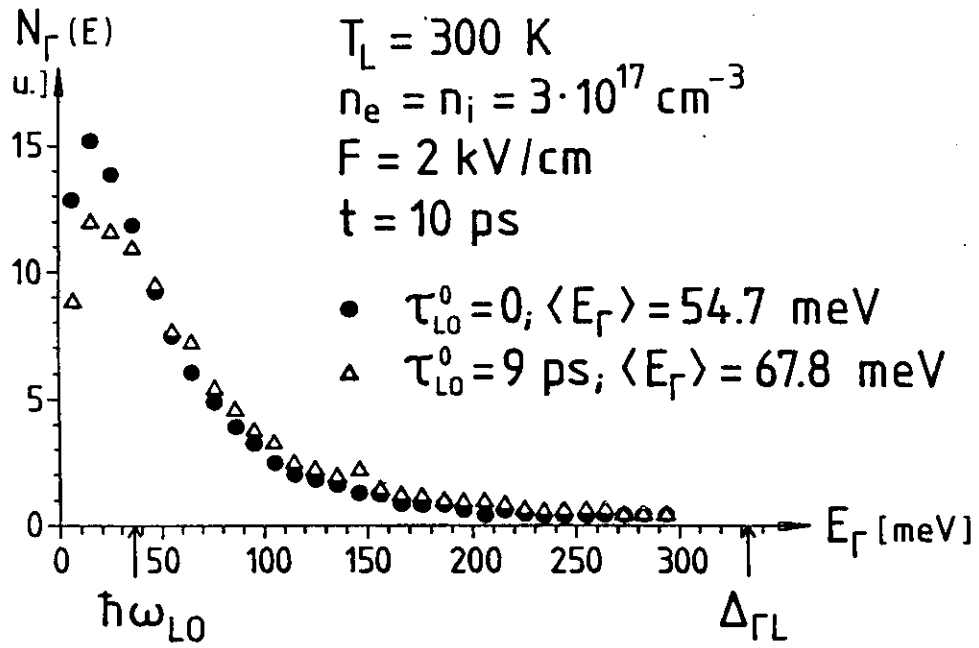

b)

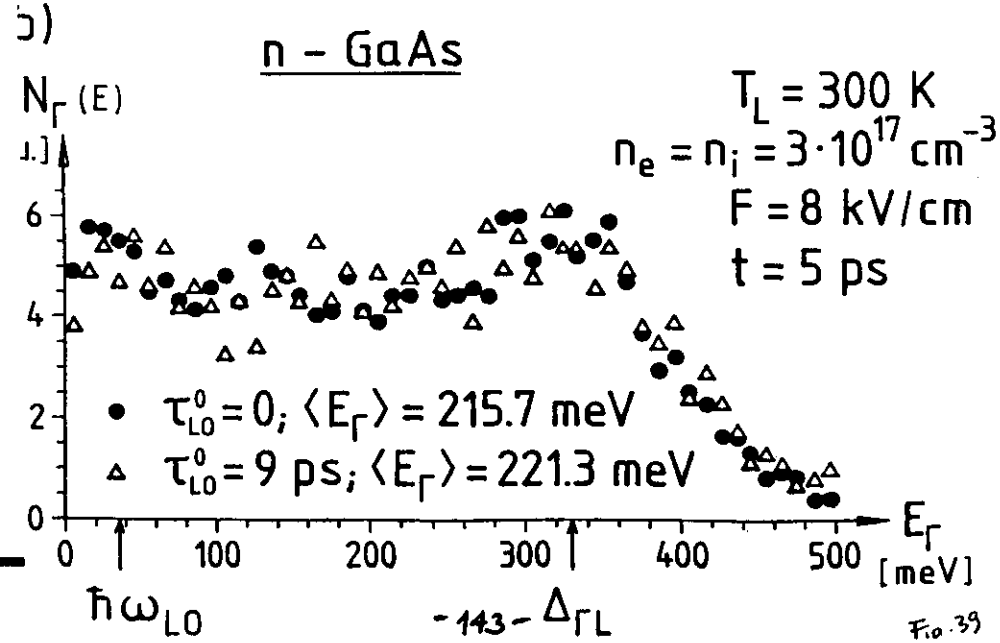

Fig. 39

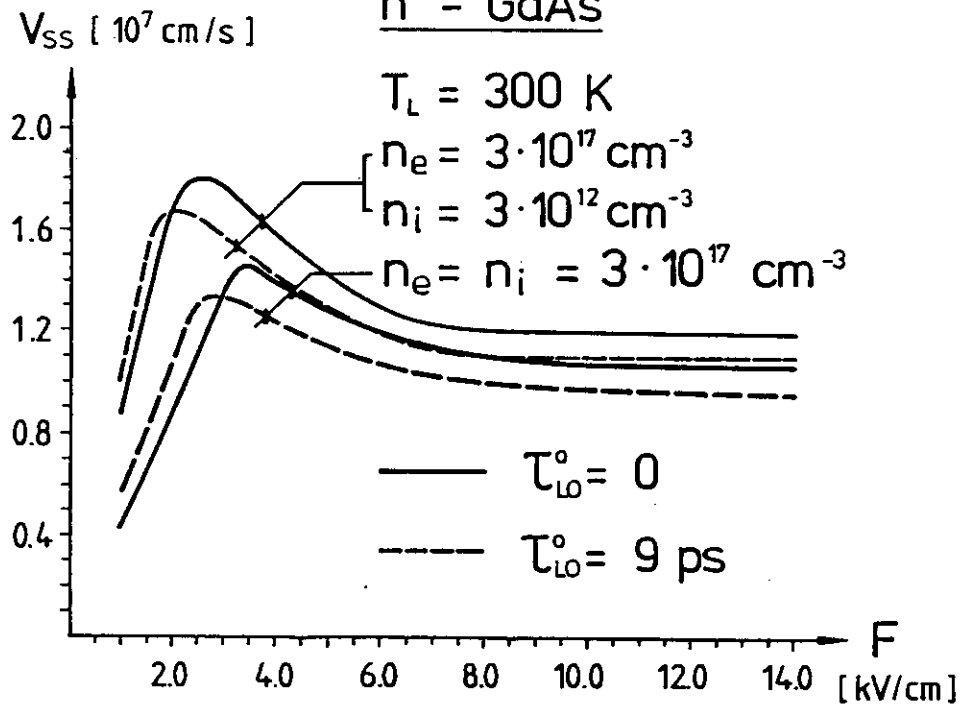

Fig 40

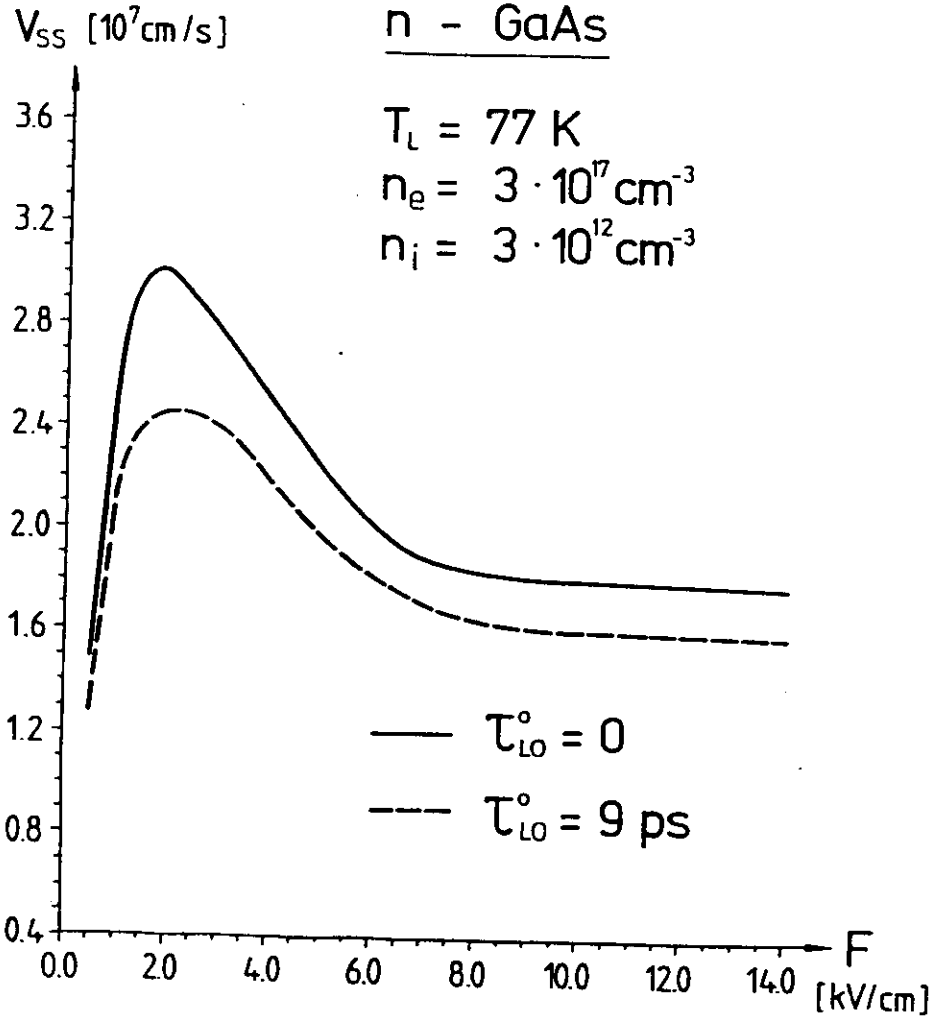
V_{SS} [10^7cm/s]
n - GaAs
T_L = 77 K
n_e = $3 \cdot 10^{17}$cm^{-3}
n_i = $3 \cdot 10^{12}$cm^{-3}
τ°_{LO} = 0
τ°_{LO} = 9 ps
3.6
3.2
2.8
2.4
2.0
1.6
1.2
0.8
0.4
0.0
2.0
4.0
6.0
8.0
10.0
12.0
14.0
F
[kV/cm]

Fig. 61